Università degli studi di Milano-Bicocca

Dipartimento di Scienza dei Materiali

Ph. D. School in Nanostructures & Nanotechnologies

XXIV cycle 2009-2011

Fabrication of nanostructured materials using block copolymer based lithography

Andrea Andreozzi
(Matr. 056401)

Tutor: Prof. Marco Fanciulli

Co-tutor: Dr. Michele Perego

Coordinator: Prof. Gianfranco Pacchioni

Contents

Chapter 1

Introduction

1.1 The NANOBLOCK project

The research activity was carried out in the framework of the European project NANOBLOCK "NANOdevice fabrication using BLOCK-copolymer based technology" [1]. The objective of the project is the growth and manipulation of semiconducting nano-objects in an oxide matrix in order to fabricate a new generation of nano-transistors, nano-memories and nano-emitters.

These nano-objects should be controlled by the combination of conventional lithography and self assembled block copolymers (BC), process known as templated-self-assembly (TSA). In fact the combination of "bottom up" self assembled BC thin films with "top-down" patterned templates allows precisely controlling of the positioning of nanodot and nanowire arrays.

Once the nano-devices, in which the nano-objects are used as elemental fabric elements and are interfaced, will be fabricated the investigation of the functionalities and electro/optical properties will be performed.

The NANOBLOCK project involves two partners in addition to MDM Laboratory, which is the coordinator partner: CEMES "Centre d'Elaboration de matèriaux et d'Etudes structurales", an autonomous laboratory of the "National Center for Scientific Research (CNRS) set in Toulouse and the Department of Electronics at the University of Barcelona. More information about the project are available on the NANOBLOCK web page (http://nanoblock-project.mdm.imm.cnr.it).

The activity described in this thesis concerns the part of the project related to the fabrication and in plane positioning of nanostructures by means of TSA. Most of the activity was focused on the development of block copolymer self assembling processes with the use of poly(styrene-block-methyl methacrylate) copolymer (PS-b-PMMA) to form PMMA cylinders or lamellae embedded in a PS matrix and perpendicularly oriented with respect to the substrate. The selective removal of the

PMMA results in a nano-structured PS polymeric template which can be used as a soft mask for advanced lithographic processes.

The main objective of the present work was the development of suitable strategies to fabricate and manipulate nanostructured materials using this block copolymer structures.

1.2 Overview about semiconductor devices

In the past the gain in productivity and performance was achieved by semiconductor industry through the scaling of MOSFET devices. The challenges facing the industries concerns the scaling of devices, such as logic and memories that together represent the major production in semiconductor devices, combined with electrical and physical requirements: electrical performance, leakage and reliability criteria should be the key guide to obtain these objectives. The development of new lithographic tools, materials and etching processes played the dominant role in achieving these gains.

Nevertheless the previsions of Moore's Law, which states the manufactures would continue to double the density of components per integrated circuit (IC) at regular intervals [2], met a critical point and to stay on the performance curve new materials were put in production in order to increase channel mobility and new approaches to device structure, such as fully-depleted silicon-on-insulator (FDSOI) and non-planar multi-gate (MG) devices, were introduced.

The continued scaling of equivalent oxide thickness (EOT) below 0.8 nm while preserving electrical performance and reliability will be a challenge [3, 4]. The EOT can be defined as the theoretical thickness of SiO_2 if its capacitance density would be as greater as the capacitance density of the high-k oxide [5]. The EOT can be expressed by the formula:

$$EOT = \frac{k_{SiO_2}}{k_{high\text{-}k}} \cdot t_{high\text{-}k} \qquad (1.1)$$

The use of high-k dielectric would allow reducing the current leakage due to the thickness of SiO_2 thanks to the increase of physical thickness of the high-k material. Moreover in order to increase mobility channel, strain engineering was introduced several years ago and now it is considered an integral part of metal-oxide-

semiconductor field-effect-transistor (MOSFET) scaling. High-k materials are now in production for dynamic random access memory (DRAM) capacitors using metal-insulator-metal (MIM) structures [6]. The main limitation due to the high dielectric constant is represented by the high physical thickness required to reduce the leakage current when the high-k materials is used. The dielectric constant must be maintained even at an ultimate film thickness of about 5 nm-7 nm.

New types of memories are also emerging as for example ferroelectric RAM (FeRAM) or magnetoresistive RAM (MRAM). As next-generation memories phase-change RAM (PRAM), resistive-change RAM (ReRAM), spin-tranfer torque MRAM and organic memories are being investigated.

The non-volatile memories (NVM) represent the best example of floating gate based process: for the scaling of both NOR and NAND devices an alternative to the traditional floating gate technology is offered by the Charge Trapping Flash Memories. The main difference between this type of memories and the NVM is represented by the silicon nitride/high-k dielectric used as charge storing instead of the silicon/oxide-nitride-oxide (ONO) stack. The major advantages in charge trapping memories are high scalability and simple integration for embedded memory application. Moreover the stress induced leakage current (SILC) is drastically reduced. Nevertheless there are also several challenges as for example the need of a high-k blocking layer between the trapping material and the gate; the gate should have a high work function thus a metal gate is mandatory to erase the memory cell with reasonable bias.

The phase change memory (PCM) is based on the properties of chalcogenide alloy, the most promising are the so-called GST (GeSbTe), and the change from crystalline or amorphous phase of the material and viceversa is used for data storage.

The main issues in the scaling technology for the logic MOSFETs are represented by the control of the short-channel effects and thus by the high channel doping required to control these effects. For DRAM the main issue concerning the shrinking is represented by the implementation of high-k material for data storage and by the leakage of current, dielectric, storage junction and access transistor source/drain subthreshold. For static random access memory (SRAM) the main issues concern the instability of hot-electron and of negative bias temperature.

Concerning the high-performance logic such as microprocessor unit, chips for PC's and servers, high complexity, high performance and high power dissipation should be considered as main characteristic of the chips. The table 1.1 shows the main requirements, updated by the International Technology Roadmap for Semiconductors, for the high-performance logic technologies from 2010 to 2015: the white cells indicate the manufacturable solutions exist and are being optimized, the yellow cells indicate manufacturable solutions are known and red cells indicate manufacturable solutions are not known. The main characteristics are reported for the extended planar bulk CMOS, for the ultra-thin body fully depleted (UTB FD) SOI MOSFET and for the multi-gate (MG) MOSFET. The grey cells indicate the periods before the production of advanced CMOS technologies, such as UTB FD and MG, has started. Physical L_g refers to the physical gate length of the devices, EOT, usually achieved by capacitance-voltage (C-V) or optical measurements, is the equivalent oxide thickness as discussed above. From 2009 high-k gate dielectric has been fabricated to control the gate leakage. The yellow cells in the extended planar bulk indicate a sort of uncertainty for the scaling of EOT below 0.9 nm while for scaling below 0.7 nm the uncertainty is marked. The channel doping in the case of planar bulk MOSFET is required to control the short-channel effect and the uncertainty becomes to be marked above 5×10^{18} cm^{-3}. The manufacturable solutions concerning the junction depth of the planar bulk MOSFET are well known and exist above 9 nm, above 8 nm the solutions are known and below 8 nm the solutions are not known. In the case of UTB FB and MG the parameters refer to the body thickness and the requirements are not well known yet. The $J_{g\ limit}$ is the maximum allowed gate leakage current density at 25° C: the introduction of high-k materials allows reducing the gate leakage current density for the same EOT [7, 8, 9, 10].

The memory technology requirements should be divided between DRAM and NVM. DRAM capacity technology is now seriously challenged because of the accelerated scaling of cell size: since the DRAM storage capacitor gets physically smaller with scaling, the EOT must scale down sharply to maintain adequate storage capacitance thus dielectric materials having high relative dielectric constant (κ) will be needed. The technology requirements of DRAM are reported in table 1.2: the white cells indicate the manufacturable solutions exist and are being optimized, the yellow cells indicate manufacturable solutions are known and red cells indicate manufacturable solutions are not known.

Year of production	2010	2011	2012	2013	2014	2015
MPU 1/2 pitch (nm)	45	38	32	27	24	21
Physical L_g (nm)	27	24	22	20	18	17
EOT (nm)						
Extended planar bulk	0.95	0.88	0.75	0.65	0.55	0.53
UTB FD				0.7	0.68	0.6
MG						0.77
Channel doping (E18/cm^3)						
Extended planar bulk	4	4.5	5	5.7	6.6	7.5
Junction depth/Body thickness (nm)						
Extended planar bulk (junction)	12	10.5	9.5	8.7	8	7.3
UTB FD (body)				7	6	5.5
MG (body)						8
$J_{g\,limit}$ (kA/cm^2)						
Extended planar bulk	0.83	0.9	1	1.1	1.2	1.3
UTB FD				1.1	1.2	1.3
MG						1.3

Table 1.1 High-performance Logic Technology Requirements [6].

Year of production	2010	2011	2012	2013	2014	2015
DRAM 1/2 pitch (nm)	42	36	31	28	25	24
DRAM cell size (μ^2)	0.01058	0.00778	0.00577	0.00314	0.00250	0.00230
DRAM storage node cell capacitor dielectric: EOT (nm)	0.6	0.5	0.4	0.3	0.3	0.3

Table 1.2 DRAM Technology Requirements [6].

1.3 Si nanocrystals based devices

A great improvement in semiconductor technology can be offered by nanocrystals based devices. They could find application in flash memories devices, as well as in optoelectronic and photovoltaic based devices.

1.3.1 Flash memories

Non-volatile memories consist of several intersecting technologies that share one common trait-non-volatility thus the requirements differ depending on their applications. Non-volatile memories have several applications in our daily lives: for example electrically erasable and programmable read-only memories (EEPROMs) and FeRAMs are used in wireless railway passes and IC cards; large-capacity flash memories are used in cellular phones, digital cameras, audio players, USB flash drives and solid-state drives for general storage and transfer of data [11]. Recent results propose graphene oxide based memory as flexible non volatile memory which have the advantage, respect to the other type of memory, to be fabricated at room temperature [12].

The stacked-gate floating-gate (FG) device structure is the most prevailing NVM implementation. The most widespread memory array organization is the so-called Flash memory. In this type of device the information is stored in the form of charge contained in the floating gate, which is a poly-silicon layer completely surrounded by dielectrics and located between the channel region and the conventional gate of a field effect transistor. The amount of charge stored on the FG layer is directly proportional to the threshold voltage of the FET and the operations of "writing" and "erasing" the memory cells implicate an increase or a reduction respectively of the amount of charge stored on the FG. The charge transfer is obtained by channel hot electron injection (CHEI) and by Fowler-Nordheim (FN) tunneling in the case of write operation and mainly by FN tunneling in the case of erase operation.

The figure 1.1 shows a schematic representation of a non-volatile memory: the bitcell is composed of a MOSFET containing a source of carriers, a drain to remove carriers from the device, a gate used to modulate the injection of carriers from the source of the device, and a substrate used to form the barrier between carriers in the source and the drain. The structural difference between a MOSFET and a non-volatile memory consists in the floating gate, i.e. an electrically isolated gate in which the charge is stored even when the system is turned off. The presence of charge shifts the threshold voltage (V_T) of the memory bit. The floating gate, composed of poly-silicon, is located between the tunnel oxide and the control gate oxide. The control gate oxide, or interpoly dielectric (IPD), can be either oxide or

oxide-nitride-oxide (ONO) and it isolates the floating gate. The charging/discharging of the floating gate is achieved through the tunnel oxide using two mechanisms: Fowler-Nordheim (FN) tunneling and channel hot-electron injection (CHEI). Concerning the programming mechanism, in FN tunneling the electrons tunnel from substrate through the thin gate oxide and eventually are collected in the floating gate. The figure 1.2 shows the band structure of the MOSFET during the FN tunneling: when a large voltage V_{cg} is applied to the control gate during programming, an electric field is created which results in a potential barrier. This barrier provides the path for the electrons to tunnel and be collected in the floating gate. The different bending of the energy bands of the control gate oxide and of the tunnel oxide is due to the different thickness of two dielectrics [13]. The tunneling current density originated from the collected electrons at the floating gate is given by:

$$J = (q^3E^2/8\pi h\Phi)\, exp\left[-4(2m)^{1/2}\Phi^{3/2}/3\hbar qE\right], \qquad (1.2)$$

where h is the Planck's constant, q is the electronic charge, E is the electric field, Φ is the barrier height and m is the free electron mass [14]. The other mechanism for programming the non-volatile memories is the hot-carrier injection (HCI): for n-type NVMs built on p-substrates the method of programming is by hot-electron injection while for p-type NVMs built on n-substrates the method of programming is by hot hole injection. The most manufactured NVMs today are n-type on p-substrates because the hot-hole injection is a very slow method since the hole mass is higher than electron mass and the Si-SiO_2 energy barrier is of 4.7 eV for holes while for electrons it is 3.2 eV. In order to program the memory cell, the hot-electrons are injected in the floating gate from the drain pinch-off region. The voltage applied to the drain (V_d) provides energy for the hot-electrons, which are accelerated by the lateral electric field (E_{lat}) along the channel into ever higher fields surrounding the drain depletion region. Once they get sufficient energy they overcome the energy barrier of 3.2 eV. A high positive V_{cg} is necessary to pull the electrons toward the floating gate otherwise they would return to the substrate. The figure 1.3 shows the energy band structure for NVM during hot-electron injection. Concerning the erasing mechanism, the main method is the FN tunneling: applying a large negative voltage at the control gate, a potential barrier is created by the

resulting electric field and this barrier provides a path for the electron to tunnel from the floating gate to the substrate through the thin gate oxide. The energy band structure during the erasing is shown in figure 1.4. The other mechanism for erasing NMV is the UV Emission in which the electrons acquire energy from UV radiation and this energy allows overcoming the energy barrier from the floating gate to either the control gate or the substrate. The figure 1.5 shows the band diagram during the erasing mechanism.

The main functional characteristics of a NVM, in order to evaluate the performance of the cell, are the endurance and the retention. These characteristics can be affected by the quality of the tunnel oxide and by the quality of the control gate oxide: for example during the charging process, by FN tunneling or HCI, oxide breakdown can occur. Oxide defects serve as trapping centers; oxide breakdown occurs after a fixed amount of charge per unit area has been injected and it is a function of applied electric field [15, 16]. Another important issue related to the quality of the oxide is the trap-up: it is defined as the trapping of electrons in the oxide during writing operations. Since the trapped charges influence the injection field, the amount of charge transferred to or from the floating gate during programming operations can be affected. Moreover the presence of defects in the control gate oxide can induce current leakage from the floating gate because of bad isolation from other electrodes if the oxide is not defect-free. Great attention should be paid during the doping of the floating gate and during the deposition and oxidation of the poly-Si [17].

As introduced before, new type of stacks have been proposed which induce lower current leakage because of lower defect densities and higher electric field properties, such as the ONO which allow reducing leakage due to the fact that the electrons get trapped in the oxide-nitride interface with a generation of electric field that opposes further charge losses [18, 19]. Typical thicknesses of the stack are around 30 nm.

The quality of the oxides should also guarantee endurance of the memory, i.e. the number of cycles the memory can withstand. When the threshold voltage difference between the programmed state and the erased state cannot be distinguished, the threshold voltage window closure, and thus the degradation of the memory, has occurred.

Retention is a measure of the time that a nonvolatile memory cell can retain the charge whether it is powered or unpowered. It takes 10 years for a NVM to have affected its retention capability. The stored charge can leak away through the control gate oxide or through the tunnel oxide and the leakage is due to mobile ions and to oxide defects. The charge loss mechanisms can be due to thermionic emission, to electron detrapping and to contamination [20, 21].

For floating gate devices the scaling of tunnel oxide and of control gate oxide presents geometric limitations and the shrinking of the dimension will be a serious challenge. The technology requirements of the NVM are divided in three categories, depending on the applications of the NVM: NAND Flash, NOR Flash and non-charge-storage memories.

All NAND Flash products are fabricated with floating-gate devices. The memory stack consists of a refractory polycide control gate, an interpoly dielectric, usually ONO layers, a polysilicon floating gate, a tunnel dielectric and a silicon substrate. However Charge Trapping NAND Flash memories, such as MANOS (metal-Al_2O_3-nitride-oxide-Si), may be used in the future because of the difficult challenges of maintaining the gate coupling ratio (GCR), defined as the capacitance ratio of the control gate to floating gate capacitor to the total floating gate capacitance, and reducing the neighboring cell cross talk in Floating Gate NAND Flash memories [22]. The table 1.3 shows the technology requirements for the Floating Gate NAND Flash: the white cells indicate the manufacturable solutions exist and are being optimized while red cells indicate manufacturable solutions are not known. As indicated in the table, from the 25 nm technology node (2012) a high-k material will be used as IPD since the space between floating gates will be too narrow to fill it with the ONO and word line polysilicon. The use of high-k materials could induce lower performance in endurance due to charge trapping and thus oxide degradation. The reduction of performance in data retention will be caused by the use of thinner tunnel oxides and by a fewer number of stored electrons. Moreover the use of high-k material will influence the choice of control gate material since a lower barrier height to silicon will cause severe gate injection during erase operation and thus materials with high work function such as p-type poly-silicon or metal should be adopted as control gate.

Year of production	2010	2011	2012	2013	2014	2015
Technology node (nm)	32	28	25	22	20	19
Tunnel oxide thickness (nm)	6-7	6-7	6-7	6-7	6-7	6-7
Interpoly dielectric material	ONO	ONO	High-k	High-k	High-k	High-k
Interpoly dielectric thickness (nm)	10-13	10-13	9-10	9-10	9-10	9-10
Control gate material	n-Poly	n-Poly	Poly/Metal	Poly/Metal	Poly/Metal	Metal
Endurance (erase/write cycles)	1.00E5	1.00E05	1.00E04	1.00E04	1.00E04	1.00E04
Data retention (years)	10-20	10-20	10-20	10-20	10	5-10

Table 1.3 Floating Gate NAND Flash Technology Requirements [6].

The table 1.4 shows the technology requirements for the Charge Trapping NAND Flash: the white cells indicate the manufacturable solutions exist and are being optimized while the yellow cells indicate manufacturable solutions are known. Al_2O_3 is the blocking oxide with the higher barrier height, but also AN, ANO or AHO are potential candidates. SiN is actually the best candidate as charge trapping layer because of relatively deep electron traps which provide good data retention even if higk-k materials with deeper traps may be used in the future [23]. The metal gate could be temporarily substituted by a p-type poly-silicon as in the case of Floating Gate NAND Flash because of its easy processing and low cost.

Year of production	2010	2011	2012	2013	2014	2015
Technology node (nm)	32	28	25	22	20	19
Tunnel dielectric material			SiO_2 or ONO	SiO_2 or ONO	SiO_2 or ONO	SiO_2 or ONO
Tunnel dielectric thickness EOT(nm)			3-4	3-4	3-4	3-4
Blocking dielectric material			Al_2O_3	Al_2O_3	Al_2O_3	Al_2O_3
Blocking dielectric thickness EOT (nm)			6-8	6-8	6	6
Charge trapping layer material			SiN	SiN	SiN	SiN
Charge trapping layer thickness (nm)			5-7	5	4-6	4-6
Gate material			Metal	Metal	Metal	Metal
Endurance (erase/write cycles)			1.00E05	1.00E04	1.00E04	1.00E04
Data retention (years)			10-20	10-20	10-20	10-20

Table 1.4 Charge Trapping NAND Flash Technology Requirements [6].

A NOR Flash consists of a single MOS transistor serving both as the cell isolation device and the storage node. The threshold voltage of the transistor is modulated by charge stored in the floating gate. The memory array allows random access of data. The cell can be programmed by CHEI and erased by FN tunneling. The Floating Gate NOR Flash technology requirements are shown in table 1.5: the white cells indicate the manufacturable solutions exist and are being optimized while red cells indicate manufacturable solutions are not known. Tunnel oxide thicknesses below 7 nm pose fundamental problems for retention reliability because of short channel effects. From the 32 nm technology node a high-k material would be necessary as interpoly dielectric in order to maintain a GCR above 0.6.

Year of production	2010	2011	2012	2013	2014	2015
Technology node (nm)	45	40	35	32	28	25
Tunnel oxide thickness (nm)	8-9	8-9	8-9	8	8	8
Interpoly dielectric material	ONO	ONO	ONO	High-k	High-k	High-k
Interpoly dielectric thickness EOT (nm)	13-15	13-15	13-15	8-10	8-10	8-10
Endurance (erase/write cycles)	1.00E5	1.00E05	1.00E05	1.00E06	1.00E06	1.00E06
Data retention (years)	10-20	10-20	10-20	20	20	20

Table 1.5 NOR Flash Technology Requirements [6].

The technology requirements for the Charge Trapping NOR Flash are shown in table 1.6: the white cells indicate the manufacturable solutions exist and are being optimized while the yellow cells indicate manufacturable solutions are known.

Year of production	2010	2011	2012	2013	2014	2015
Technology node (nm)	45	40	35	32	28	25
Tunnel oxide thickness (nm)	4.5	4.5	4.5	4	4	4
Blocking dielectric thickness EOT (nm)	6-8	6-8	6-8	6-8	6-8	5-7
Charge trapping layer thickness (nm)	4-6	4-6	4-6	4-6	4-6	4-5
Endurance (erase/write cycles)	1.00E05	1.00E05	1.00E05	1.00E05	1.00E05	1.00E06
Data retention (years)	10-20	10-20	10-20	10-20	10-20	10-20

Table 1.6 Charge Trapping NOR Flash Technology Requirements [6].

Finally the Non-Charge-Based NVM are promising to scale further since they provide memory states without electric charges. For example FeRAM devices achieve non volatility by switching and sensing the polarization state of a ferroelectric capacitor: the challenge is to find ferroelectric and electrode materials that provide adequate change in polarization. These devices are less dense than NOR or NAND Flash and are not capable of multiple logic levels (MLC) so at the moment they are not the best candidate to replace the NAND or NOR techonology. MRAM devices use a magnetic tunnel junction (MTJ) as the memory element. It consists of two ferromagnetic materials separated by a thin insulating layer which

acts as a tunnel barrier. MRAM can be used as NVM as well as SRAM and DRAM and thus it is the closest to an ideal "universal memory". However it is very difficult, as well as inefficient, to produce a magnetic field in an IC. The main challenge for this type of memories is to achieve adequate magnetic intensity fields to accomplish switching in scaled cells [6].

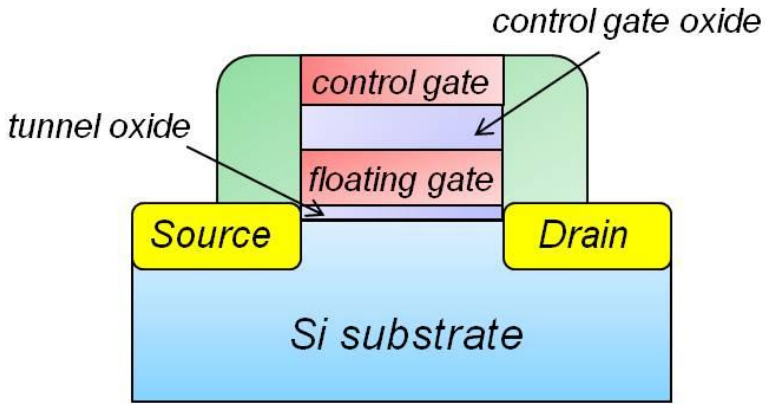

Figure 1.1 Conventional floating gate non volatile memory bit.

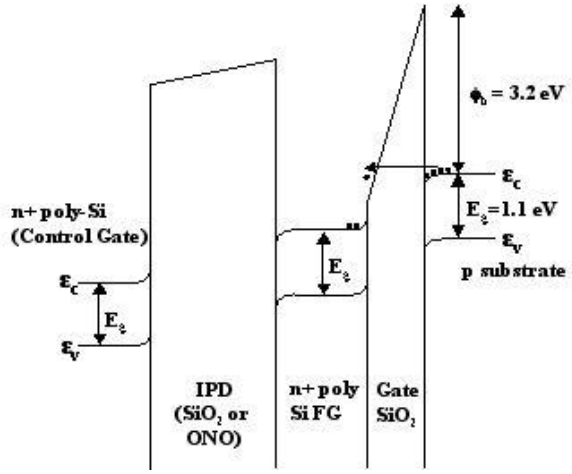

Figure 1.2 Energy band diagram of a floating gate memory during programming by FN tunneling.

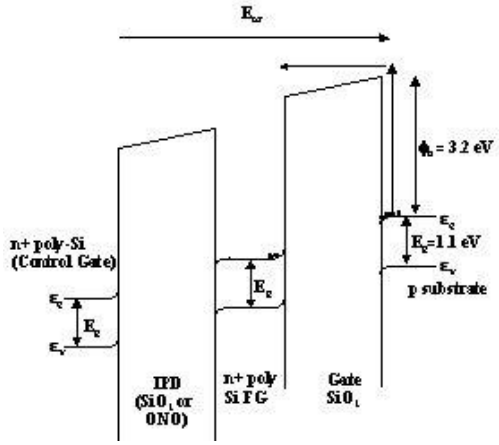

Figure 1.3 Energy band diagram of a floating gate memory during programming by hot-electron injection.

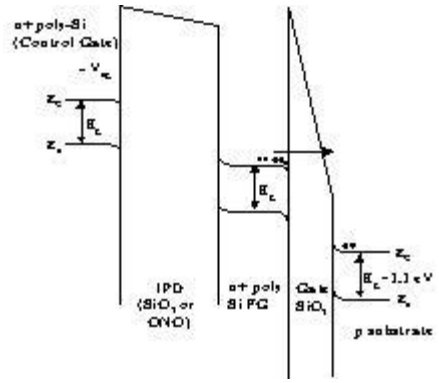

Figure 1.4 Energy band diagram of a floating gate memory during erasing by FN tunneling.

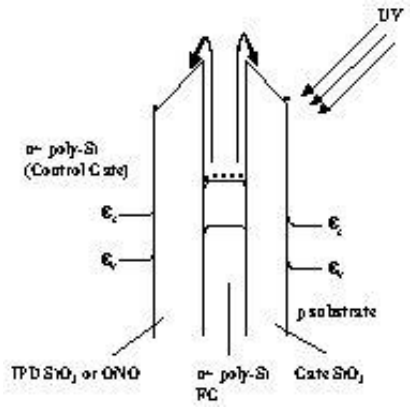

Figure 1.5 Energy band diagram of a floating gate memory during erasing by UV emission.

As mentioned before, the non volatile memories presents challenges in years to come and there are several limitation related to them although their huge commercial success. The main issue is represented by the limited potential for continued scaling of the structure. In fact the tunnel oxide has to allow quick charge transfer to and from the floating gate under low electrical operation voltage. It should allow fast and low power write and erase operations. At the same time the tunnel oxide must provide sufficient isolation under retention up to ten years as indicate by the technological requirements. The figure 1.6 shows the scaling of NOR bit cell size compared to the scaling of tunnel dielectric over several technology node: the bit cell has been reduced by over an order of magnitude during the time proposed while the thickness of tunnel oxide has remained quite constant [24]. The ability to reduce tunnel oxide thickness is limited by defects in the dielectric: the repeated cycles during programming/erasing operations could lead to bulk and interface oxide defects, which behave like traps, as well as to stress-induced leakage current. Developing a technology immune to defects in the dielectric will allow reducing operating voltage and thus enabling continued scaling technology. If one weak spot would be present in the tunnel oxide, a discharge path could be created compromising long-term non-volatility; using a distributed charge storage instead of a continuous floating gate would preserve the fundamental operating principle of the memory, enabling at the same time the scaling technology [25].

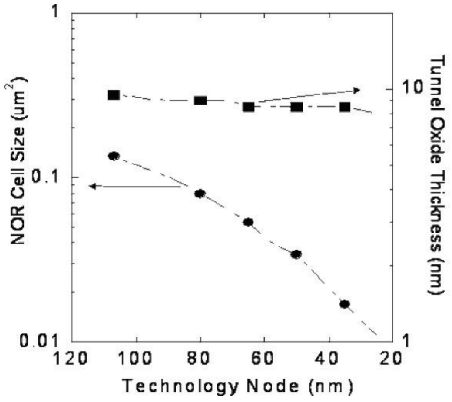

Figure 1.6 Scaling of NOR bit cell size and tunnel oxide thickness as a function of the technology node.

The idea of nanocrystals NVM device is to store the charge on a layer of discrete and mutually isolated nanocrystals instead on a continuous layer as the poly-Si FG

[26]. The presence or lack of charge in the nanocrystals would generate a change in the threshold voltage of a MOSFET. Due to the isolated nature of the nanocrystals, reduction of the tunnel oxide thickness would be possible: if a nanocrystal is near a tunnel oxide defect only local charge loss will result, with the majority of nanocrystals retaining their stored charge. This is one of the main advantages of a nanocrystals-based NVM. Differently, a defect in the tunnel oxide of a continuous floating gate would result in complete charge loss. In this way nanocrystals-based NVMs seem to offer the possibility to reduce the tunnel oxide of the device and thus to reduce the operating voltage. The figure 1.7 shows a schematic representation of a Nanocrystals NVM. The possibility to reduce the thickness of the tunnel oxide is also due to the effects of Coulomb Blockade [27].

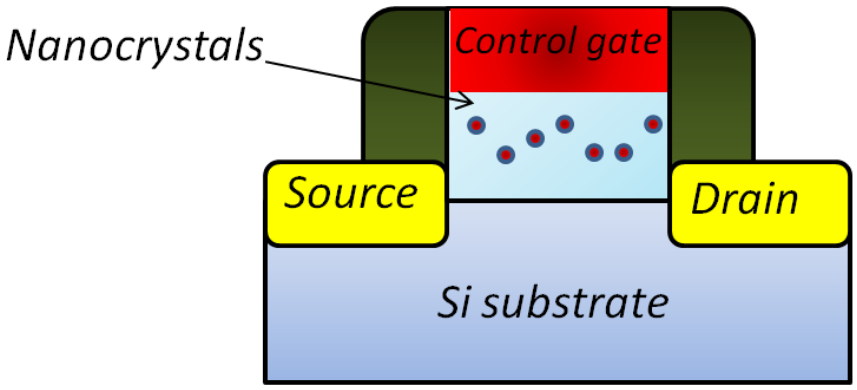

Figure 1.7 Nanocrystals non volatile memory.

Other important advantage is the possibility to use a simplified process of fabrication because of the absence of a dual-poly layer; moreover the absence of a conventional floating gate allows reducing the issue related to the drain-induced-barrier-lowering (DIBL). The distributed nature of the charge makes the nanocrystals NVMs immune to stress induced leakage current (SILC) and oxide defects. Nevertheless the low capacitive coupling between the external control gate and the nanocrystals charge storage layer results in higher operating voltage and removes the coupling ratio, which is used to optimize the performance/reliability trade-off. Thus several challenges have to be faced in the Nanocrystals NVM yet.

1.3.2 Optoelectronic and photovoltaic

Nanocrystals NVMs are not the only applications in the nanoelectronic field. Nanocrystals based devices could find application also in solar and emitting devices. Semiconductor nanocrystals are promising candidates for low cost next-generation photovoltaic devices. They can be dispersed in solvents, combined with polymers and deposited on various substrates to form dye-sensitized solar cells, hybrid nanocrystal–polymer composite solar cells and all-inorganic nanocrystal solar cells. Such technologies allow obtaining scaling and cost advantages when compared with conventional single crystal and thin film solar cells [28, 29, 30, 31, 32, 33, 34].

Light-emitting semiconductor nanocrystals are potentially useful for tasks such as single-molecule biological imaging and the creation of single-photon sources and low-threshold lasers because of their size-tunable optical properties [35, 36].

With the aim to fabricate a new generation of nanocrystals-based nano-devices, in which the nano-objects are ordered in 2-dimensional non-periodic arrays by means of TSA, an intense activity for developing a reliable and reproducible protocol in order to obtain block copolymers self-assembly has been performed in this thesis work.

References

1. http://nanoblock-project.mdm.imm.cnr.it/

2. R. R. Schaller, Moore's law: past, present, and future *IEEE Spectrum* (1997)

3. S. E. Thompson and S. Parthasarathy, *Materials Today* **9**, 20 (2006)

4. M. Ieong, V. Narayanan, D. Singh, A. Topol, V. Chan, and Z. Ren, *Materials Today* **9**, 26 (2006)

5. G. D. Wilk, R. M. Wallace, J. M. Anthony *J. Appl. Phys*. **89**, 5243 (2001)

6. International Technology Roadmap for Semiconductors, http://www.itrs.net/

7. B. H. Lee, J. Oh, H. H. Tseng, R. Jammy, and H. Huff, *Materials Today* **9**, 32 (2006)

8. J. P. Locquet, C. Marchiori, M. Sousa, J. Fompeyrine, J. W. Seo, *J. Appl. Phys.* **100**, 051610 (2006)

9. H. Wong, H. Iwai, *Microelectr. Eng.* ***83***, 1867 (2006)

10. J. Robertson, *J. Appl. Phys.* **104**, 124111 (2008)

11. Y. Fujisaki, *J. J. Appl. Phys.* **49**, 100001 (2010)

12. H. Y. Jeong, J. Y. Kim, J. W. Kim, J. O. Hwang, J.-E. Kim, J. Y. Lee, T. H. Yoon, B. J. Cho, S. O. Kim, R. S. Ruoff and S.-Y. Choi, *Nano Lett.* **10**, 4381 (2010)

13. http://aplawrence.com/

14. M. Lezlinger and E. H. Snow, *J. Appl. Phys.* **40**, 278 (1969)

15. E. Harari, *J. App. Phys.* **49**, 2478 (1978)

16. A. Modelli and B. Ricco, *IEEE IEDM Tech. Digest*, 148 (1984)

17. L. Faraone, *IEEE Transactions on Electron Devices*, **ED-33**, 1785 (1986)

18. S. Mori, Y. Kaneko, N. Arai, Y. Ohshima, H. Araki, K. Narita, E. Sakagami and K. Yoshikawa, *Proceedings 1985 IEEE IRPS* 132 (1990)

19. M. Aminzadeh, *IEEE Transactions on Electron Devices*, **ED-35**, 205 (1988)

20. R. E. Shiner, *Proceedings IRPS* 238 (1980)

21. N. Mielke, *Proceedings IRPS* 106 (1980)

22. Y. Shin, J. Choi, C. Kang, C. Lee, K. T. Park, J. S. Lee, J. Sel, V. Kim, B. Choi, J. Sim, D. Kim, H. J. Cho andK. Kim, *IEDM Tech. Digest*, 547 (2005)

23. A. Chin, C. C. Laio, C. Chen, C. Chiang, D. S. Yu, W. J. Yoo, G. S. Samudra, T. Wang, I. J. Hsieh, S. P. McAlister, and C. C. Chi, *IEDM Tech. Digest*,165 (2005)

24. R.Muralidhar, M. A. Sadd and B. E. White, "*Silicon Nanocrystal Nonvolatile Memories"*, pp 223-249, *Nanostructure Science and Technology, Device Application of Silicon Nanocrystals and Nanostructures* (2009)

25. J. De Blauwe, *IEEE Transactions on Nanotechnology*, **1**, 72 (2002)

26. D.-H. Chae, T.-S. Yoon, D. H. Kim, J.-Y Kwon, K.-B Kim, J. D. Lee and B.-G. Park, *57th Annu. Device Research Conf. Dig.*, 140 (1999)

27. J. J. Welser, S. Tiwari, S. Rishton, K. Y. Lee and Y. Lee, *IEEE Electron Device Lett.* **18**, 278 (1997)

28. Y. Wang, Y. Sun and K. Li, *Mater. Lett.*, **63**, 1102 (2009)

29. M. Gratzel, *J. Photochem. Photobiol., A*, **168**, 235 (2004)

30. R. Watt, D. Blake, J. H. Warner, E. A. Thomsen, E. L. Tavenner, H. Rubinsztein-Dunlop and P. Meredith, J. *Phys. D: Appl. Phys.*, **38**, 2006 (2005)

31. N. C. Greenham, X. Peng and A. P. Alivisatos, *Phys. Rev. B: Condens. Matter*, **54**, 17628 (1996)

32. I. Gur, N. A. Fromer, M. L. Geier and A. P. Alivisatos, *Science*, **310**, 462 (2005)

33. K. S. Leschkies, R. Divakar, J. Basu, E. Enache-Pommer, J. E. Boercker, C. B. Carter, U. R. Kortshagen, D. J. Norris and E. S. Aydil, *Nano Lett.*, **7**, 1793 (2007)

34. Y. Wu, C. Wadia, W. L. Ma, B. Sadtler and A. P. Alivisatos, *Nano Lett.*, **8**, 2551 (2008)

35. V. I. Klimov, A. A. Mikhailovsky, S. Xu, A. Malko, J.A. Hollingsworth, C. A. Leatherdale, H.-J. Eisler and M.G. Bawendi, Science **290**, 314 (2000)

36. V. L. Colvin,M. C. Schlamp and A. P. Alivisatos, *Nature* **370**, 354 (1994)

Chapter 2

Experimental

2.1 The Self-Assembly Technology

The self assembly technology, which is the spontaneous organization of materials into regular patterns, can be a useful tool for alternative patterning approaches [1]. Self-assembly is one of the few practical strategies for making ensembles of nanostructures. There are two main type of self-assembly: static self-assembly and dynamic self-assembly. The former involves systems at global or local equilibrium which do not dissipate energy after the formation of the ordered structure: examples can be molecular crystals, phase separated and ionic layered polymers, liquid crystals. The latter involves interactions in which the system dissipates energy: examples are patterns formed by competition between reaction and diffusion in oscillating chemical reactions, galaxies, solar systems. The components of self-assembly systems must be able to move with respect to one another. Their steady-state positions balance attractions and repulsion. Non-covalent or weak covalent interactions, such as van der Waals, electrostatic and hydrophobic interaction, hydrogen and coordination bond, are involved in molecular self-assembly. Self-assembly originated in the study of molecules, but it is a strategy that is applicable at all scales.

The possible applications using self-assembly approach involve nanotechnology, in particular nanoelectronics in which bottom-up has a fundamental role. Bottom-up approach uses chemical properties of single molecules to cause single-molecule component to self-assemble into some useful conformation.

Bottom-up approaches using self-assembling materials are emerging as a valid tool to overcome the limitations of optical diffraction and the wavelength light sources which avoid fabricating sub-30 nm features. The complexities associated with continued dimensional scaling of the photolithography process for future integrated circuit (IC) generations have created opportunities for alternative patterning

approaches, and one inviting prospect from the world of nanotechnology involves using self-assembling materials to define the features of IC elements.

Self-assembly is an attractive concept because the underlying mechanisms in principle permit scaling to atomic-scale dimensions; however, any legitimate IC patterning option necessarily involves much more than high resolution. Other important factors include extreme demands for pattern uniformity, minimal pattern roughness, and low defectiveness levels; a need for precise pattern alignment and registration; the ability to pattern a wide variety of shapes; rapid parallel processing across large wafer areas; and materials/process compatibility with the semiconductor manufacturing infrastructure. This long list of stringent requirements is well-met by photolithography and thus the semiconductor industry will likely never abandon the process as its primary patterning approach, but will rather increasingly seek symbiotic techniques for augmenting lithographic resolution capabilities.

It is in this spirit of technological compatibility that polymer self-assembly has recently emerged as an unconventional approach for extending the photolithography process to finer patterning dimensions. In particular, block copolymers (BC) have received great attention due to their processing advantages and to their compatibility with the semiconductor technology [2, 3, 4, 5, 6, 7].

2.1.1 Block Copolymers Self-Assembly

Block copolymers are a special class of polymer with two or more polymer chains chemically bound to each other [8]. They can lead to various nano-structures depending on the composition and chain architecture. They belong to a class of soft materials which are characterized by fluid-like disorder on molecular scale and high degree of order at longer length scales. There is an enormous range of molecular architectures of block copolymers, but all these architectures can be understood basing on two parameters: the number of distinct blocks composing the block copolymers and the linear versus branched sequencing of the blocks [9].

The simplest architecture, used also in the present thesis work, is the linear AB diblock. Figure 2.1 shows different configurations involving two or three monomer types. The architectures are classified also by topology, i.e. linear or branched

sequencing. The properties of block copolymers materials rely on their mesoscopic self-assembly which produces spatially periodic composition patterns, commonly referred to microphases. Since different blocks are incompatible for chemical and entropic reasons, they tend to separate and to form microphases: the entropy of mixing per unit of volume of dissimilar polymers is small and it varies inversely with the molecular weight. Thus, even minor differences between the blocks can produce excess free-energy contributions unfavourable to mixing. This phenomenon is accentuated for block copolymers with high molecular weight.

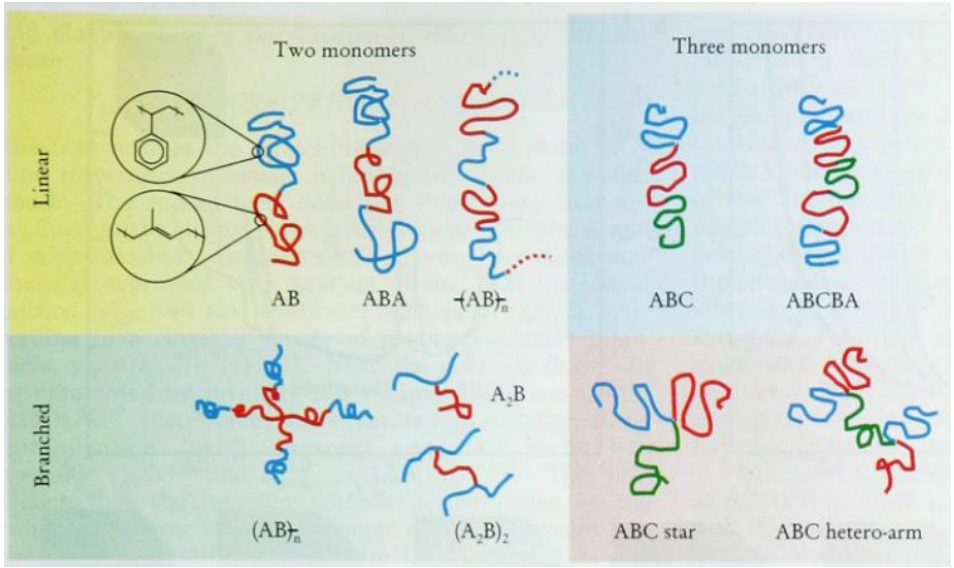

Figure 2.1 Different types of block copolymers depending on the number of monomer types and on the topology (linear versus branched sequencing) [9].

The mixing free energy is commonly described by the *Flory-Huggins interaction parameter* which describes the free-energy cost per monomer of contacts between A and B monomers. The parameter is described in the following formula:

$$\chi_{AB} = (Z/k_BT)[\varepsilon_{AB} - (1/2)(\varepsilon_{AA} + \varepsilon_{BB})] \qquad (2.1)$$

Z indicates the number of nearest neighbor monomers to a copolymer configuration cell, k_B is the Boltzmann constant, ε_{AB} indicates the interaction energy per monomer between A and B monomers while ε_{AA} and ε_{BB} indicate the interaction energies par monomer between same monomer types. A positive value of the parameter indicates net repulsion between A and B while negative χ_{AB} indicates free-energy drive towards mixing: it means that A-B contact produces lower energy than the sum of A-A and B-B contacts. As general rule, for typical dissimilar monomer pairs with no strong specific interactions, χ_{AB} is positive and small compared with unity.

However the covalent bond linking the blocks prevents a macrophase separation, as it happens for homopolymers, and it counterbalances the thermodynamic forces driving separation. In this way a nanoscale structural organization of the block copolymers occurs [10, 11]. Looking at the formula 2.1 it is clear that χ_{AB} varies inversely with the temperature. Thus an increase of temperature is necessary to promote mixing between blocks. The entropic forces from the covalent linkages, called also chain elasticity, contribute to the extended configurations of block copolymers. The entropic force can be approximated by the Hookian law. For a block with N monomers extended to a distance R, the elastic free energy can be expressed as:

$$F_e = 3k_B TR^2/(2Na^2) \qquad (2.2)$$

In the expression 2.2 a refers to a monomer scale size and depends on the local structure of the polymer chain. The block molecular structure is characterized by the overall degree of polymerization N, which is the total number of monomers per macromolecule, and by the composition $f_A = N_A/N$, where N_A is the number of A monomers per molecule.

The equilibrium polymer-polymer phase behavior is controlled by the molecular architecture, the choice of monomers, the composition and the degree of polymerization [11]. The equilibrium state of a block copolymer is represented by the ensemble of molecular configurations which minimize the free energy G. The system enthalpy H is reduced by the condition $\chi_{AB} > 0$, which means a reduction in contacts between blocks. The state of segregation is controlled by χN [12]. For $\chi N << 10$, entropic factors dominate and the block copolymers are in a spatially homogeneous state. When $\chi N \sim 10$, a delicate balance exists between entropic and energetic effects. Increasing χN and in particular when $\chi N >> 10$, a phase transition occurs. The phase is denoted as order-disorder transition (ODT). When $\chi N >> 10$, the contacts between blocks decrease at the expense of addition al chain stretching, energetic factors dominate and microstructures are characterized by narrow interfaces. Except for the case near ODT curve ($\chi N \sim 10$), where block copolymers composition f is correlated with χN, changes in f affect the shape and packing symmetry of the ordered microstructures. Above ODT curve, several ordered microphase structures have region of thermodynamic stability. For high asymmetric AB diblock copolymers (ratio above 80:20), patterns consist of close-packed zero-

dimensional spheres of B block embedded in a matrix of A block. More symmetric materials (70:30) form one-dimensional close-packed cylinder of B block embedded in a matrix of A block, and symmetric block copolymers (50:50) create alternating two-dimensional lamellae.

While the competition between the interfacial and chain-stretching energies governs the bulk equilibrium phase behaviour, the relative volume fractions of the blocks control the curvature, size and periodicity of the microdomains [1, 11, 12, 13, 14]. The energetically preferable arrangement, where the smaller B blocks pack into the interiors of A blocks, allows the longer A blocks to reside on the convex side of A-B interface, which reduces the elastic energy.

Figure 2.2 shows the phase diagram for linear AB diblock copolymers. The phases predicted by the self-consistent mean-field theory are four: spherical, cylindrical, gyroid and lamellar [15, 16, 17, 18]. The gyroid phase, whose stability regions are close to the ODT and between the lamellar and cylindrical phases, is one of the several cubic structures characterized by domain boundaries with negative Gauss curvature. The picture shows the ordered microphase region above ODT curve, depending on χN and the equilibrium morphologies as a function of composition f_A with fixed χN.

The size of microdomains scales with the block copolymer molecular weight. Often, for symmetric diblock copolymers, the size of microdomains is denoted as the natural period L_0 that corresponds to the length of two copolymer molecules in the ordered state [10]. The law which governs the correlation between microdomain size L_0 and molecular weight can be expressed as $L_0 \propto N^{\alpha}$; here N indicates the number of monomers in the diblock copolymers and α varies with the degree of phase separation.

The theories about block-copolymer phase behavior can be divided in two categories: strong segregation limit (SSL) when $\chi N >> 10$ and weak segregation limit (WSL) when $\chi N \leq 10$. In the first case the interfaces of microdomain structures are sharp while in the second case chain stretching is neglected [19, 20]. The SSL is useful to predict the symmetry, size and periodicity far away from ODT while near ODT the situation is complex and a correlation between χ, N and f can lead to curvature in the order-disorder transition lines [21]. In the SSL, the mean-field theory suggests that L_0 scales with $N^{2/3}$; in the WSL L_0 scales with $N^{1/2}$ while in the intermediate segregation region (ISR), between SSL and WSL, α varies

theoretically from 0.72 to 1.017 and experimentally from 0.8 to 0.83 [22, 23, 24]. When quenched below the ODT an undisturbed disordered melt will order without a preferred direction thus leading to short-range order but long-range isotropy. In order to recover long-rang order, the application of a large-amplitude oscillatory shear field can induce oriented microstructures, with highly anisotropic properties [25, 26].

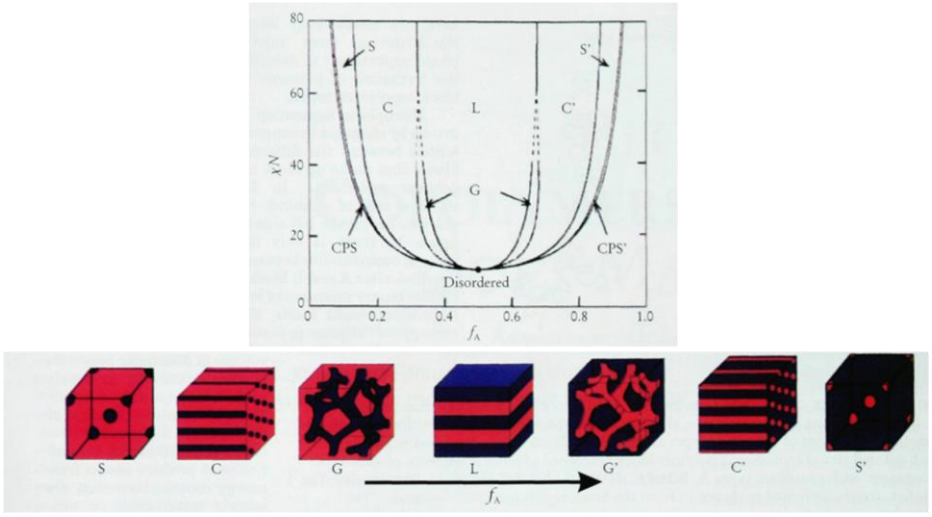

Figure 2.2 Phase diagram for linear AB diblock copolymers. In the top part of the picture the equilibrium morphologies predicted by self-consistent mean-field theory are depicted while in the bottom part of the picture a representation of the equilibrium microdomain structures as a function of f_A are reported [9].

2.1.1.1 PS-b-PMMA thin films

Block copolymers thin films differ from their bulk morphologies [1]. When a block copolymer is confined to form a thin film on a surface, its morphology is critically influenced by film thickness *t* and by the energetic interactions at the interfaces, i.e. air/polymer interface and polymer/substrate interface [27, 28, 29, 30]. A film confined between two rigid interfaces belongs to the category of "hard" confinement while "soft" confinement refers to a film where one interface is in direct contact with the atmosphere [31].

Considering the more common "soft" confinement, the polymer domain spacing L_0 has a fundamental role in the morphology. In general pattern formation is dictated by the preference of the polymeric blocks for one or both of the interfaces, as well as the total film thickness. The rule is the orientation of the microdomains parallel to the substrate: in this case one of the blocks will preferentially wet the interface. If

there is incommensurability between the film thickness t and lattice spacing L_0, the formation of islands or holes occurs. The degree of incommensurability is described by the deviation of the ratio t/L_0 from the commensurability condition [32]. If, for example, a lamellar AB diblock copolymer presents preferential surface interactions and the A block wets both substrate and free interfaces (symmetric wetting), the commensurability is achieved for an integer value of the ratio t/L_0 and no island or hole formation occurs at free surface. If block A wets the substrate and block B wets the free surface (anti-symmetric wetting) the commensurability condition is achieved for $t/L_0 = n+0.5$ (n = 1, 2, 3...) [4].

Lamellar microdomains of symmetric polystyrene-*block*-poly(methylmethacrylate) (PS-*b*-PMMA) can be treated as example. PS-*b*-PMMA is a good material because the PMMA domains can be easily removed using ultraviolet exposure and acetic acid treatment, leaving nanoporous PS film that can be used as soft mask for lithographic processes [13, 33, 34, 35, 36, 37, 38, 39, 40]. The affinity of the polar PMMA block for the hydrophilic oxide surface and the lower surface energy of the non-polar PS block lead to PMMA wetting of the substrate surface and to the PS assembling at air interface [10]. If the film thickness is commensurate with domain spacing L_0, and for this type of block copolymer an anti-symmetric wetting occurs ($t/L_0 = n+0.5$), a series of lamellae of alternating composition join the two interfaces. On the contrary, island and holes form on the surface for minimizing the total energy if the thickness is incommensurate with lattice spacing.

For microstructures with more complex symmetries, determination of the commensurability condition is more difficult than for lamellae, but the same principle of island/hole formation on preferential surfaces applies.

As introduced before, also the energetic interactions at interfaces play an important role in the morphologies of BC. The polymer/air interface for example imposes an inert gas environment for the BC self-assembling. The better, and much diffused, way to promote self-organizing of BC is to perform the process under vacuum. As mentioned before, the rule is the parallel orientation of the microdomains respect to the substrate. Nevertheless the properties of the substrate-polymer interface can be modified by tuning the surface chemistry in order to achieve perpendicular orientation of BC microdomains.

Different strategies can be used to achieve perpendicular orientation of the microdomains: surface modification, strong electric field and solvent annealing [41,

42, 43, 44]. The most common method to modify the substrate and thus to control the polymer/substrate interaction is the use of random copolymers.

Random copolymer brushes refer to an assemblage of tethered polymer chains consisting of two different repeat units which are randomly distributed along the polymer chain. In a random copolymer system with the monomer A and monomer B, the resulting polymer would be completely random with no patterned distribution along the chain.

Referring to the PS-*b*-PMMA system, which is the block copolymer used in the present thesis work, a random copolymer PS-*r*-PMMA is considered. In any case the concept can be applied generally to other systems. The possibility to create a surface which consists of the same monomers as found in a block copolymers is a great simplification and guarantees tunability over a wide range of surface affinities, including neutrality. The polymer brushes are amorphous thus allowing uniform coverage of the surface: in this way the morphology of the brush is not important allowing great simplification. Control of the interactions between surface and polymers by means of random copolymers were proposed, even if the preparation of the random copolymers, by a free-radical polymerization, caused broad molecular weight distribution [45, 46]. A great improvement was offered by the control of the interfacial energy with anchored random copolymer chains having low polydispersity, i.e. the measure of the distribution of molecular mass in a given polymer sample: the improvement consisted in the use of a unimolecular initiator based on *2,2,6,6-tetramethylpiperidinyloxy (TEMPO)*. Polymers synthesized with TEMPO initiator are terminated on one end with a moiety containing a hydroxyl (OH) group and on the other end with the TEMPO group [47, 48]. The figure 2.3 shows a schematic view of the end-functionalized random copolymer.

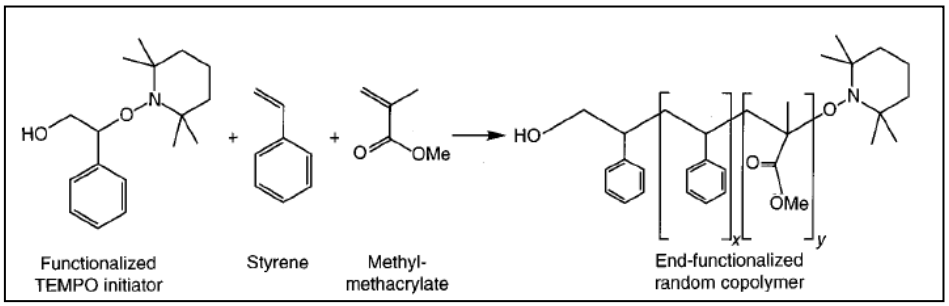

Figure 2.3 Functionalized TEMPO initiator is combined with Styrene and Methyl-methacrylate to synthesize End-functionalized random copolymer [47].

The OH group is used to end-graft the chains to the native silicon oxide layer. Once the random copolymer has been deposited on the substrate by spin-coating, an annealing well above the glass transition temperature T_g of both PS and PMMA has to be performed to allow the terminal OH groups diffusing to and reacting with the native oxide layer. Unattached polymer chains are usually removed by rinsing in toluene. The resulting thickness is approximately twice the radius of gyration of the grafted chains.

Homopolymer dewetting experiments demonstrated the possibility to neutralize the surface, with interactions between homopolymers and the brush that can be finely tuned by varying the composition of the polymers. This neutralization should allow perpendicular orientation of the microstructures respect to the surface [49, 50, 51, 52]. The composition of random copolymers influences the orientation of block copolymer: depending on the desired morphology, different windows of thickness have been found as a function of the composition of random copolymer. Grazing-incidence small-angle X-ray scattering (GISAXS) studies showed the optimum thickness condition, in which balanced interfacial interactions is achieved, to the perpendicular orientation of the domains [53, 54, 55]. The figure 2.4 shows the thickness windows for the perpendicular orientation of the domains for cylinder-forming PS-*b*-PMMA and for lamella-forming PS-*b*-PMMA.

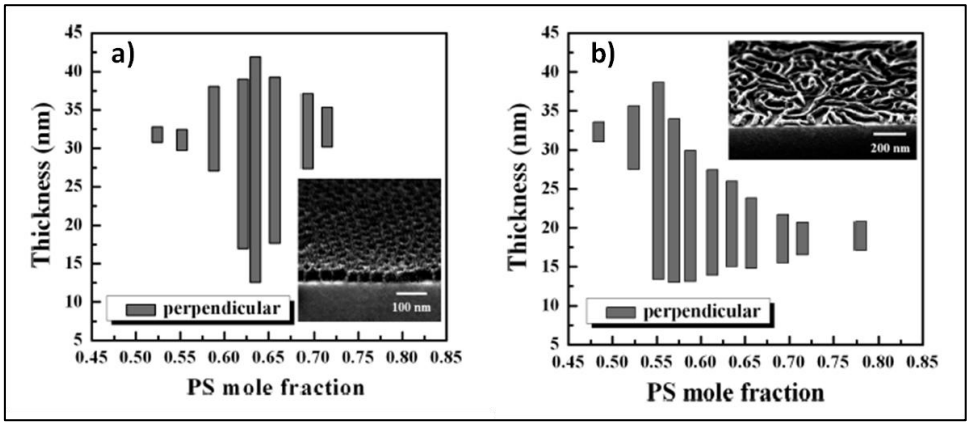

Figure 2.4 Windows of thickness as a function of PS mole fraction in PS-*r*-PMMA for cylinder-forming PS-*b*-PMMA (a) and for lamella-forming PS-*b*-PMMA. The inset in the figure (a) refers to the 42 nm thick film deposited on random copolymer with PS fraction of 0.64 while the inset in the figure (b) refers to the 39 nm thick film deposited on random copolymer with PS fraction of 0.55 [53].

Another method to control the orientation of BCs thin film is offered by solvent annealing process which exploits the increased mobility in the BC thin films. In this

approach solvent vapor is used to partially solubilize and to plasticize the thin film thus increasing the chains mobility, due to a reduction of glass transition temperature of the blocks [56, 57, 58]. The solvent must be suitable for both the blocks and in the case of PS-*b*-PMMA a solvent preference for PMMA is indicated in order to overcome the free surface preference for the lower surface tension PS blocks to produce well-ordered structures [59]. Under the saturated solvent vapor the films undergo a swelling and are driven to a disordered phase. Then the film is removed from the saturated solvent vapor and exposed to an ambient atmosphere. During solvent evaporation, i.e. during the removal of the film from the solvent vapor, the evaporation begins surface and a gradient in solvent concentration will develop normal to the surface. A further evaporation of the solvent should induce phase ordering at top surface and propagation of the ordering from the top to the bottom of the film [60, 61].

Concerning the electric field method, the driving force to align BC microstructures is the difference in the dielectric constants $\Delta\varepsilon$ between blocks. In this way anisotropic microdomains are aligned in the direction of applied electric fields [62, 63].

Also the control over lateral ordering in aligned microdomains has an important role. Among the range of strategies to achieve long-range lateral ordering, which includes chemically patterned surface, shear flow and directional solidification, graphoepitaxy offers a rich opportunity for studies of self-assembly behavior in confined environments and represents a valid source of innovation in nanofabrication methods [64, 65, 66, 67, 68, 69]. In order to achieve topographic guiding patterns, plasma etching of solid substrates using a patterned photoresist layer as an etch mask is required. In graphoepitaxy the wall spacing ranges from 2 to 3 times the lattice spacing in block copolymers to few microns. For example in the case of sphere-forming BC, perfect arrays of sphere with n rows were observed when the wall spacing W is between $(n-0.5)L_0$ and $(n+0.5)L_0$, L_0 being the lattice spacing of spheres [70, 71]. Defects such as vacancies or dislocations can be induced by defects in the wall edge. Considering other morphologies, such as cylindrical and lamellar microdomains, different cases were found. Vertically oriented cylinders were investigated within patterned substrates [40]. As in the case of flat surfaces, the major requirement to induce perpendicular orientation of cylinders respect to the substrate is the treatment of patterned substrate with random

copolymers. Considering the common PS-*b*-PMMA system, PS-*r*-PMMA random copolymers should be used.

Focusing on the lamellar morphology, it has been well established that interactions between the blocks and the walls govern the orientation of lamellar microdomains, and the commensurability between the wall separation and the copolymer period affects domain spacing. To align the perpendicular lamellar microdomains within the patterned substrates the bottom surface should have a neutral interaction with both blocks while the sidewalls can have different type of wetting. A first type of orientation can be induced by neutral wetting of the substrate by both blocks and by preferential wetting of the sidewalls by one block: for example PS-*b*-PMMA block copolymers would have neutral interactions with the substrate while gold sidewalls would induce preferential wetting of PS. In this case the lamellar microdomains would orient perpendicularly respect to the substrate and parallel to the sidewalls. Perpendicular orientation of the lamellar microdomains both respect to the substrate and to the sidewalls requires a neutral layer both on the substrate and the sidewalls [39]. Figure 2.5 shows the different cases of orientation for the lamellar PS-*b*-PMMA structures.

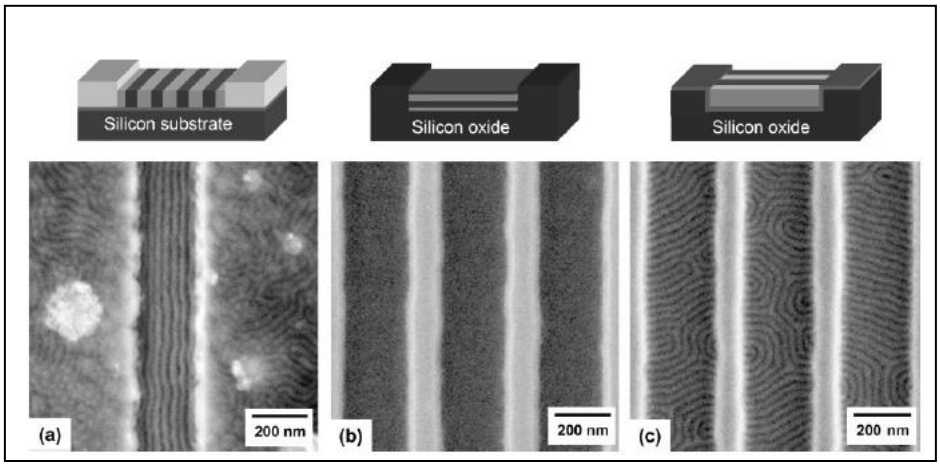

Figure 2.5 Lamellar structures of PS-b-PMMA: perpendicular orientation of domains respect to the neutralized substrate and preferential wetting of gold sidewalls by PS blocks (a), parallel orientation of domains respect to the substrate (b) and perpendicular orientation of the domains to both the substrate and the trench sidewalls (c) [39].

Block copolymers are particularly attractive for semiconductor patterning applications because they can act as sacrificial templates for defining integrated circuit elements [72, 73, 74, 75].

Block copolymers self assembly provide straightforward means to achieve feature sizes below 20 nm, pitches below 40 nm and densities of 10^{11} cm^{-2}. Such an example can be the high-aspect-ratio magnetic nanowire arrays with density ~10^{12} cm^{-2} which has been fabricated by cobalt electrodeposition into thick PS-PMMA hole-array templates [76].

Lift off process can be used to fabricate lower-aspect-ratio structures instead, after sputtering deposition into the templates [40].

Pattern-transfer techniques have been demonstrated in patterning a variety of thin film materials including quantum dots array and metal dot arrays [77, 78].

Block copolymers can serve also as guiding agents to deposit functional materials: selective adsorption or chemical reaction with one of the block copolymer domains provides a method for coding spatial information into materials at nanometer-length scales. In this way it is possible to achieve spatial selectivity [79].

Furthermore BC self assembly can be used to position metal catalysts with nanometer-scale precision; such an example is the carbon nanotubes growth catalyzed by iron dot arrays which were fabricated by polyferrocenyldimethylsilane (PFS) domains in PS-*b*-PFS diblock copolymer thin films [80].

Among the several applications concerning block copolymers, shallow-trench array capacitor, engineered material optical refractive index, nanoporous membranes and nanocrystal flash memories are examples of possible device fabrication using BC technology [3]. The shallow-trench array capacitor represents an exception to the performance improvement with device shrinking since smaller device dimensions degrade performance. For example the storage capacity of a passive on-chip capacitor varies as a function of the surface area. The use of polymer self-assembly can be a valid method to increase capacitor surface area without introducing additional process complexity. Fabrication of shallow-trench-array on-chip decoupling capacitors has been obtained combining BC self-assembly, plasma etching and atomic layer deposition. This process allowed increasing capacitance even if leakage current increased as well thus demonstrating the requirement of balance between enhanced capacitance and appropriate leakage current levels [3].

Considering the principle of total internal reflection, which is the phenomenon by which light is reflected upon encountering an interface between the medium in which it is travelling and a medium with a lower index of refraction, self-assembled polymer patterns offer an alternative method to modify the optical properties of a

fraction of the films: combining BC self-assembly and plasma etching it is possible to render only a fraction of the dielectric film porous, in order to create a layered structure comprising a porous top dielectric layer over a fully dense underlying dielectric film [3, 81, 82]. The porous top layer has a reduced optical index relative to the underlying dense dielectric film, thus creating the appropriate index mismatch for a waveguide effect. In this case a low-index cladding material at the bottom interface between the dense dielectric film and the substrate is required as well in order to obtain total internal reflection.

The characteristic dimensions of block copolymers, i.e. with pore diameter below 20 nm and pore density above 10^{10} cm^{-2}, are suitable for membrane applications in fields such as high-quality molecular sorting, sensing and filtration [83, 84]. Starting from self-assembled PS template and transferring the pattern by using plasma etching it is possible to reproduce with uniformity the PS template. The flexibility of block copolymer self-assembly process allows tuning the pore diameter, which can be adjusted by changes to BC molecular weight [52, 85, 86]. Concerning the electronic devices, the template obtained using BC self-assembly can be used to fabricate Flash memory transistor: the nanostructured material will be used as charge-storage in this case [87, 88]. Nanocrystals floating-gate memories are predicted to offer better scalability than that of conventional Flash devices providing improved retention and reliability at the same program oxide thickness as well lower voltage operation. This type of device stores a memory bit in a floating gate composed of a group of electrically isolated nanoparticles rather than in a continuous floating-gate layer thus providing tolerance against defects in extremely thin oxide layers [89]. The fabrication of arrays of isolated nanocrystals involves a sequence of etches and depositions: self-assembly of BC with formation of nanoporous template, oxide etch, BC removal, Si and oxide depositions.

2.2 Atomic layer deposition

Atomic layer deposition (ALD) is a growth technique that is based on the sequential use of a gas phase chemical process.

During the process two precursors react with the surface one-at-a-time in a sequential manner. By exposing the precursors to the growth surface repeatedly, a thin film is deposited.

ALD is a self-limiting (the amount of film material deposited in each reaction cycle is constant), sequential surface chemistry that deposits conformal thin films of materials onto substrates of varying compositions. ALD is similar in chemistry to chemical vapor deposition (CVD), except that the ALD reaction breaks the CVD reaction into two half reactions, keeping the precursor materials separate during the reaction.

Due to the characteristics of self-limiting and surface reactions, ALD film growth makes atomic scale deposition control possible. By keeping the precursors separate throughout the coating process, atomic layer control of film growth can be obtained as fine as ~0.1 Å per cycle.

Separation of the precursors is accomplished by pulsing a purge gas (typically nitrogen or argon) after each precursor pulse to remove excess precursor from the process chamber.

The growth of material layers by ALD consists of four steps: exposure of the first precursor, purge or evacuation of the reaction chamber to remove the non-reacted precursors, exposure of the second precursor, purge or evacuation of the reaction chamber. Each reaction cycle adds a given amount of material to the surface, referred to as the growth per cycle. To grow a material layer, reaction cycles are repeated as many as required for the desired film thickness. One cycle may take time from 0.5 s to a few seconds and deposit between 0.1 and 3 Å of film thickness. Because of the surface control, ALD-grown films are extremely conformal and uniform in thickness.

Atomic layer deposition (ALD) was performed in a Savannah 200 reactor. Al_2O_3 films were deposited at 300°C into the SiO_2 porous backbone using trimethylaluminium (TMA) and H_2O as Al and oxygen precursors; both chemicals

were stored at room temperature. ALD cycle structure was composed of 0.2 s TMA pulse / 8 s purge with N_2 / 0.2 s H_2O pulse / 10 s purge with N_2.

The ALD pulse sequence was specifically developed for the deposition into the nanoporous templates.

The self-limiting character and the linearity of the ALD growth were verified on flat SiO_2 substrates that were introduced in the ALD reactor during each Al_2O_3 deposition in order to accurately monitor the growth and the final thickness of the films. Given an expected theoretical growth rate of ~0.9 ± 0.1 Å/cycle, film thickness was tuned by varying the number of ALD cycles between 20 and 120. Figure 2.6 depicts the four step of the ALD cycle for the growth of Al_2O_3.

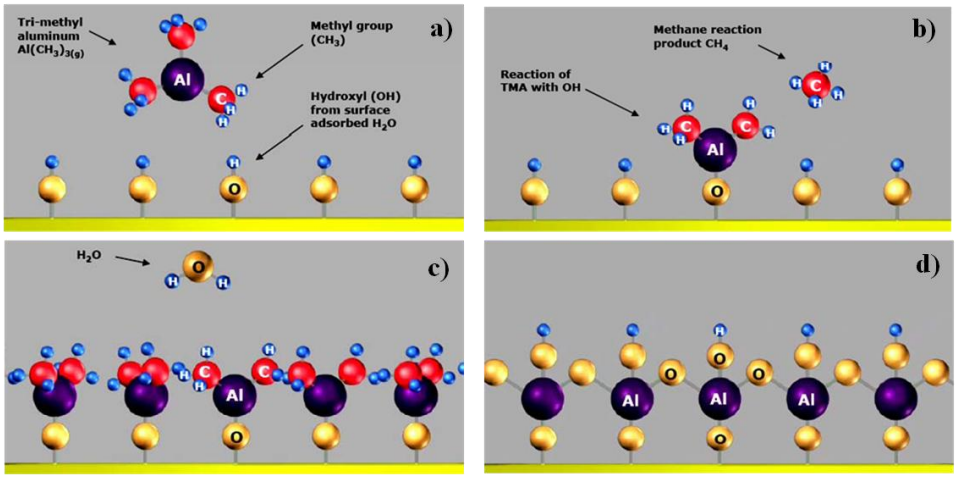

Figure 2.6 ALD cycle: exposure of the TMA (a), reaction of TMA with OH and removal of the CH_4 reaction product (b), exposure of H_2O (c), purge of the reaction chamber (d).

2.3 Ion implantation

Ion implantation is a material engineering process by which ions of a material are accelerated in an electrical field and impacted into another solid.

This process is used to change the physical, chemical, or electrical properties of the solid.

Ion implantation equipment typically consists of an ion source, where ions of the desired element are produced, an accelerator, where the ions are electrostatically accelerated to a high energy, and a target chamber, where the ions impinge on a target, which is the material to be implanted.

Thus ion implantation is a special case of particle radiation. Each ion is typically a single atom or molecule, and thus the actual amount of material implanted in the target is the integral over time of the ion current. This amount is called the dose. The currents supplied by implanters are typically small (μA), and thus the dose which can be implanted in a reasonable amount of time is small. Therefore, ion implantation finds application in cases where the amount of chemical change required is small.

Typical ion energies are in the range of 10 to 500 keV. Energies in the range 1 to 10 keV can be used, leading to a penetration of only a few nanometers or less. Energies lower than this result in very little damage to the target, and fall under the designation ion beam deposition. Higher energies can also be used: accelerators capable of 5 MeV are common. However, there is often great structural damage to the target, and because the depth distribution is broad, the net composition change at any point in the target will be small. The energy of the ions, as well as the ion species and the composition of the target, determine the depth of penetration of the ions in the solid. The average penetration depth is called the range of the ions. Under typical circumstances ion ranges will be between 10 nanometers and 1 micrometer. Thus, ion implantation is especially useful in cases where the chemical or structural change is desired to be near the surface of the target.

Ions gradually lose their energy as they travel through the solid, both from occasional collisions with target atoms (which cause abrupt energy transfers) and from a mild drag from overlap of electron orbitals, which is a continuous process. The loss of ion energy in the target is called stopping and can be simulated with the binary collision approximation method. A schematic view of ion implantation system is depicted in figure 2.7.

In order to fabricate silicon nanoscrystals ultra low energy - ion beam synthesis (ULE-IBS) has been performed: in this way too broad size distribution can be avoided [90, 91]. The implantation profile has a Gaussian distribution: nucleation occurs preferentially at the peak of the implantation profile. Formation of nanocrystals should occur in a very narrow band. By changing the energy of implantation, the position of the band respect to the substrate can be tuned.

The ULE implantation allows using very thin oxide layers and thus it is a good method for memory devices fabrication.

A thermal treatment should be performed after the implantation in order to promote nanocrystals formation.

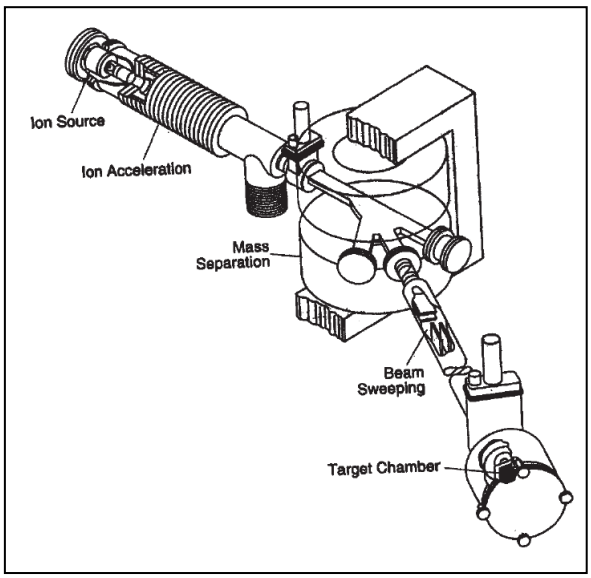

Figure 2.7 Schematic drawing of an ion implantation system.

Typically the process of ion implantation leads to the incorporation of impurity atoms as dissolved monomers in the host materials. Depending mainly on the substrate temperature, the implanted atoms may diffuse through the matrix or not. During the ion implantation process the monomer concentration increases linearly with time. As the concentration of monomers reaches the solubility threshold, small agglomerations of impurity atoms start to form and the increase of monomers slow down. These unstable agglomerates are called embryos. Due to statistical fluctuations some of them grow beyond a critical radius Rc forming stable precipitates. If the local monomer concentration around the precipitates is above the equilibrium monomer concentration, the precipitates grow by absorption of monomers from the surrounding reservoir of the dissolved impurity. When the concentration of impurity atoms decreases below the nucleation threshold no new precipitates are formed. A competitive coarsening process, the Ostwald ripening, begins. In order to minimize the total interfacial energy of the system, large nanoclusters grow at the expense of the smaller ones that finally dissolve. At very high fluence nanoclusters can be so close that they start to merge forming an almost continuous buried layer.

2.4 E-beam evaporation

The evaporation has been performed by means of EB3 evaporator. The EB3 Multihearth Electron Beam Source installed in the AUTO 306 provides the means for electron beam evaporation of materials placed in the crucible in the source. When operated, the Source generates an electron beam which is used to evaporate materials in the crucible.

The EB3 kW Power Supply consists of an EB3 Power Supply Unit and an EB3 Source Control. The EB3 Power Supply Unit provides the electrical supplies for the EB3 Multihearth Electron Beam Source. The EB3 Source Control is used to control the operation of the Source. The EB3 Beam Sweep Unit is used to scan the electron beam over the material in the crucible.

The kit contains all of the electrical and water leadthroughs and the cooling-water pipelines for the Source. The crucible in the Source can be automatically or manually rotate with the EB3 Motorised Turret Drive or the EB3 Manual Turret Drive. The EB3 Water Flow-Switch automatically switches off the Source if the cooling-water supply fails.

The Source fits in the AUTO 306 vacuum chamber and is operated when the vacuum chamber is at the appropriate pressure for evaporation. When the source is operated, high voltage electrical supplies, provided by the EB3 kW Power Supply, heat a tungsten filament until it is incandescent; the filament then spontaneously and randomly emits electrons. The anode plate then collects the electrons and forms them into a beam which is accelerated through the high voltage potential of 5 kV. Magnetic fields created by a permanent magnet and the pole pieces and pole piece extensions deflect the beam through 270° until it impacts on the material in the crucible hearth, which is at electrical ground potential. If the electron beam contains sufficient energy, the material in the crucible is evaporated. For the beam to reach the crucible, it passes through two apertures in the top shield on the Source. The permanent magnet, pole pieces and pole extensions direct the beam onto one point on the crucible hearth.

However, the Source also has beam sweep coils fitted. When energised, these coils enable the beam to be scanned across the hearth in one or both of two directions.

The EB3 Sweep Unit energises the beam sweep coils and allows controlling the deflection of the electron beam. Figure 2.8 shows the EB3 scheme.

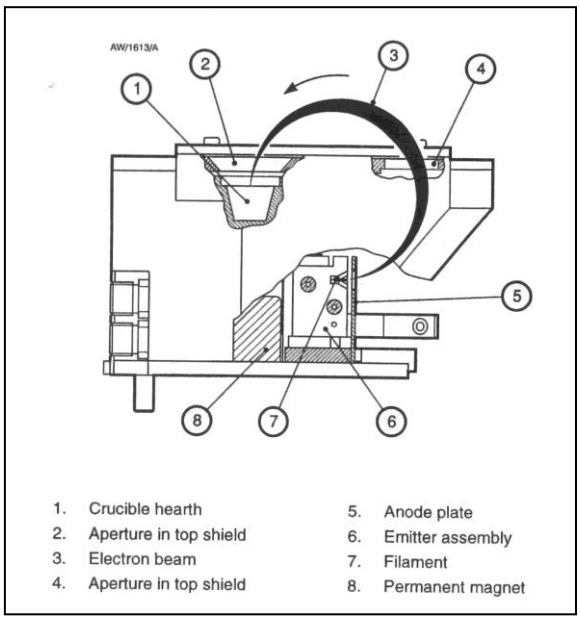

Figure 2.8 Principle of operation of the Source.

The EB3 Multihearth Electron Beam Source is a magnetically focused electron beam source. The electron beam is deflected through 270° onto hearth in the crucible by pole pieces, pole piece extensions and a permanent magnet. The magnet is next to crucible water-cooling system; this ensures that the magnet is stable and has a long life. The electron beam has a diameter of approximately 4 mm at 1 kW. A shield on the top of the Source prevents cross contamination of hearths and the Source by evaporant.

The crucible is water cooled and is mounted on a rotable turret. The EB3 Multihearth Electron Beam Source is supplied with a four hearth crucible fitted. The EB3 kW Power Supply consists of two electrical units which are supplied together: the EB3 Power Supply Unit and the EB3 Source Control. The former provides the high and low voltage electrical supplies to the EB3 Multihearth Electron Beam Source. The front panel has an electrical supply isolator, circuit breakers and indicator lamps which show when the electrical supplies to the Power Supply Unit are on. The Power Supply Unit also has indicator lamps which show when a circuit breaker has tripped, and reset buttons to reset a circuit breaker when it has tripped. Another lamp is on when the interlock signal to the Power Supply Unit is on. When the interlock signal is off, the electrical supplies to the Source are switched off. The electronic valves in the Power Supply Unit are cooled by air from

cooling-fans a lamp is on when the fans are operating. The latter is used to control the operation of the EB3 Multihearth Electron Beam Source. The front panel of the Source Control has an on/off switch for the Source Control and an on/off switch for the Source (the gun switch). A voltmeter shows the electrical voltage supplied to the Source. The beam current or the filament current supplied to the Source are shown on the ammeter. The current displayed on the ammeter is selected by the meter switch. The current supplied to the filament, and so the emission current, can be changed by the current control. The voltage adjuster allows adjusting the voltage supplied to the source. A switch on the front panel allows selecting local control, by the Source control, or remote control. Status LEDs show when the Source is on and whether the Source is remotely or locally controlled. A current adjuster on the rear of the Source Control allows presetting the maximum emission current. The EB3 Motorised Turret Drive allows to automatically rotate the crucible on the EB3 Multihearth Electron Beam Source. The Source is mounted on a baffle plate. A turret drive passes through a leadthrough in the baseplate of the AUTO306 and connects to the turret of the Source. The turret is rotated by an electric motor. Microswitches on the Motorised Turret Drive detect the position of the turret and stop the turret at the selected position. The EB3 Beam Sweep Unit allows scanning the electron beam across the hearth, in the X and Y directions. The front panel on the Sweep Control has an on/off switch, amplitude controls to control the amplitude of the X and Y deflection, frequency controls which select the frequency of the X and Y deflections and waveform selectors which select the waveform of the deflections. Two sets of LEDs show the deflection schematically. The offset adjusters allow selecting the static position of the electron beam on the hearth when there is not beam sweep selected. Once the static position has been selected, any beam sweep selected is then relative to the static position.

The thickness of the films deposited can be measured by the FTM6 Film Thickness Monitor. The FTM6 measures the resonant frequency of oscillation of the crystal. This frequency changes as the film thickness of the deposit on the crystal changes. To compensate for differences between the source-to-substrate and source-to-crystal distances and attitudes, a calibration or “tooling factor” can be programmed into the FTM6. The film thickness on the substrate can then be calculated from the film thickness on the crystal. The FTM6 can be programmed with data for two different deposition materials, including density, termination thickness and tooling

factor. Film thickness is calculated from the measured crystal resonant frequency and the default or specified deposition material density and tooling factors, as follows:

$$T_C = \frac{F \cdot D_q \cdot N_q \cdot (P_q - P_6)}{D_e} \quad (2.3)$$

where T_C is the calculated film thickness, F is the tooling factor, D_q is the density of quartz, N_q is the frequency constant of quartz, P_q is the period of loaded crystal, D_e is the density of deposition material and P_6 is the period of 6 MHz crystal.

2.5 Reactive Ion Etching

Reactive ion etching (RIE) takes place in plasma. The basic process in RIE is that plasma is established by gas discharge and contains a large number of chemically active gaseous ions. The ions interact with material atoms on the surface and produce new compounds which are volatile and evacuated by a vacuum system. Energized ions bombarding the material surface can also sputter off surface atoms, resulting in a certain degree of physical etching. Therefore RIE combines both physical and chemical etchings.

The main characteristics of RIE are the etching selectivity and the etching anisotropy. The former is the ratio of substrate etching rate to mask etching rate, the latter is represented by the ratio of etching in depth to lateral etching.

Other factors influence the RIE process, such as the flow of reactive ion gas, the discharge power, the chamber pressure, the substrate temperature, the electrode material and the loading effect [92].

A common RIE system is a planar diode electrode system in which the cathode is connected to a Radio Frequency (RF) power source by capacitance coupling. The field is typically set to a frequency of 13.56 MHz, applied at a few hundred Watts. The anode and reaction chamber are grounded. Upon applying a RF power to the diode system, a high frequency electrical field between the anode and cathode will accelerate and resonate a small number of free electrons. These electrons acquiring enough kinetic energy in the RF field will collide with gas molecules and ionize the gas molecules. Accompanying the ionization process there are also recombination

processes, i.e. electrons and ions recombine to molecules producing photons. The negative field near the cathode accelerates ions toward cathode.

Usually the chamber vacuum is at 10^{-3} Torr or lower: in this way the mean free path of electrons is longer and they can acquire more acceleration energy between two collisions with gas molecule. The higher the pressure, the more isotropic is the etching: generally at low chamber pressure ion sputtering etching dominates because chemically active gaseous molecules are less and ion energy is higher; at high chamber pressure the etching is dominated by chemical reaction because the mean free path of ions is reduced and the number of chemically active ions is large. During ion bombardment in RIE, the substrate temperature can reach 100-200 °C. Since the ions, during etching, bombard not only the substrate but also the rest of the cathode, the cathode material should be chemically inert. Otherwise a consumption of large number of active ions by the cathode would occur, affecting the etching rate. Loading effect is the non uniformity in etching rate caused by a variation of etching area. The reaction rate is directly linked to the supply rate of reactive gases. Thus when etching area has increased while the gas flow rate and other conditions remain the same, more gaseous ions are consumed without replenishment and the etching rate will decrease. Then etching conditions have to be adjusted according to the area to be etched in order to maintain the same etching rate.

2.6 Lift off

Lift-off process is a method of creating patterns of a target material on the surface of a wafer, using a sacrificial material. It is an additive process, as opposed to more traditional subtracting technique like etching, described in section 2.5.

Lift off consist of forming an inverse image of the pattern desired on the wafer using a stencil layer, which covers certain areas on the wafer and exposes the rest. The layer to be patterned is then deposited over the stenciled wafer. In the exposed areas of the stencil, the layer material gets deposited directly on the wafer substrate, while in the covered areas, the material gets deposited on top of the stencil film. After the layer material has been deposited, the wafer is immersed in a liquid that can dissolve the stencil layer. Once the stencil is dissolved by the liquid,

the layer material over it gets "lifted off", leaving behind the layer material that were deposited over the wafer substrate itself, which forms the final pattern on the wafer.

The key to successful lift-off is the ability to ensure the existence of a distinct break between the layer material deposited on top of the stencil and the layer material deposited on top of the wafer substrate. Such a separation allows the dissolving liquid to reach and attack the stencil layer. This kind of process allows depositing composite layers consisting of several different materials one material at a time and then patterned with a single lift-off. Moreover sloped side walls become possible, resulting in good step coverage.

On the other hand, the main disadvantage of the lift-off process is the difficulty of creating the required stencil patterns for successful lift-off. In this work the stencil pattern has been created by block copolymers self-assembly.

References

1. G. M. Whitesides and B. Grzybowski, *Science* **295**, 2418 (2002)

2. C. J. Hawker, T. P. Russel, *MRS Bull.* **30**, 952 (2005)

3. C. T. Black, R. Ruiz, G. Breyta, J. Y. Cheng, M. E. Colburn, K. W. Guarini, H. C. Kim, Y. Zhang, *IBM J. Res. Dev.* **51**, 605 (2007)

4. R. A. Segalman, *Mater. Sci. Eng. R* **48**, 191 (2005)

5. C. Park, J. Yoon, E. L. Thomas, *Polymer* **44**, 6725 (2003)

6. J. Y. Cheng, C. A. Ross, H. I. Smith, E. L. Thomas, *Adv. Mater.* **18**, 2505 (2006)

7. C. T. Black, *ACS Nano* **1**, 147 (2007)

8. S. Krishnamoorthy, C. Hinderling and H. Heinzelmann, *Materials Today* **9**, 40 (2006)

9. F. S. Bates and G. H. Fredrickson, *Physics Today* **52**, 32 (1999)

10. H.-C. Kim, S.-M. Park and W. D. Hinsberg, *Chem. Rev.* **110**, 146 (2010)

11. F. S. Bates, *Science* **251**, 898 (1991)

12. F.S. Bates and G. H. Fredrickson, *Annu. Rev. Phys. Chem.* **41**, 525 (1990)

13. K. W. Guarini, C. T. Black, K. R. Milkove and R. L. Sandstrom, *J. Vac. Sci. Technol. B* **19**, 2784 (2001)

14. I. W. Hamley, *The Physics of Block Copolymers*; Oxford University Press: New York (1998)

15. M. W. Matsen, M. Schick, *Phys. Rev. Lett.* **72**, 2660 (1994)

16. M. W. Matsen, M. Schick, *Macromolecules* **27**, 6761 (1994)

17. M. W. Matsen, M. Schick, *Macromolecules* **27**, 7157 (1994)

18. M. W. Matsen, F. S. Bates, *Macromolecules* **29**, 1091 (1996)

19. L. Leibler, *Macromolecules* **13**, 1602 (1980)

20. G. H. Fredrickson and E. Helfand, *J. Chem. Phys.* **87**, 697 (1987)

21. D. M. Anderson and E. L. Thomas, *Macromolecules* **21**, 3221 (1988)

22. T.Hashimoto, M. Shibayama, H. Kawai, *Macromolecules* **13**, 1237 (1980)

23. J. Melenkeviz, M. Muthukumar, *Macromolecules* **24**, 4199 (1991)

24. M. D. Whitemore, J. Noolandi, *J. Chem. Phys.* **93**, 2946 (1990)

25. G. Hadziioannou and A. Skoulios, *Macromolecules* **15**, 258 (1982)

26. A. Mathis, G. Hadziioannou, A. Skoulios, *Colloid Polym. Sci.* **257**, 136 (1979)

27. T. P. Russell, G. Coulon, V. R. Deline, D. C. Miller, *Macromolecules* **22**, 4600 (1989)

28. P. F. Green, T. M. Christensen, T. P. Russell, *Macromolecules* **24**, 252 (1991)

29. A. M. Mayes, T. P. Russell, P. Bassereau, S. M. Baker, G. I. Smith, *Macromolecules* **27**, 749 (1994)

30. S. H. Anastasiadis, T. P. Russell, S. K. Satija, C. F. Majkrzak, *J. Chem. Phys.* **92**, 5677 (1990)

31. M. J. Fasolka and A. M. Mayes, *Annu. Rev. Mater. Res.* **31**, 323 (2001)

32. J. N. L. Albert and T. H. Epps, *Materials Today* **13**, 24 (2010)

33. S. Ham, C. Shin, E. Kim, D.-Y. Ryu, U. Jeong, T. P. Russel and C. J. Hawker, *Macromolecules* **41**, 6431 (2008)

34. I. A. Zucchi, E. Poliani and M. Perego, *Nanotechnology* **21**, 185304 (2010)

35. D.-Y. Ryu, S. Ham, E. Kim, U. Jeong, C. J. Hawker and T. P. Russel, *Macromolecules* **42**, 4902 (2009)

36. T. P. Russell, G. Coulon, V. R. Deline and D. C. Miller, *Macromolecules* **22**, 4600 (1989)

37. C. De Rosa, F. Auriemma, R. Di Girolamo, G. P. Pepe, T. Napolitano and R. Scaldaferri, *Adv. Mater*. **22**, 5414 (2010)

38. E. Han, H. Kang, C.-C. Liu, P. F. Nealey and P. Gopalan, *Macromolecules* **22**, 4325 (2010)

39. S.-M. Park, M. P. Stoykovich, R. Ruiz, Y. Zhang, C. T. Black and P. F. Nealey, *Adv. Mater*. **19**, 607 (2007)

40. S. Xiao, X. Yang, E. W. Edwards, Y.-H. La and P. F. Nealey, *Nanotechnology* **16**, S324 (2005)

41. T. Thurn-Albrecht, J. DeRouchey, T. P. Russell and R. Kolb, *Macromolecules* **35**, 8106 (2002)

42. S. H. Kim, M. J. Misner, T. Xu, M. Kimura and T. P. Russell, *Adv. Mater*. **16**, 226 (2004)

43. Y. Xuan, J. Peng, L. Cui, H. Wang, B. Le and Y. Han, *Macromolecules* **37**, 7301 (2004)

44. T. Thurn-Albrecht, J. DeRouchey, T. P. Russell and H. M. Jaeger, *Macromolecules* **33**, 3250 (2000)

45. D. G. Walton, G. J. Kellogg, A. M. Mayes, P. Lambooy, T. P. Russell, *Macromolecules* **27**, 6225 (1994)

46. G. J. Kellogg, D. G. Walton, A. M. Mayes, P. Lambooy, T. P. Russell, P. D. Gallagher, S. K. Satija, *Phys. Rev. Lett.* **76**, 2503 (1996)

47. P. Mansky, Y. Liu, E. Huang, T. P. Russell, C. J. Hawker, *Science* **275**, 1458 (1997)

48. C. J. Hawker, E.Elce, J. Dao, W. Volksen, T. P. Russell and G. G. Barclay, *Macromolecules* **29**, 2686 (1996)

49. E. Huang, S. Pruzinsky, T. P. Russell, J. Mays, C. J. Hawker, *Macromolecules* **32**, 5299 (1999)

50. P. Mansky, T. P. Russell, C. J. Hawker, J. Mays, D. C. Cook, S. K. Satija, *Phys. Rev. Lett.* **79**, 237 (1997)

51. P. Mansky, T. P. Russell, C. J. Hawker, M. Pitsikalis, J. Mays, *Macromolecules* **30**, 6810 (1997)

52. K. W. Guarini, C. T. Black, S. H. I. Yeung, *Adv. Mater.* **14**, 1290 (2002)

53. S. Ham, C. Shin, E. Kim, D. Y. Ryu, U. Jeong, T. P. Russell, C. J. Hawker, *Macromolecules* **41**, 6431 (2008)

54. E. Han, K. O. Stuen, Y.-H. La, P. F. Nealey and P. Gopalan, *Macromolecules* **41**, 9090 (2008)

55. D. Y. Ryu, S. Ham, E. Kim, U. Jeong, C. J. Hawker and T. P. Russell, *Macromolecules* **42**, 4902 (2009)

56. Z. Di, D. Posselt, D.-M. Smilgies and C. M. Papadakis, *Macromolecules* **43**, 418 (2010)

57. S. H. Kim, M. J. Misner, T. Xu, M. Kimura and T. P. Russell, *Adv. Mater.* **16**, 226 (2004)

58. K. A. Cavicchi, K. J. Berthiaume, T. P. Russell, *Polymer* **46**, 11635 (2005)

59. Y. Xuan, J. Peng, L. Cui, H. Wang, B. Li and Y. Han, *Macromolecules* **37**, 7301 (2004)

60. Y. Chen, H. Huang, Z. Hu and T. He, *Langmuir* **20**, 3805 (2004)

61. A. Knoll, L. Tsarkova and G. Krausch, *Nano Lett.* **7**, 843 (2007)

62. T. Thurn-Albrecht, J. DeRouchey, T. P. Russell, H. M. Jaeger, *Macromolecules* **33**, 3250 (2000)

63. T. Thurn-Albrecht, J. DeRouchey, T. P. Russell, R.Kolb, *Macromolecules* **35**, 8106 (2002)

64. J. Y. Cheng, C. A. Ross, H. I. Smith and E. L. Thomas, *Adv. Mater.* **18**, 2505 (2006)

65. E. Han, H. Kang, C.-C. Liu, P. F. Nealey and P. Gopalan, *Adv. Mater.* **22**, 4325 (2010)

66. S. –M. Park, M. P. Stoykovich, R. Ruiz, Y. Zhang, C. T. Black and P. F. Nealey, *Adv. Mater.* **19**, 607 (2007)

67. R. A. Segalman, H. Yokoyama, E. J. Kramer, *Adv. Mater.* **13**, 1152 (2001)

68. D. Sundrani, S. B. Darling, S. J. Sibener, *Nano Lett.* **4**, 273 (2004)

69. R. A. Segalman, A. Hexemer, E. J. Kramer, *Macromolecules* **36**, 6831 (2003)

70. J. Y. Cheng, C. A. Ross, E. L. Thomas, H. I. Smith, G. J. Vancso, *Appl. Phys. Lett.* **81**, 3657 (2002)

71. J. Y. Cheng, F. Zhang, H. I. Smith, G. J. Vancso, C. A. Ross, *Adv. Mater.* **18**, 597 (2006)

72. I. W. Hamley, *Nanotechnology* **14**, R39 (2003)

73. C. Harrison, M. Park, P. M. Chaikin, R. A. Register and D. H. Adamson, *J. Vac. Sci. Technol. B* **16**, 544 (1998)

74. M. Lazzari and M. A. Lopez-Quintela, *Adv. Mater.* **15**, 1583 (2003)

75. M. Li, A. C. Christopher and K. O. Christopher, *Adv. Polymer Sci.* **190**, 183 (2005)

76. T. Thurn-Albrecht, J. Schotter, C. A. Kastle, N. Emley, T. Shibauchi, L. Krusin-Elbaum, K. Guarini, C. T. Black, M. T. Tuominen and T. P. Russell, *Science* **290**, 2126 (2000)

77. R. R. Li. P. D. Dapkus, M. E. Thompson, W. G. Jeong, C. Harrison, P. M. Chaikin, R. A. Register and D. H. Adamson, *Appl. Phys. Lett.* **76**, 1689 (2000)

78. J. P. Spatz, T. Herzog, S. Mossmer, P. Ziemann and M. Moller, *Adv. Mater.* **11**, 149 (1999)

79. W. A. Lopes and H. M. Jaeger, *Nature* **414**, 735 (2001)

80. C. Hinderling, Y. Keles, T. Stockli, H. E. Knapp, T. de los Arcos, P. Oelhafen, I. Korczagin, M. A. Hempenius, G. J. Vancso, R. Pugin and H. Heinzelmann, *Adv. Mater.* **16**, 876 (2004)

81. A. Loni, L. T. Canham, M. G. Berger, R. Arens-Fischer, H. Munder, H. Luth, H. F. Arrand and T. M. Benson, *Thin Solid Films* **276**, 143 (1996)

82. A. Jain, S. Rogojevic, S. Ponoth, N. Agarwal, I. Matthew, W. N. Gill, P. Persans, M. Tomozawa, J. L. Plawsky and E. Simonyi, *Thin Solid Films* **398-399**, 513 (2001)

83. T. A. Desai, D. J. Hansford, L. Kulinsky, A. H. Nashat, G. Rasi, J. Tu, W. Yuchun, Z. Miqin and M. Ferrari, *Biomed. Microdevices* **2**, 11 (1999)

84. L. Leoni, A. Boiarski and T. A. Desai, *Biomed. Microdevices* **4**, 131 (2002)

85. T. Xu, H.-C. Kim, J. DeRouchey, C. Seney, C. Levesque, P. Martin, C. M. Stafford and T. P. Russell, *Polymer* **42**, 9091 (2001)

86. C. T. Black, K. W. Guarini, G. Breyta, M. C. Colburn, R. Ruiz, R. L. Sandstrom, E. M. Sikorski and Y. Zhang, *J. Vac. Sci. Technol. B* **24**, 3188 (2006)

87. C. T. Black, K. W. Guarini, R. Ruiz, E. M. Sikorski, I. V. Babich, R. L. Sandstrom and Y. Zhang, *IEEE IEDM Tech. Digest*, 16.3 (2007)

88. K. W. Guarini, C. T. Black, Y. Zhang, I. V. Babich, E. M. Sikorski and L. M. Gignac, *IEEE IEDM Tech. Digest*, 22.2.1 (2003)

89. S. Tiwari, F. Rana, H. Hanafi, A. Hartstein, E. F. Crabbe and K. Chan, *Appl. Phys. Lett.* **68**, 1377 (1996)

90. A. Nakajima, T. Futatsugi, N. Horiguchi, and N. Yokoyamaa, *Jpn. J. Appl. Phys.*, **36**, L1551 (1997)

91. A. Nakajima, T. Futatsugi, H. Nakao, T. Usuki, N. Horiguchi and N. Yokoyamaa, *J. Appl. Phys.*, **84**, 1316 (1998)

92. Zheng Cui, *Micro-Nanofabrication*, Springer (2005)

Chapter 3

Characterization techniques

The fabrication and study of nanostructures with dimensions equal or below 20 nm requires the use of advanced characterization techniques to determine the chemical, structural and functional properties of these materials. Block copolymer characterization was routinely performed by scanning electron microscopy (SEM) and ellipsometry (SE) during the polymeric film deposition in order to control all the steps of the polymeric film fabrication. SE provides accurate measurements of the random and block copolymer film thicknesses. These measurements were necessary in order to verify the proper deposition and effective thermal treatments of the random copolymer, which provides neutralization of the substrate in order to induce perpendicular orientation of the cylindrical and lamellar block-copolymers. Thickness measurements of the PS-b-PMMA film after spin coating were routinely performed to verify that the film thickness is adjusted in order to induce perpendicular orientation of the cylindrical/lamellar block copolymer thin films. The combination of SE and SEM analyses allowed the optimization of the protocols for the fabrication of the nanoporous and lamellar PS matrices. On the other side, various experimental techniques were used for the structural, chemical and electro-optical characterization of the semiconducting nanostructures fabricated using block-copolymer self assembly. To this end scanning electron microscopy, spectroscopic ellipsometry, transmission electron microscopy, time of flight secondary ion mass spectroscopy and atomic force microscopy were extensively used. In the following sections a brief description of these techniques is reported in order to elucidate the contributions of each experimental technique to the present work.

3.1 Scanning Electron Microscopy

A scanning electron microscope is a type of electron microscope that images a sample by scanning it with a high-energy beam of electrons in a raster scan pattern. The electrons interact with the atoms that make up the sample producing signals that contain information about the sample's surface topography, composition, and other properties such as electrical conductivity. The types of signals produced by an SEM include secondary electrons (SE), back-scattered electrons (BSE), characteristic X-rays, light (CL), specimen current (SC) and transmitted electrons (TE). Figure 3.1 depicts a schematic view of signals produced by SEM.

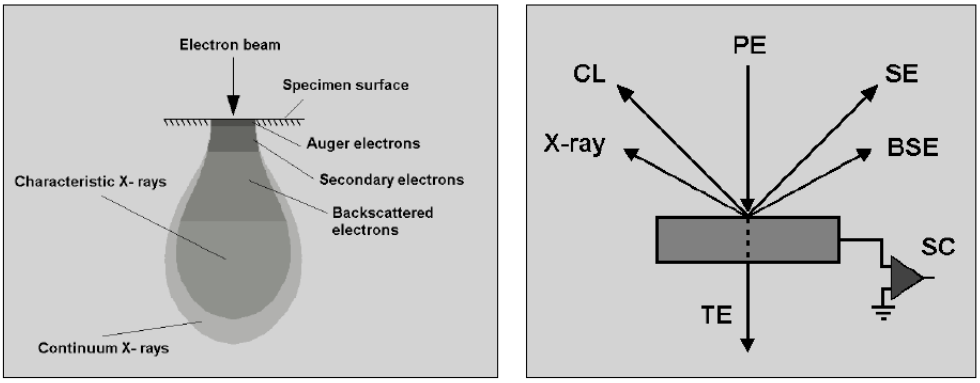

Figure 3.1 Schematic view of signals produced by SEM.

The signals result from interactions of the electron beam with atoms at or near the surface of the sample. In the most common or standard detection mode, secondary electron imaging (SEI), the SEM can produce very high-resolution images of a sample surface, revealing details less than 1 nm in size. Due to the very narrow electron beam, SEM micrographs have a large depth of field yielding a characteristic three-dimensional appearance useful for understanding the surface structure of a sample. A wide range of magnifications is possible, from about 10 times (about equivalent to that of a powerful hand-lens) to more than 500,000 times, about 250 times the magnification limit of the best light microscopes.

Secondary electrons (SE) are low energy electrons (<50 eV) and they are generated by inelastic scattering of primary electrons (PE) on the atomic core or on the electrons of the atomic shell of the sample material. Back-scattered electrons (BSE) are beam electrons that are reflected from the sample by elastic scattering. They have energy higher than 50 eV and carry depth information. BSE are often used in

analytical SEM along with the spectra made from the characteristic X-rays to obtain information about the chemical composition of the sample. Because the intensity of the BSE signal is strongly related to the atomic number (Z) of the specimen, BSE images can provide information about the distribution of different elements in the sample. Characteristic X-rays are emitted when the electron beam removes an inner shell electron from the sample, causing a higher energy electron to fill the shell and release energy. These characteristic X-rays are used to identify the composition and measure the abundance of elements in the sample.

Figure 3.2 shows the Supra 40 Gemini® FE-SEM used in this thesis work to characterize the nanostructures. Supra 40 is a field emission (FE) SEM based on the highly performing Gemini® column, which delivers nanoscale high resolution imaging over the entire voltage range (from 20 eV up to 30 keV). The core of an electron optical system is the *accelerating column*. It mainly consists of the following sub-system: *emitter gun, condenser lenses, shutter, field lenses, aperture, projector lens, deflecting coils, secondary electron detector*. The electron gun consists of three components: a cathode for emitting the electrons, an extractor anode and a cathode lens to collect the emitted electrons into a beam.

More specifically, there exist three types of cathode: the thermionic (TE-C), the field emission (FE-C) (also called *cold cathode*) and the thermal field emission (TFE-C) cathode. All of them are generally made either tungsten (W) or LaB_6. A TE-C uses high temperature (1600 °C – 2500 °C) to provide electrons enough kinetic energy to overcome the work function barrier to escape from the tip into the free space. The emission area of a TE-C is normally between 5 μm and 15 μm. The cathode lens collects the electron cloud to form, through a crossover, an electron beam. The distance between such crossover point and the cathode tip is usually referred to as *virtual source* (VS) whose size and position is used to compare the cathode emitting properties. FE-C are needles sharper than TE-C, whose apex is normally less than 100 nm of radius and the VS size is just a few nanometers. The sharper the needle the higher the electrical field at the needle end even at low extractor voltage (the field strength is usually 10^8 V/m). Because the emission area is so small, there is no more need of a cathode lens to shrink the emitted electrons cloud as in the TE-C case. Figure 3.3 evidences the differences between them. The FE-C working temperature is about 30 °C, that is why they are named *cold*. The low working temperature of FE-C ensures a long lifetime but, on the other hand,

makes the beam current much sensitive to the gaseous impurities. For this reason ultra high vacuum is required for FE-C (10^{-10} Torr) while TE-C can work even at higher pressures (10^{-6} Torr) [1]. The first three columns of the table 3.1 provide the main features comparison for the W or LaB_6 TE cathode and a W cold cathode. The Leo Gemini® column, presented in 1992 by Carl Zeiss Inc., has some differences respect to a standard column [2]. The beam generator is a TFE-C made by a ZrO/W junction and known as *Schottky emitter* or *Schottky FE* cathode. The Schottky FE tip consists of a <100> tungsten crystal oriented along the tip direction with a sintered reservoir of zirconium oxide in the shank. The tip is mounted over a bent filament which warms up to about 1500 °C to ensure a lower sensitivity to impurities and less restricting vacuum conditions. If an electric field is then generated (*extraction voltage*) the high temperature allows the ZrO to drift from the shank to the sharp end so that it forms a fine tip. The VS radius is only about 15 nm. The ZrO reduces the extraction work function from 4.6 eV (W) to 2.48 eV. All around the TFE-C, except of around the tip, a suppressor electrode is placed. This electrode collects the electrons which have not been emitted by the ZrO tip as depicted in figure 3.4. The Schottky emitter has been developed to overcome the weaknesses of cold cathodes. It combines high beam brightness and low energy spread of the FE-C together with long term current stability and low beam noise. The required capability to deliver much higher probe currents is a consequence of a 100 times larger tip area than that of a FE-C cathode. These conditions permit the Schottky FE emitters to get a very low current noise and current drift. The fourth column of table 3.1 lists the operating parameters and performance of this emitter type.

Emitter type	Thermionic	Thermionic	Cold FE	Schottky FE
Cathode material	W	LaB_6	W(310)	ZrO/W (100)
Operating temperature, K	2800	1900	300	1800
Cathode radius, nm	60,000	10,000	≤100	≤1000
Effective source radius, nm	15,000	5,000	2.5(a)	15 (a)
Emission current density, A/cm²	3	30	17,000	5300
Total emission current, μA	200	80	5	200
Normalized brightness, A/cm²sr.kV	1.10^4	1.10^5	2.10^7	1.10^7
Maximum probe current, nA	1000	1000	0.2	20
Energy spread at the cathode, eV	0.59	0.40	0.26	0.31
Energy spread at the gun exit, eV	1.5-2.5	1.3-2.5	0.3-0.7	0.35-0.71
Beam noise, %	1	1	5-10	1
Emission current drift, %/h	0.1	0.2	5	<0.5
Operating vacuum, kPa	$\leq 1.10^{-5}$	$\leq 1.10^{-6}$	$\leq 1.10^{-10}$	$\leq 1.10^{-8}$
Cathode life, hours	200	>500	>2000	>2000
Cathode regeneration	Not required	Not required	Every 6 to 8 h	Not required
Sensitivity to external influence	Minimal	Minimal	High	Low

Table 3.1 Typical operating parameters and performances of various emitter guns.

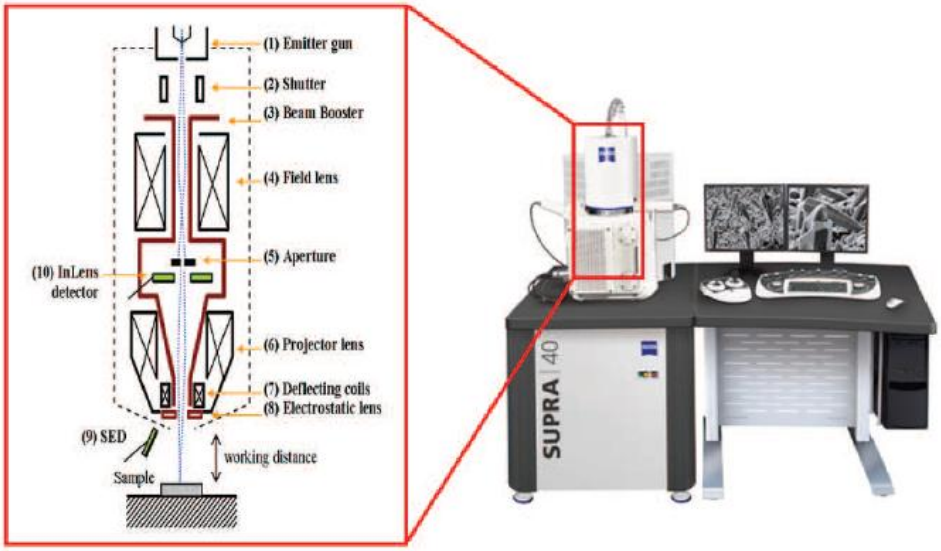

Figure 3.2 Supra 40 Gemini® FE-SEM (right picture) with schematic view of the SEM column (left picture).

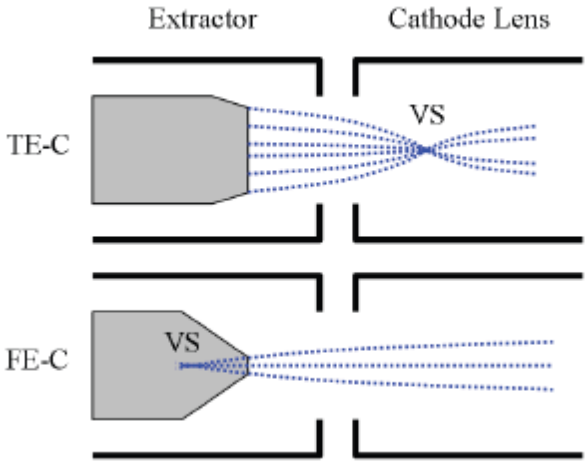

Figure 3.3 Position of virtual source (VS) in TE-C and in FE-C.

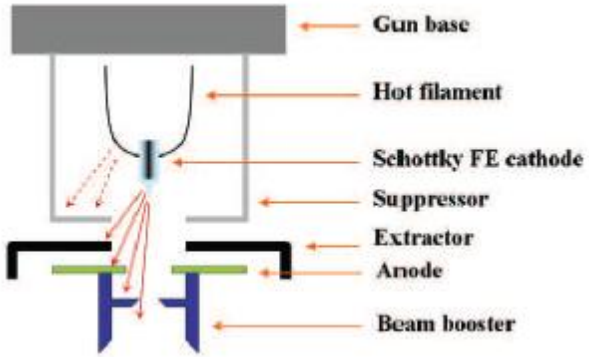

Figure 3.4 Schottky field emission gun in Gemini® column.

The condenser lenses converges the electrons emitted by the electron gun so that they can arrive at the exposure surface in maximum numbers over the smallest size. Due to the stronger focusing power and lower aberration of magnetic field respect to electrostatic field, the condenser lenses are typically made by coils winded over a soft iron core. Small gaps in the iron cores let the magnetic field fringes to interact with the travelling electrons so that Lorentz's forces are used to thinner the beam spot size. The shutter is an electron deflector through which the beam can be switched off. Because magnetic fields implies hysteresis phenomena, residual field even at zero current, and the response to a variation is much slower respect to the case of electric field, the shutter is normally made by an electrostatic deflector. Some hundreds of volt are applied to quickly drive the beam off the column axis so that the travelling electrons cannot reach anymore the target. Field lenses are magnetic lenses used for adjusting the focal plane and correct column aberrations. The working principle is the same as for the optical lenses. Several apertures can be used in an electron column to select the desired beam current reaching the sample surface. The bigger the aperture the higher the current and the signal to noise ratio (S/N) of SEM images. The projector lens is the final lens, which focuses the electron beam coming out from the aperture. In order to properly focus the beam over the sample surface it is necessary to adjust the electronic focus with the *working distance* (WD) that is the distance between the end of the column and the top of the sample.

Deflecting coils provide beam deflection. They can be placed before, after or inside the projector lens. Secondary electron detector (SED) detects primary electrons which hit the sample. Another important improvement of the Leo Gemini® column

is the beam booster, depicted in figure 3.4. Electrons created in the Schottky gun are accelerated to the set acceleration voltage on their passage to the anode. The beam booster is always held at 8 kV if the anode potential is below or equal to 20kV. In this way, electrons always travel under an accelerating voltage of at least 8kV inside the column. This considerably reduces the sensitivity of the electron beam to magnetic stray fields, thus inducing fewer aberrations, and the electron probe diameter. In addition to the beam booster, the Gemini column has the *objective lens* that consists of a combined electrostatic and electromagnetic lens duplet. Before the beam goes out of the column the electrostatic lens create an opposing field which reduces the potential of the electrons by 8kV. The energy of the electrons reaching the sample surface therefore corresponds to that set by the anode acceleration voltage. Moreover the magnetic projector lens is shaped in order decrease the magnetic stray field on the sample surface so that fewer aberrations affect the beam onto the sample. Another important characteristic of the Leo Gemini® column is the presence of an annular secondary electron detector along the booster column, namely the *InLens* detector. The retarding field of the electrostatic objective lens acts as a collector for the electrons scattered by the sample surface. These backward travelling electrons are deflected out of the column axis by the tapered magnetic lens and they are collected onto the *Inlens* detector. The process is described in figure 3.5. By means of that deflection the crossover between forward and backward travelling electrons is minimized, resulting is an increased S/N signal.

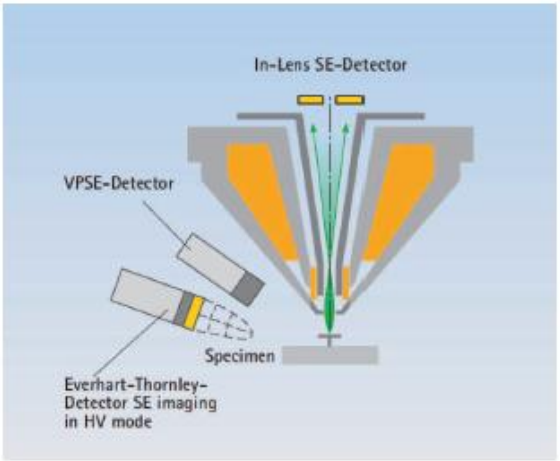

Figure 3.5 Backward scattered electrons addressed toward *InLens* detector in a Gemini® column.

3.2 Spectroscopic Ellipsometry

Spectroscopic ellipsometry (SE) is an optical technique for the investigation of the optical properties and thickness of thin films [3]. It has applications in many different fields, from semiconductor physics to microelectronic and biology, from basic research to industrial applications.

As an optical technique, spectroscopic ellipsometry is non-destructive and contactless. Upon the analysis of the change of polarization of light, which is reflected off a sample, ellipsometry can yield information about layers that are thinner than the wavelength of the probing light itself, even down to fraction of monolayers. Ellipsometry can probe the complex refractive index, which gives access to fundamental physical parameters and it is related to a variety of sample properties, including morphology, crystal quality and even chemical composition or electrical conductivity.

It is commonly used to characterize film thickness for single layers or complex multilayer stacks ranging from a few Å or tenths of nm to several μm with an excellent accuracy. The name "ellipsometry" stems from the fact that the most general state of polarization is elliptic. SE can employ broad band light sources, which cover a certain spectral range in the infrared, visible or ultraviolet spectral region. By that, the complex refractive index in the corresponding spectral region can be obtained, thus giving access to a large number of fundamental physical properties [4, 5, 6, 7].

Ellipsometry is based on the analysis of the polarization state of a beam of light that is emitted by a lamp and linearly polarized by a polarizer. It can pass through an optional compensator (retarder, quarter wave plate) and then falls onto a sample. After reflection the radiation passes an optional compensator and a second polarizer, which is called an analyzer, and falls into the detector. The schematic setup of an ellipsometry experiment is depicted in figure 3.6. Instead of the compensators some ellipsometers use a phase-modulator in the path of the incident light beam. Ellipsometry is a specular optical technique in the sense that the angle of incidence is equal to the angle of reflection. The incident and the reflected beam span the *plane of incidence*. Light which is polarized parallel to this plane is named *p-polarized*. A polarization direction perpendicular is called *s-polarized*. The nature

of the polarization change of the light is determined only by the sample's properties such as thickness and optical constants. Polarization state of the light incident upon the sample may be decomposed into the *s* and a *p* component. The amplitudes of these components, after reflection and normalized to their initial value, are denoted by *Rs* and *Rp*, respectively. SE actually measures the ratio of *Rs* and *Rp*, which is described by the fundamental equation of ellipsometry:

$$\rho = \frac{Rp}{Rs} = tan\Psi e^{i\Delta} \qquad (3.1)$$

TanΨ and Δ are the amplitude ratio and the phase shift (difference) upon reflection, respectively. Since SE is measuring the ratio of two values rather than their absolute values, it is very robust, accurate and reproducible.

SE is indeed an indirect method; in general the measured Ψ and Δ cannot be converted directly into the optical constants of the sample and a model analysis must be performed. Thus a layer model must be established, which considers the optical constants and thickness parameters of all individual layers of the sample including the correct layer sequence. The sample is assumed to be composed by a certain number of discrete and defined layers that are homogeneous and isotropic. By using an iterative procedure (least-squares minimization) unknown optical constants and/or thickness parameters are varied, and Ψ and Δ values are calculated. The calculated Ψ and Δ values which match the experimental data best provide the optical constants and thickness parameters of the sample. A comparison of the experimental and modeled data is shown in Figure 3.7. In order to quantify how well the data generated by the optical model fit, and thus agree, with the experimental measured Ψ and Δ spectra it is introduced the concept of Mean Squared Error (MSE) value. Basically, the MSE sums over all the SE wavelengths the differences between the experimental and the model data. The lower the MSE value, the better the agreement between the experimental and model generated SE data [8]. Among the different models which can be used to achieve thickness information, the *Cauchy layer* is the most indicated for the measure of transparent thin film, such as block copolymer films. The *Cauchy layer* is a commonly used layer for determining the optical constants of a transparent or partially transparent film, such as dielectrics and semiconductors below the fundamental band-gap. Considering a limited spectral range, the optical constants of these materials can be

represented by an index (*n*) which slowly varies as a function of wavelength plus an exponential absorption tail (*k*). The index of refraction of the Cauchy layer is represented by an inverse power series containing only even terms and the extinction coefficient is represented by a simple exponential tail. The index of refraction (*n*) can be expressed by the equation:

$$n(\lambda) = A + \frac{B}{\lambda^2} + \frac{C}{\lambda^4} \qquad (3.2)$$

Here λ is expressed in μm. A, B, C parameters are variable fit parameters that determine the index dispersion. The extinction coefficient (*k*) can be expressed by the equation:

$$k(\lambda) = K_A exp\left[1.24\ K_E\left(\frac{1}{\lambda} - \frac{1}{Band\ Edge}\right)\right] \qquad (3.3)$$

Here the *Band Edge* is expressed in μm. K_A and K_E are fit parameters for determining the shape of the extinction coefficient dispersion. The *Band Edge* parameter represents the extension coefficient and even if normally it can be set manually, it is not a fit parameter since it is directly correlated to the K_A. In fact (*k*) is equal to K_A at the *Band Edge*. The Effective Medium Approximation (EMA) layer model describes the macroscopic properties of a medium based on the properties and the relative fractions of its components. It is used to mix together the optical constants of two or three materials. This model is particularly useful to determine the fraction of nanoporous surface in block copolymer masks. Commercial software provides three different EMA mixing methods for the user to choose from [9]. These are a simple Linear combination, Bruggeman EMA and Maxwell-Garnet EMA. The Linear mixing simply interpolates between the constituents dielectric functions to get the optical constants of the composite material. The Maxwell-Garnett EMA and Bruggeman EMA are the most common. The Maxwell-Garnett assumes spherical inclusions of materials two and three which exist in a host matrix of material one. The Bruggeman EMA makes the self consistent choice of the host material. The Maxwell-Garnett EMA and Bruggeman EMA are very useful for modeling surface and interfacial roughness as well as modeling polycrystalline materials by mixing together amorphous and crystalline optical constants of the material.

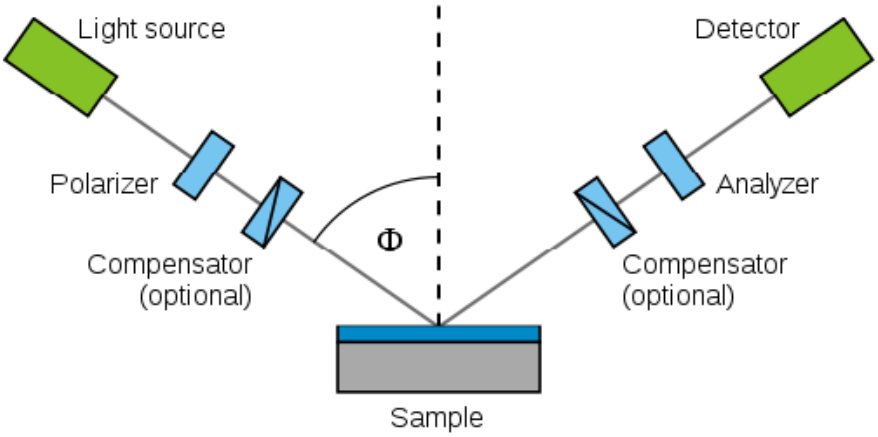

Figure 3.6 Schematic setup of an ellipsometry experiment.

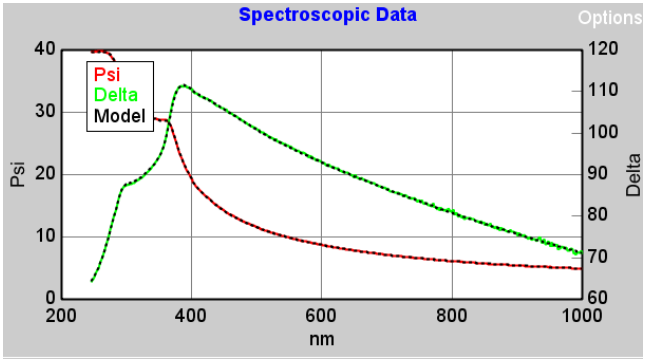

Figure 3.7 Ψ and Δ SE spectra: experimental (red and green) and model (dotted) curves.

3.3 Transmission Electron Microscopy

Transmission electron microscopy (TEM) is a microscopy technique whereby a beam of electrons is transmitted through an ultra thin specimen, interacting with the specimen as it passes through.

An image is formed from the interaction of the electrons transmitted through the specimen; the image is magnified and focused onto an imaging device, such as a fluorescent screen, on a layer of photographic film, or to be detected by a sensor such as a CCD camera.

TEMs are capable of imaging at a significantly higher resolution than light microscopes, owing to the small de Broglie wavelength of electrons. This enables the instrument's user to examine fine detail, even as small as a single column of

atoms, which is tens of thousands times smaller than the smallest resolvable object in a light microscope. TEM forms a major analysis method in a range of scientific fields, in both physical and biological sciences. At smaller magnifications, TEM image contrast is due to absorption of electrons in the material, due to the thickness and composition of the material. At higher magnifications complex wave interactions modulate the intensity of the image. Alternate modes of use allow the TEM to observe modulations in chemical identity, crystal orientation, electronic structure and sample induced electron phase shift as well as the regular absorption based imaging. TEM utilizes a stationary, coherent electron beam which passes through a sample forming a magnified image of the sample [10, 11]. The main strength of TEM is its extremely high resolution due to the very small wavelength of electrons:

$$\lambda_e = \frac{h}{mv} = \frac{h}{\sqrt{2qmV}} = \frac{1.22}{\sqrt{V}}\ (nm) \qquad (3.4)$$

where v is the electron velocity, V the accelerating voltage, m the electron mass, h the Plank's constant and q the electron charge. An approximated estimation of the resolution s can be obtained using the relation:

$$s = 0.61\lambda/NA \qquad (3.5)$$

In optical microscopy, the numerical aperture NA≈1 and λ ≈500 nm give a resolution s≈300 nm. In electron microscopy due to larger electron imperfections NA is approximately 0.01 but the wavelength is shorter: for V=100 keV, λ is 0.004 nm giving a resolution s≈0.25 nm. A schematic of TEM is shown in figure 3.8. From the top down, TEM consists of an emission source, which may be a tungsten (W) filament, or a lanthanum hexaboride (LaB_6) source. For tungsten, this will be of the form of either a hairpin-style filament or a small spike-shaped filament while LaB_6 sources utilize small single crystals. The two types of emissions source are depicted in figure 3.9. By connecting this gun to a high voltage source (from 100 to 400 kV) the gun will, given sufficient current, begin to emit electrons either by thermionic or field electron emission into the vacuum. This extraction is usually aided by the use of a Wehnelt cylinder. Once extracted, the upper lenses of the TEM lead to the formation of the electron probe to the desired size and location for

later interaction with the sample. Manipulation of the electron beam is performed using two physical effects. The interaction of electrons with a magnetic field will cause electrons to move according to the right hand rule, thus allowing electromagnets to manipulate the electron beam. Additionally, electrostatic fields can cause the electrons to be deflected through a constant angle. Coupling of two deflections in opposing directions with a small intermediate gap allows the formation of a shift in the beam path, this being used in TEM for beam shifting, subsequently this is extremely important to scanning transmission electron microscope (STEM). From these two effects, as well as the use of an electron imaging system, sufficient control over the beam path is possible for TEM operation. The optical configuration of a TEM can be rapidly changed, unlike that for an optical microscope, as lenses in the beam path can be enabled, have their strength changed, or be disabled entirely simply via rapid electrical switching. Typically a TEM consists of three stages of lensing: the condensor lenses, the objective lenses and the projector lenses. The condensor lenses are responsible for primary beam formation while the objective lenses focus the beam that comes through the sample itself. The projector lenses are used to expand the beam onto the phosphor screen or other imaging device, such as film. The magnification of the TEM is due to the ratio of the distances between the specimen and the objective lens' image plane.

Imaging systems in a TEM consist of a phosphor screen, which may be made of fine (10-100 μm) particulate zinc sulphide for direct observation by the operator. A TEM is composed of several components, which include a vacuum system in which the electrons travel, an electron emission source for generation of the electron stream, a series of electromagnetic lenses, as well as electrostatic plates. The latter two allow the operator to guide and manipulate the beam as required. Also required is a device to allow the insertion into, motion within, and removal of specimens from the beam path. The sample is placed on a copper grid of 3 mm in diameter. The sample must be sufficiently thin (100-200 nm) to be transparent to electrons. Imaging devices are subsequently used to create an image from the electrons that exit the system. To increase the mean free path of the electron gas interaction, a standard TEM is evacuated to low pressures, typically on the order of 10^{-4} Pa. The need for this is twofold: first the allowance for the voltage difference between the cathode and the ground without generating an arc and secondly to reduce the

collision frequency of electrons with gas atoms to negligible levels. TEM components such as specimen holders and film cartridges must be routinely inserted or replaced requiring a system with the ability to re-evacuate on a regular basis. As such, TEMs are equipped with multiple pumping systems and airlocks and are not permanently vacuum sealed. The vacuum system for evacuating a TEM to an operating pressure level consists of several stages. Initially a low or roughing vacuum is achieved with either a rotary vane pump bringing the TEM to a sufficiently low pressure to allow the operation of a turbomolecular pump which brings the TEM to its high vacuum level necessary for operations. Sections of the TEM may be isolated by the use of gate valves, to allow different vacuum levels in specific areas, such as a higher vacuum of 10^{-4} to 10^{-7} Pa or higher in the electron gun in high resolution or field emission TEMs. High-voltage TEMs require ultra high vacuums on the range of 10^{-7} to 10^{-9} Pa to prevent generation of an electrical arc, particularly at the TEM cathode. As such for higher voltage TEMs a third vacuum system may operate, with the gun isolated from the main chamber either by use of gate valves or by the use of a differential pumping aperture. The differential pumping aperture is a small hole that prevents diffusion of gas molecules into the higher vacuum gun area faster than they can be pumped out. For these very low pressures either an ion pump is used. The electron gun is formed from several components: the filament, a biasing circuit, a Wehnelt cap, and an extraction anode. By connecting the filament to the negative component power supply, electrons can be "pumped" from the electron gun to the anode plate, and TEM column, thus completing the circuit. The gun is designed to create a beam of electrons exiting from the assembly at some given angle, known as the gun divergence semiangle, α. By constructing the Wehnelt cylinder such that it has a higher negative charge than the filament itself, electrons that exit the filament in a diverging manner are, under proper operation, forced into a converging pattern the minimum size of which is the gun crossover diameter. The thermionic emission current density, *J*, can be related to the work function of the emitting material as described in the equation 3.6, where *A* is a constant, Φ is the work function and T is the temperature of the material.

$$J = AT^2 exp\left(-\frac{\Phi}{kT}\right) \qquad (3.6)$$

The equation 3.6 shows that in order to achieve sufficient current density it is necessary to heat the emitter. For this reason materials with either a high melting point, such as tungsten, or those with a low work function (LaB_6) are required for the gun filament.

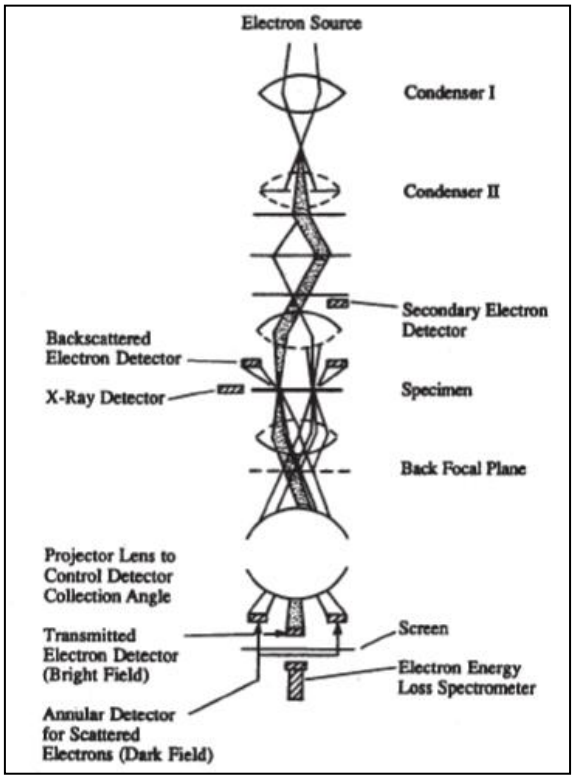

Figure 3.8 Schematic drawing of a typical TEM [11].

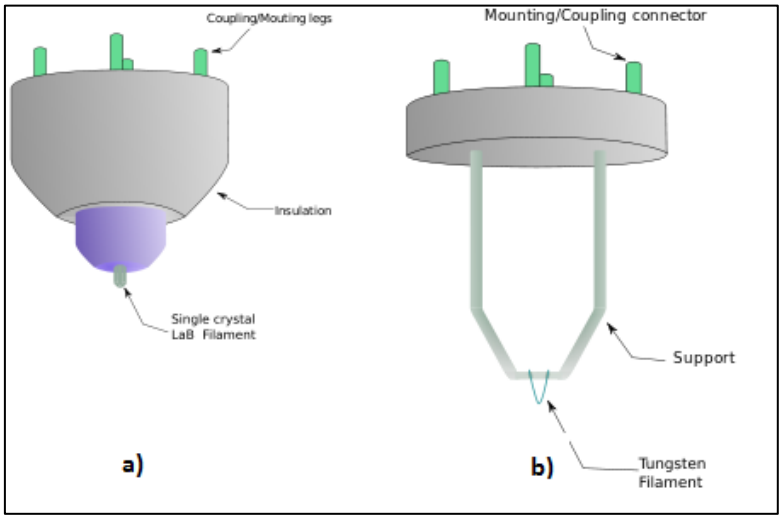

Figure 3.9 Single crystal LaB_6 filament (a) and hairpin style tungsten filament (b).

There are three primary imaging modes: bright field, dark field and high resolution microscopy. The image contrast is related to scattering and diffraction of electron in the sample. Images formed using only the transmitted electrons are bright field images while images formed using a specific diffracted beam are dark field images. The absorption of a small fraction of the electrons induces sample heating that could lead to a modification of the sample during the measurement. High resolution images are obtained combining the transmitted and a number of diffracted beams to form an interference image in the image plane of the objectives lens. High resolution transmission electron microscopy (HRTEM) gives structural information on the atomic size level. Microanalytical and structural information can be obtained by electron energy loss spectroscopy (EELS), an absorption spectroscopy based on the analysis of the distribution of electron energies for electron transmitted through the sample. EELS relies on the measurement of electron energy loss due to inelastic collisions. The EELS spectrum contains three different groups of peaks: the zero loss peak containing no useful information, the low energy loss peak due primarily to plasmons, and the high energy loss peaks due to inner shell ionization. EELS images are generated by displaying the intensity of a particular energy of the spectrum.

Sample preparation in TEM is a complex procedure because the sample must be very thin. The preparation details are shown in figure 3.10. In HRTEM the thickness of a silicon sample should be less than 10 nm operating at 200 keV. Traditionally mechanical lapping, polishing and ion milling has been used. A recent addition to sample preparation is the focused ion beam (FIB) instrument. Ga+ ions are rastered over a given portion of a sample and the incident ion cause a hole to be milled into the sample. This sample can be precisely located allowing one particular part of the sample to be examined. There is however a question of whether the ion bombardment of the FIB perturbs the sample. The surface of the sample may become amorphous and contain a high density of Ga. Nevertheless FIB has become a routine sample preparation technique.

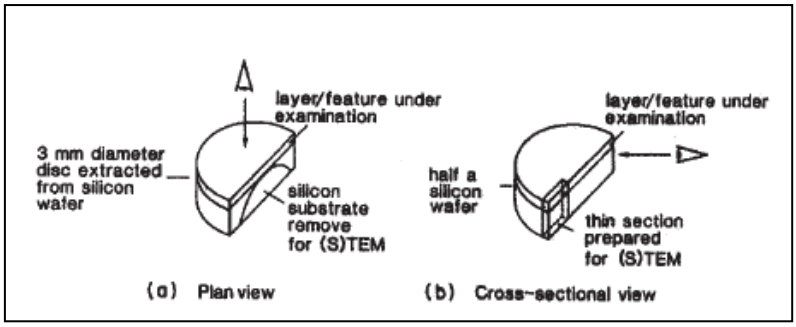

Figure 3.10 Plan view (a) and cross-section view (b) geometry used in TEM analyses [10].

3.4 ToF SIMS

Secondary ion mass spectrometry (SIMS) is a technique used in materials science and surface science to analyze the composition of solid surfaces and thin films by heavy particle bombardment of the surface of the specimen with a focused primary ion beam and collecting and analyzing ejected secondary ions.

A schematic of SIMS instrumentation is depicted in figure 3.11. These secondary ions are measured with a mass spectrometer to determine the elemental, isotopic, or molecular composition of the surface.

SIMS is the most sensitive surface analysis technique, being able to detect elements present in the parts per billion range. The mass/charge ratio (m/e) is analyzed by different type of mass analyzers obtaining a mass spectrum. The (m/e) spectrum supplies information on the chemical composition of the bombarded area. The emission processes induced by ion bombardment include electrons, photons and surface particles. The escape depth of the sputtered atoms is generally a few monolayers leading to a very high surface sensitivity which is one of the important features of secondary ion mass spectrometry.

The use of a time of flight (TOF) mass analyzer allows increasing the ion collection by a three order of magnitude. This kind of mass spectrometer is based on the principle that ions with the same energy but different masses need different flight times to pass a certain drift. Therefore by measuring the flight time of these ions the respective mass/charge ratio can be determined. Dual beam time of flight secondary ion mass spectroscopy (ToF SIMS) achieves the highest depth resolution due to the possibility of decoupling the sputtering gun from the analysis gun, thus employing relatively low energies for sputtering. In particular, by using Cs+ ions for

sputtering, a very high sensitivity can be obtained in negative polarity. The detection limits for numerous elements can be further improved by modifying the surface chemistry of the analyzed material. The negative ion yields can be enhanced by several orders of magnitude by depositing or implanting in the surface of interest highly electropositive elements such as alkali metals. The Cs ions beam has, therefore, become the most commonly used primary ion source for negative secondary ion detection [12].

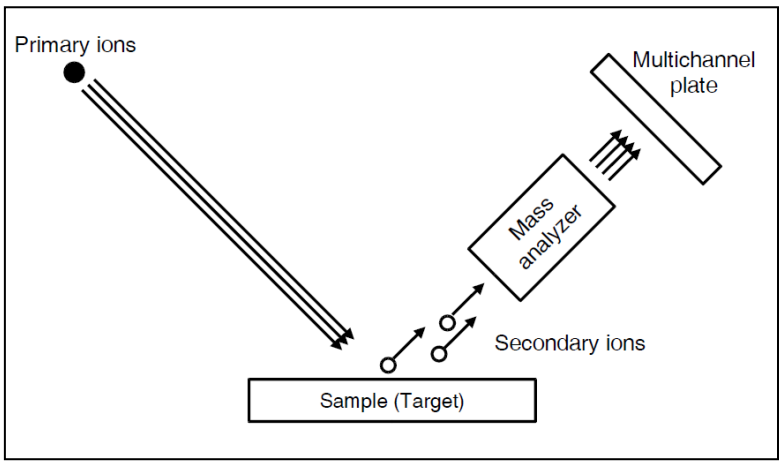

Figure 3.11 Schematic view of SIMS instrumentation.

3.5 Atomic Force Microscopy

Atomic force microscopy (AFM) operates by measuring the force between a probe and the sample. This force depends on the nature of the sample, the distance between the probe and the sample, the probe geometry and the sample surface contamination.

In contrast to scanning tunneling microscopy (STM), which requires electrically conducting samples, AFM is suitable for conducting as well as insulating samples [11].

AFM instrument consists of a cantilever with a sharp tip mounted on its end. The cantilever is usually formed from silicon, silicon oxide or silicon nitride and it is typically 100 µm long, 20 µm wide and 0.1 µm thick. The vertical sensitivity depends on the cantilever length. Figure 3.12 shows a schematic illustration of an AFM. When the tip is brought into proximity of a sample surface, forces between

the tip and the sample lead to a deflection of the cantilever according to Hooke's law. Depending on the situation, forces that are measured in AFM include mechanical contact force, van der Waals forces, capillary forces, chemical bonding, electrostatic forces, magnetic forces, Casimir forces. Typically, the deflection is measured using a laser spot reflected from the top surface of the cantilever into an array of photodiodes. Other methods that are used include optical interferometry, capacitive sensing or piezoresistive AFM cantilevers.

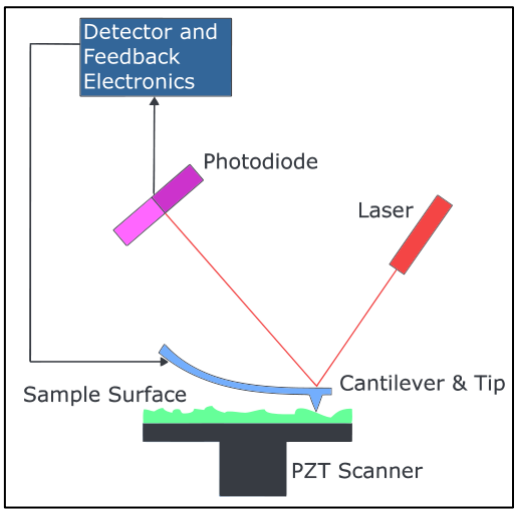

Figure 3.12 Block diagram of atomic force microscope.

AFM can operate in several modes. In the *contact mode*, the probe tip is dragged across the surface and the resulting image is a topographical map of the sample surface. A drawback for this mode of operation is that the dragging motion of the probe tip, combined with adhesive forces between the tip and the surface, can damage both sample and probe. In the *non-contact mode*, the instrument senses van der Waal attractive forces between the surface and the probe tip held above the sample surface. Nevertheless these forces are substantially weaker than the contact mode forces so that the tip must be given a small oscillation and ac detection methods are used to detect the small forces between the sample and the tip. *Tapping mode* imaging overcomes the limitations of the conventional scanning modes by alternately placing the tip in contact with the surface to provide high resolution and then lifting the tip off the surface to avoid dragging the tip across the surface. It is implemented in ambient air by oscillating the cantilever assembly at or near the cantilever's resonant frequency with a piezoelectric crystal. The piezo motion causes the cantilever to oscillate when the tip does not contact the surface. The

oscillating tip is then moved toward the surface until it begins to lightly touch the surface. During scanning the vertically oscillating tip alternatively contacts the surface and lifts off, generally at a frequency of 50 to 500 kHz. As the oscillating cantilever contacts the surface intermittently, energy loss caused by the tip contacting the surface reduces the oscillation amplitude that is then used to identify and measure surface features. When the tip passes over a bump in the surface, the cantilever has less room to oscillate and the amplitude of oscillation decreases. Conversely, when the tip passes over a depression, the cantilever has more room to oscillate and the amplitude of the tip is measured and the feedback loop adjusts the tip-sample separation maintaining constant amplitude and the force on the sample [11].

References

1. Zheng Cui, *Micro-Nanofabrication*, Springer (2005)

2. http://www.zeiss.com/nts

3. H. G. Tompkins, and E. A. Irene, *Handbook of Ellipsometry*, Springer New York (2005)

4. H. G. Tompkins and E. A. Irene, *"Handbook of Ellipsometry"*, W. Andrews Inc., New York (2005)

5. H. G. Tompkins, *A user's guide to Ellipsometry*, Dover Publications, Inc., Mineola, New York (1993)

6. J. N. Hilfiker, C. L. Bungay, R. A. Synowicki, T. E. Tiwald, C. M. Herzinger, B. Johs, G. K. Pribil, and J. A. Woollam, *J. Vac. Sci. Technol. A* **21**, 1103 (2003)

7. K. Vedam, *Thin Solid Films* **313**, 1 (1998)

8. http://www.jawoollam.com

9. User manual, *Easy to use acquisition/analysis software for spectroscopic ellipsometry (EASE™)*, Ver. 2.30, J. A. Woollam Inc.

10. H. Read, *Analytical (Trasmission) Electron Microscopy*, in Analysis of Microelectronics Materials and Devices, M. Grasserbauer and H. W. Werner, eds., Wiley & Sons Ltd, New York (1991)

11. D. K. Schroder, *Semiconductor Material and Devices Characterization*, Wiley & Sons, Inc., New York (2006)

12. M. L. Yu, *Phys. Rev. B* **26**, 4731 (1982)

Chapter 4

Results and discussion

4.1 Introduction

In this chapter the experimental results related to the fabrication of various nanostructured materials by block copolymer lithography are presented. In particular in section 4.2 DBCs composed of polystyrene (PS) and poly(methylmethacrylate) (PMMA) are employed to fabricate periodic nanoporous thin films to be used as soft mask in advanced lithographic processes. The selected PS-*b*-PMMA system is suitable for this protocol because PMMA can be easily degraded by ultraviolet exposure and subsequently removed by acetic acid treatment. Following this approach it is possible to fabricate a nanoporous PS mask with controlled characteristic dimensions to be used for the synthesis of nano-objects, such as nanodots and nanowires, as well as for advanced lithographic processes. In particular a detailed analysis of the experimental parameters that determine the final characteristics of the nanoporous polymeric mask, such as the thickness of the polymeric film, the pore diameter and the pore-to-pore distance, is presented. In section 4.3 the PS polymeric soft mask is used as a sacrificial layer to transfer the nanoporous pattern to the underlying SiO_2 film. The resulting nanoporous SiO_2 film can be used as hard mask for subsequent lithographic processes or as a backbone for the conformal growth of other material in order to fabricate nanostructured surfaces with tunable characteristic dimensions. In section 4.4 atomic layer deposition (ALD) is used to grow a thin Al_2O_3 film on to the nanoporous SiO_2 scaffold. By properly tuning the thickness of the conformal Al_2O_3 layer, the characteristic dimensions (pore diameter and depth) of the resulting nanoporous Al_2O_3 are controlled at nanometer level, providing a versatile approach to the synthesis of nanostructured surfaces. In the following two sections the nanoporous PS mask is used to fabricate ordered arrays of Si nanocrystals by means of ion beam synthesis and lift off processes both in the plane and in non-periodic

nanostructures fabricated by e-beam lithography. Finally in the last section of the chapter we explore the possibility to control the in plane positioning of the nanoporous template by depositing the BC thin film on pre-patterned surfaces.

4.2 Soft mask fabrication

Successful deposition of block copolymer thin films requires an accurate preparation and cleaning of the substrate. Small silicon pieces, whose dimensions can vary from 1 x 1 cm^2 up to 3 x 3 cm^2, were used. Mainly the silicon pieces were cut from 200 mm diameter Si (100) wafers with a 16 nm thick SiO_2 film thermally grown on top of it and from 100 mm diameter Si (100) wafers with a 50 nm thick SiO_2 film thermally grown on top of it. Piranha solution (H_2SO_4/H_2O_2 in the ratio 3:1) cleaning at 80°C for a time that can vary from 40 to 60 minutes was performed to eliminate any residual organic trace and to vary the hydroxyl group (-OH) density at SiO_2 surface. A higher concentration of hydroxyl group means a higher concentration of anchoring point for the random copolymer terminations, as described in chapter 2. After the piranha cleaning the samples were rinsed in water, cleaned with isopropanol in an ultrasonic bath and dried under N_2 flow.

After cleaning the SiO_2 surfaces were properly neutralized in order to avoid preferential wetting of one of the two components. From a general point of view, when block copolymers are confined in thin films several constraints have to be considered. The most influencing parameters concern the interaction of the block copolymers at the interfaces, both the polymer-air interface and the polymer-substrate interface. All the processes performed during this activity were carried out in vacuum atmosphere (~10^{-3} mbar). Focusing on the interaction between the block copolymer and the substrate, the general rule of parallel orientation of the microdomains respect to the substrate, due to the preferential wetting of one of the two blocks with the substrate, has to be considered. Different strategies have been proposed in the literature to achieve perpendicular orientation of the microdomains, such as surface modification, strong electric field and solvent annealing [1, 2, 3, 4, 5]. In the present work we neutralized the surface by means of random copolymer of suitable composition. In particular different PS-*r*-PMMA random copolymers were used to avoid the PMMA preferential wetting of the substrate. Two random

copolymers (PS-*r*-PMMA) with a styrene fraction of 0.58, M_n = 11400 and PDI = 1.64 and a styrene fraction of 0.62, M_n = 13500 and PDI = 1.26 respectively were purchased from Polymer Source Inc. and used without further purification. Hereafter these random copolymers will be identified by the labels R58 and R62 respectively, the number indicating the PS fraction of the PS-*r*-PMMA. The PS fraction of PS-*r*-PMMA determines the window of thickness in which perpendicular orientation of the domains occurs [6, 7, 8, 9, 10]. Thus the choice of the random copolymer has to be evaluated depending on the desired applications. The protocol developed to generate the neutralization layer by means of PS-*r*-PMMA, is the same for both the R58 and R62 and it is depicted in figure 4.1. A solution with 9 mg of PS-*r*-PMMA in 1 ml of toluene was prepared and rinsed in ultrasonic bath. The OH terminations of the random copolymer were used to graft the copolymer to the silicon oxide layer. The solution was spun for 30 seconds at 3000 rpm. The samples were annealed in vacuum with a pressure value of 3 x 10^{-2} mbar at 170° C for 48 hours. The temperature was well above the glass transition temperature of the copolymers to allow chain ends to diffuse and react with the substrate. After annealing, samples were cleaned by rinsing for 5 minutes in toluene sonication to remove non-anchored chains: the thickness of the resulting self assembled layers, measured by spectroscopic ellipsometry, were 4.5 ± 0.4 nm for the R58 and 8.1 ± 0.3 nm for the R62 respectively.

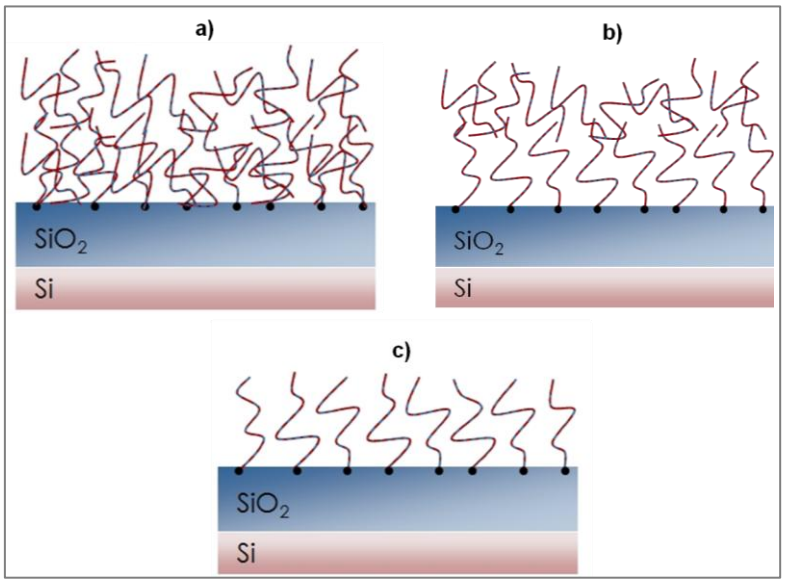

Figure 4.1 PS-*r*-PMMA chains deposited by spin coating on SiO_2 substrate (a), self alignment of the first layer of random copolymer (b) and self-assembled PS-*r*-PMMA chains after removal of the unbounded chain by sonication in toluene (c).

The asymmetric PS-*b*-PMMA copolymer with a styrene fraction of 0.71, M_n = 67100 and PDI = 1.09 was purchased from Polymer Source Inc. and used without further purification. This type of block copolymer naturally self separates in hexagonally packed PMMA cylinders embedded in a PS matrix. A solution with PS-*b*-PMMA copolymer in toluene was prepared. The spinning parameters of the solution were properly adjusted to obtain the desired film thickness. The annealing was performed under vacuum ($p = 3 \times 10^{-2}$ mbar) at 190° C for 2 hours to promote self-organization into hexagonal arrangements of PMMA cylinders in a PS matrix with natural domain period $L_0 \sim 36$ nm [11]. As in the case of PS-*r*-PMMA the block copolymers were heated well above their glass transition temperature, corresponding to 102°C for PS block and 111°C for PMMA block respectively [12].

4.2.1 The role of random copolymer

Substrate neutralization with PS-*r*-PMMA random copolymer is essential in order to get the perpendicular orientation, with respect to the substrate, of the PMMA cylinder in the polymeric thin film. Depending on the grafting copolymer used for the neutralization of the substrate, the desired orientation can be achieved in different windows of thicknesses of the polymeric films [6]. In figure 4.2 SEM plan views of the PS-*b*-PMMA films with different thicknesses are reported for both random copolymers. According to SEM images, the R58 random copolymer presented a narrow window with perpendicular orientation at 21 ± 0.5 nm, i.e. well below the lattice spacing L_0 of the PS-*b*-PMMA copolymer. In a recent paper Zucchi *et al.* analyzed the effect of thickness commensurability on the same system and showed the presence of a well defined window of thicknesses centered around 18 nm and slightly shifted compared to our present results [11]. This discrepancy is attributed to the different pressure conditions during the thermal treatment. Due to the limited thermo-oxidative stability of thin polymeric films, variations of the annealing pressure, i.e. of the residual oxygen partial pressure in the furnace, are reported to modify the random layer composition and consequently the neutralization of the surface, affecting the final arrangement of the block-copolymer thin film [11]. On the contrary the R62 random copolymer presented a wide

window of thicknesses, ranging from 21 nm to 38 nm, with perpendicular orientation of PMMA cylinders, in excellent agreement with data reported by Ham *et al.* [13].

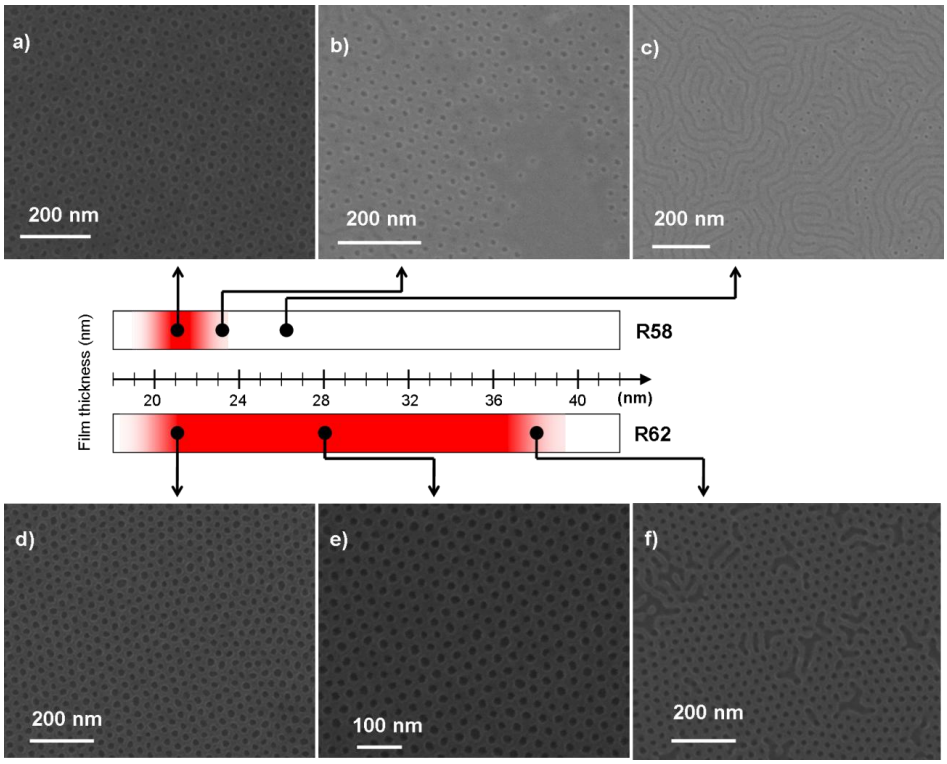

Figure 4.2 SEM images of PS-*b*-PMMA films self-assembled on R58 random copolymer as a function of film thickness: (a) 21 nm, (b) 23 nm, (c) 26 nm. SEM images of PS-*b*-PMMA films self-assembled on R62 random copolymer as a function of film thickness: (d) 21 nm, (e) 28 nm, (f) 38 nm.

From the technological point of view, the presence of a very narrow window, as obtained for the R58 random copolymer, implies severe limitations. Uniform polymeric thin films can be easily achieved only on 1 x 1 cm^2 areas: when operating on samples larger than 1x1 cm^2, small fluctuations of the thickness of the polymeric film, due to spinning conditions, determine instabilities of the film morphology, as depicted in figure 4.3(a). Moreover the thickness of the polymeric mask cannot be tuned as function of the lithographic process requirements. The large window of thicknesses obtained for the R62 random copolymer allows overcoming all these limitations. Figure 4.3(b) shows the perfect perpendicular orientation of the block copolymer obtained over the entire area of the sample, when neutralizing the surface with the R62 random copolymer.

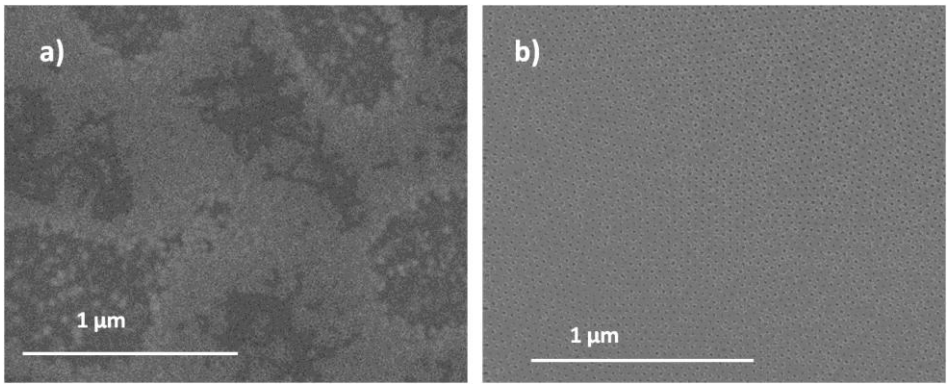

Figure 4.3 SEM images of block copolymer thin films spun on a 2x2 cm^2 surface neutralized with R58 random copolymer (a) and on a 3x3 cm^2 substrate neutralized with R62 random copolymer (b).

In order to fabricate the nanoporous PS mask, selective removal of the cylindrical PMMA blocks is required. It is well known that ultraviolet exposure (5 mW/cm^2, λ=253.7 nm, 90 min) degrades the PMMA and cross links the PS matrix. After UV treatment the PMMA cylinders are selectively removed by immersion in acetic acid bath and subsequent rinsing in deionized water. Finally oxygen plasma treatments are performed to remove the random copolymer at the bottom of the pores. Repeated cycles of UV exposure and acetic acid followed by oxygen plasma treatments were optimized in order to assure the complete opening of the pores in the matrix. In particular, for R58 removal, repeated cycles of UV degradation, rinsing in acetic bath and oxygen plasma treatment are used according to the following sequence:

- UV irradiation for 90 minutes and subsequent acetic acid bath for 8 minutes
- Oxygen plasma at 40 W, with partial pressure of 0.6 mbar, for 30 seconds
- UV irradiation for 90 minutes and subsequent acetic acid bath for 8 minutes
- Oxygen plasma at 40 W, with partial pressure of 0.6 mbar, for 30 seconds
- UV irradiation for 90 minutes and subsequent acetic acid bath for 8 minutes

When R62 is used the sequence of the step is the same with the difference that the oxygen plasma in each step is 1 minute long. The duration of the oxygen plasma exposure is strictly related to the thickness of the random copolymer: thicker the random polymer thin film, longer the required oxygen plasma treatment. In figure 4.4(a) the etching calibration performed on the random copolymer is shown. Considering that the R58 random copolymer is 4.5 ± 0.4 nm thick and the R62 random copolymer is 8.1 ± 0.3 nm thick, the overall time of oxygen plasma is expected to be 60 seconds in the former case and 120 seconds in the latter case. To

verify this issue, Si dots were fabricated by e-beam evaporation of silicon through the nanoporous polymeric template and subsequent removal of the PS matrix by degradation in piranha solution. SEM images in figure 4.4 depict the difference between a mask with partially (b) and well (c) opened pores.

It is worth to note that piranha solution is a very aggressive treatment. Even if the most indicated procedure for lift-off implies the use of an organic solvent, the removal of the PS mask was performed by means of piranha solution because of the hard cross linking of the PS matrix after the oxygen plasma treatment. In fact several experiments were performed to understand the behavior of the PS mask during the removal of PMMA cylinders: in particular a step-by-step dissolution of the PS mask was performed, i.e. a sonication in toluene was performed after each step of the protocol developed for the removal of PMMA cylinders in order to identify the step of process that determines the cross-linking of the polymeric matrix. We observed that the polymeric mask was no more soluble in toluene after the oxygen plasma treatment. This is probably due to some specific spectral lines in the UV range of the oxygen plasma spectrum [14]. In order to avoid this effect different configurations of the plasma were considered, working with Argon, Oxygen and a mixing of Ar/O at several pressures (from 0.6 up to 2 mbar). No one of these combinations was demonstrated to be effective in limiting the cross-linking of the PS matrix.

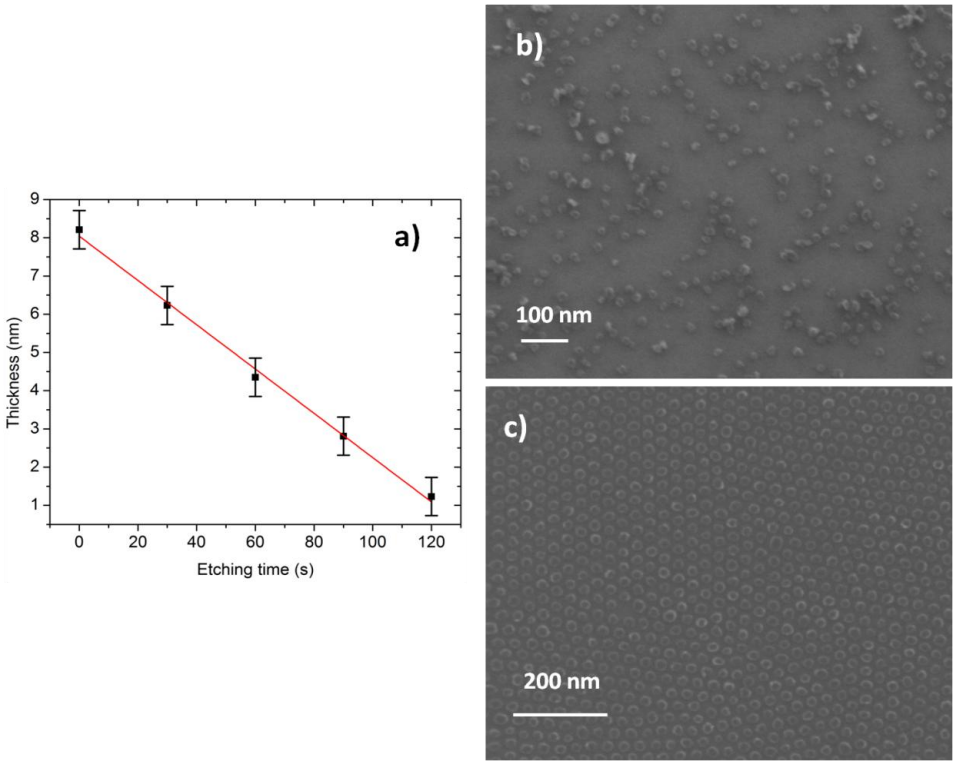

Figure 4.4 Calibration curve of oxygen plasma etching for the R62 random copolymer. The thickness of the random copolymer film is plotted as a function of the etching time (a). SEM images of the silicon dots evaporated through the nanoporous mask after removal of the PS thin film. Disordered or ordered arrays of Si dots are observed when the evaporation is performed through a mask with partially (b) or well (c) opened pores.

In conclusion the oxygen plasma treatment is essential to remove the random copolymer from the bottom of the pores, but it induces a hard cross linking of the PS mask making it completely insoluble in conventional organic solvents, despite different works in the literature claiming that the PS mask can be removed by dipping the samples in toluene or other solvents [15, 16, 17]. Piranha solution was found to be the only chemical agent really effective to burn the PS matrix after the plasma treatment.

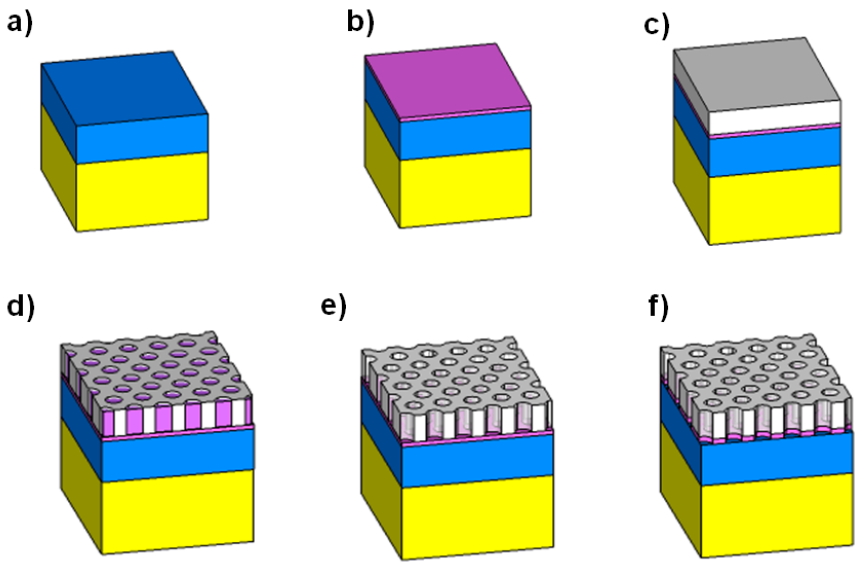

Figure 4.5 Protocol for the fabrication of PS soft mask: surface preparation (a), spin coating of PS-*r*-PMMA and annealing (b), spin coating of PS-*b*-PMMA (c), annealing at 190°C to induce self-organization of the blocks (d), removal of PMMA cylinders by UV irradiation and acetic acid bath (e) and removal of the random copolymer at the bottom of the pore by means of oxygen plasma (f).

The complete process for the fabrication of the nanoporous PS mask is schematically depicted in figure 4.5. Figure 4.6 shows a SEM plan view image of the final nanoporus PS template which exhibit the tipical hexagonally distribution of the pores in the polymeric soft mask resembling the PMMA cylinder orientation after the self-assembly process.

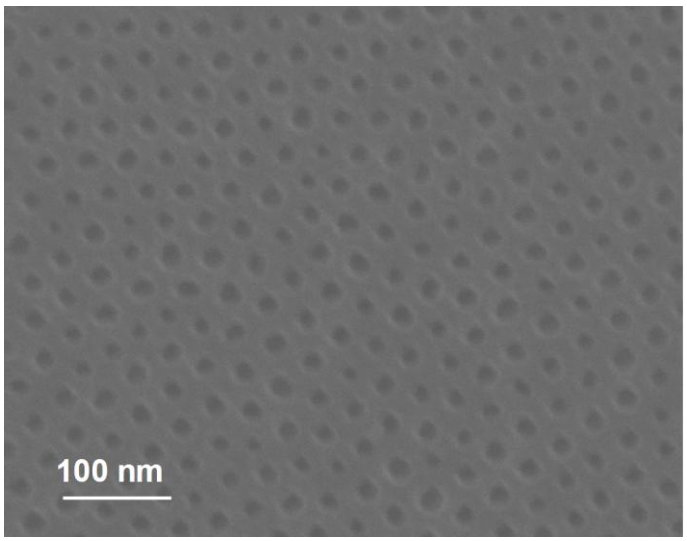

Figure 4.6 Plan view SEM images of polymeric PS mask after the complete removal of PMMA cylinders and complete aperture of the pore.

4.2.1.1 Statistical analysis

The oxygen plasma treatment is expected to have an impact on the morphology of the PS matrix, since the exposure to oxygen plasma is supposed to isotropically degrade the polymeric film. For this reason the evolution of the average diameter of the pores during the various steps of the process was monitored. A detailed analysis of the pore diameter was performed by means of SPIP^{TM} software, the scanning probe image processor. This software allows the analysis of SEM or AFM images, determining a variety of structural properties of a film surface. A detailed analysis of pore and particles is also possible with this kind of software. In particular we used the software to calculate the mean pore diameter of the polymeric mask, as well as the centre-to-centre distance between pores. In the "Threshold Detection Method", depending on the quality of the SEM image, the software makes difference between the contrast values in the image: below a certain value the particle/pore is not selected while above a certain value the pores are selected and a further differentiation occurs, depending on their diameter. In this way a distribution of the diameters can be obtained, together with other useful information. Figure 4.7 shows an example of the detection method: a rectangular region of the SEM image plan view image of the nanoporous PS template has been selected (in principle any kind of shape can be selected) and a measure of the parameters of the pores has been performed. Each color which encircles the pores indicated a pore with a different area. It is possible to represent these data in a histogram that indicate the number of pores with similar areas. Assuming the pores have a circular shape, from the area it is then possible to calculate the diameter of the pores. Moreover form the analysis of the picture it is possible to determine the pore-to-pore average distance.

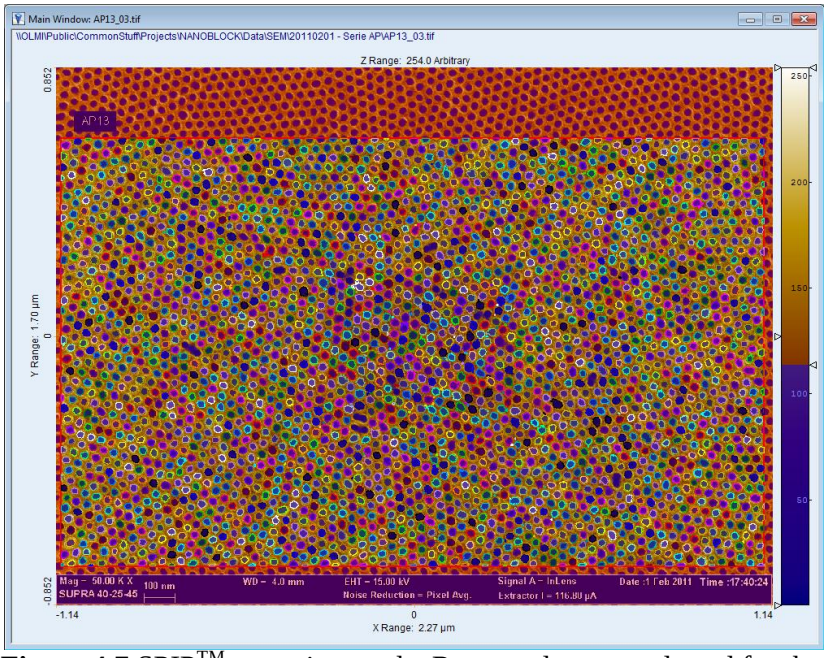

Figure 4.7 SPIP^{TM} operating mode. Rectangular area selected for the analysis of the pores. Each color represents a different pore measure.

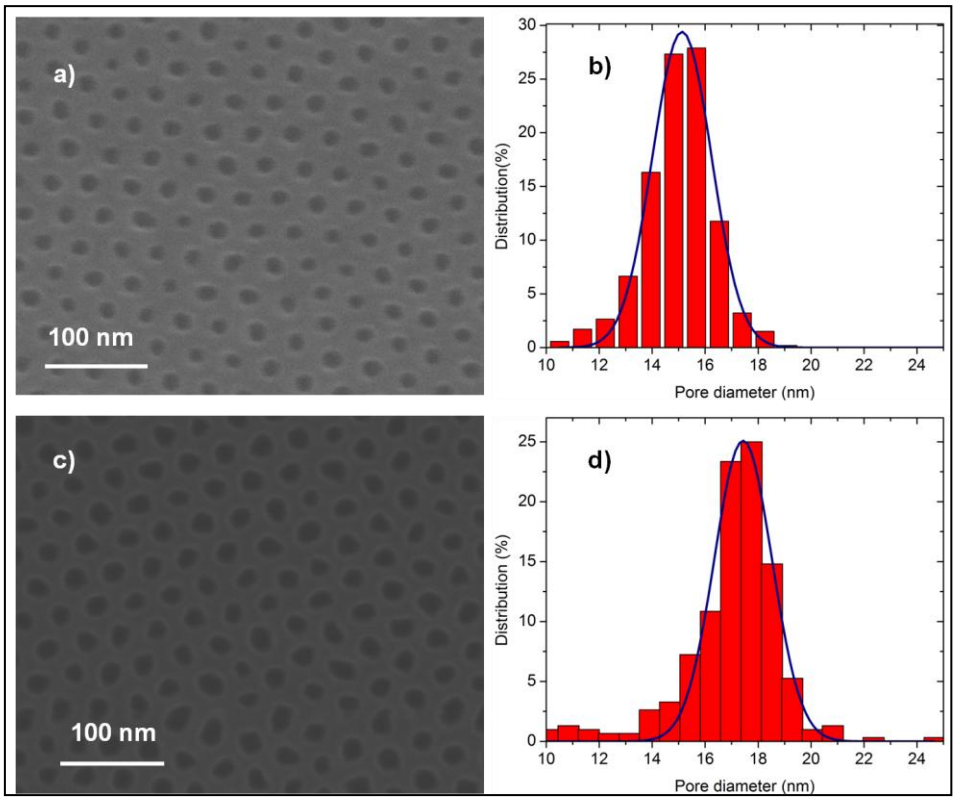

Figure 4.8 SEM image of the PS mask after 30 seconds of oxygen plasma (a) and relative Gaussian curve indicating the pore distribution (b). SEM image of the PS mask after 60 seconds of oxygen plasma (c) and relative Gaussian curve (d). The PS fraction in random copolymer is 0.58 (R58).

Figure 4.8(a) shows the SEM image of the PS mask after the first cycle of UV and acetic acid followed by 30 seconds oxygen plasma treatment for the R58 random

copolymer. The SEM image of the same polymeric film after complete removal of the PMMA cylinders, i.e. after a second cycle of UV irradiation and acetic acid followed by a further 30 seconds oxygen plasma treatment and then a last cycle of UV irradiation and acetic acid, is reported in figure 4.8(c). Software analysis of the SEM images allowed determining the size and spatial distribution of the pores in the PS matrix. Figure 4.8(b) and 4.8(d) show the size distributions of the pore diameter as obtained from the images reported in figure 4.8(a) and 4.8(c) respectively. The comparison between the histograms in figure 4.8(b) and 4.8(d) highlights an enlargement of the average pore diameter during the process for the removal of the PMMA cylinders. In both cases the shape of the distribution is Gaussian-like. The analysis was repeated for several SEM images on a set of samples prepared using the same recipe and the weighted mean of the pore diameter was calculated. Following this procedure a mean pore diameter <d> of 15.3 ± 0.3 nm after the 30 seconds oxygen plasma treatment and a mean pore diameter of 17.3 ± 0.4 nm after complete removal of the PMMA cylinders were determined. The center-to-center distance D between the nearest pores was not modified during the PMMA removal process. D values were measured by software analysis of the SEM images obtained from various samples and the mean value <D> is 33.1 ± 0.3 nm.

The same analysis was performed on the samples prepared using R62 random copolymer for surface neutralization. Figure 4.9(a) shows the SEM image of the PS mask after the first cycle of UV and acetic acid followed by 30 seconds oxygen plasma treatment. The SEM image of the same polymeric film after a second cycle of UV irradiation and acetic acid followed by a further 30 s oxygen plasma treatment is reported in figure 4.9(c). In both cases the shape of the size distribution of the pores in the PS matrix is Gaussian-like as shown in figure 4.9(b) and 4.9(d). The mean pore diameter <d> was determined to be 16.7 ± 0.4 nm after the first opening cycle and 19.0 ± 0.5 nm after the second one. The average distance <D> between the nearest pores was not modified during the process and a mean value of 33.1 ± 0.2 nm was measured. As previously discussed, due to the thickness of the R62 random copolymer thin film, a further oxygen plasma treatment (60 seconds) is required in order to completely open the bottom of the pores. Figure 4.9(e) shows the matrix after this last cycle and the corresponding size distribution of the pores is shown in figure 4.9(f). The mean pore diameter <d> after the complete opening of

the pores was determined to be 20.7 ± 0.6 nm, while no variations of the center-to-center distance <D> between the nearest pores was observed.

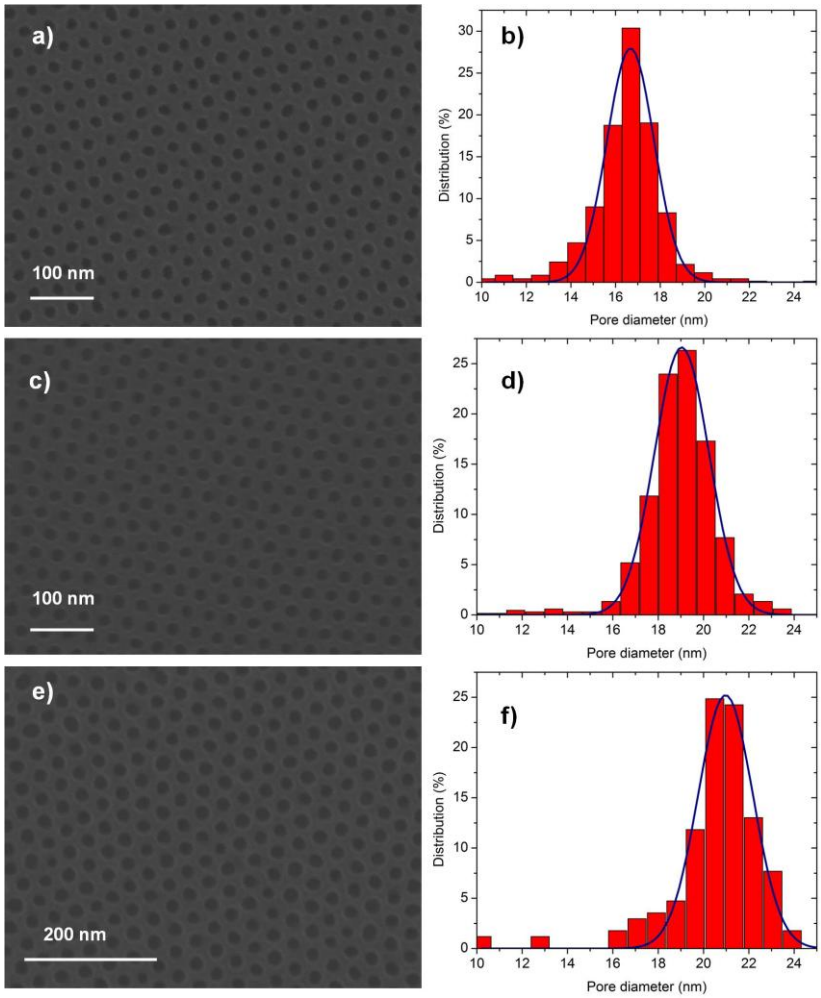

Figure 4.9 SEM image of the PS mask after 30 seconds of oxygen plasma (a) and relative Gaussian curve indicating the pore distribution (b). SEM image of the PS mask after 60 seconds of oxygen plasma (c) and relative Gaussian curve (d). SEM image of the PS mask after 120 seconds of oxygen plasma (e) and relative Gaussian curve (f). The PS fraction in random copolymer is 0.62 (R62).

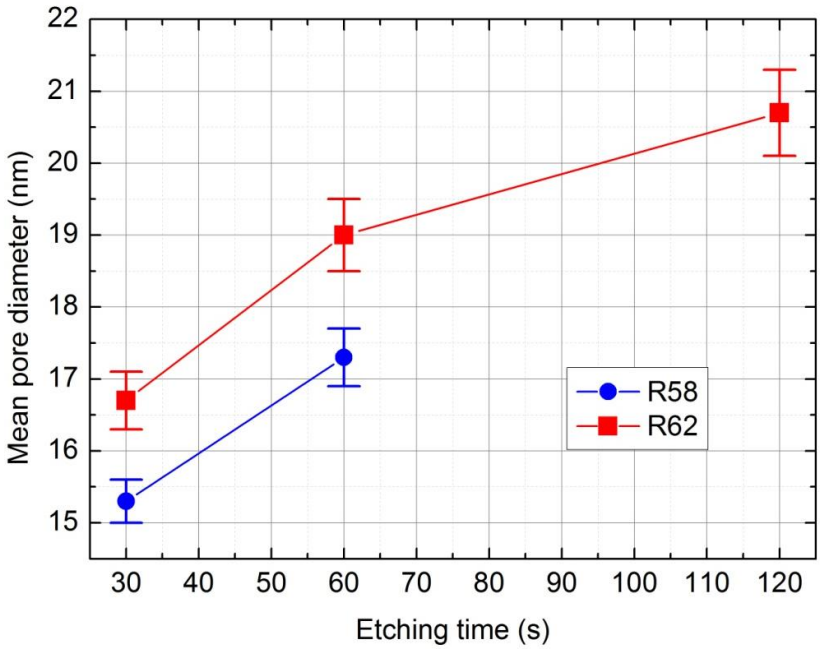

Figure 4.10 The mean pore diameters of the PS masks deposited on different random copolymers are reported as a function of the oxygen plasma etching time.

To summarize the evolution of the mean pore diameter in the polymeric films as a function of the oxygen plasma irradiation time, the <d> values obtained for the two PS-*r*-PMMA copolymers are reported in figure 4.10. According to these experimental findings, considering equivalent oxygen plasma exposures, the average dimension of the pores in the PS matrix is larger in the films deposited on the R62 random copolymer than in those deposited on the R58 random copolymer. The reported evolution of the pore diameter with the exposure to oxygen plasma could be explained in terms of isotropic etching of the polymeric mask. Moreover the strong cross-linking of the PS matrix, induced by the oxygen plasma treatment, could result in volume contraction of the polymeric film and consequently in the observed enlargement of the pores without any variation of their center-to-center distance [18]. On the other side the observed variation in pore diameter, when depositing the PS-*b*-PMMA block copolymer on different random copolymer thin films, suggests that the neutralization of the substrate influences the orientation of the PMMA cylinders with respect to the substrate, as well as their characteristic dimensions. This is a new interesting result in the expertise area of block copolymers. According to a phenomenological description of the system, the perpendicular or parallel orientation for each specific polymeric system is

determined by the free energy F of the block copolymer thin film, which can be expressed as:

$$F = F_{elastic} + F_{S\text{-}MMA} + F_{surface} + F_{interface} \quad (4.1)$$

where $F_{elastic}$ indicates the elastic free energy of the stretched block chains, including the entropic phenomena governing the chains conformations, $F_{S\text{-}MMA}$ refers to the energy of interaction between PS and PMMA blocks of the copolymer, $F_{surface}$ is the surface energy at the free surface and $F_{interface}$ refers to the surface energy of the interaction of the block copolymer with the functionalized substrate [19, 20]. Within the window of thicknesses with perpendicular orientation, the variation of the pore diameter, induced by the substrate neutralization, should be described taking into account all the different contributions to the overall free-energy of the system. Considering that in both cases the same block copolymer was used, the $F_{S\text{-}MMA}$ contribution is exactly the same irrespective of the random copolymer. Similarly $F_{surface}$ could be assumed to be equivalent in both cases, since the processing conditions were the same in terms of atmosphere and pressure during the thermal treatments. According to this model, a variation of the $F_{interface}$ contribution, due to the different substrate neutralization, results in a new equilibrium condition to be achieved by adjusting the $F_{elastic}$ term. Considering the experimental data herein reported, the center-to-center distance of the pores in the PS matrix is the same for both type of random copolymers but the mean pore diameter is different in the two cases. This finding supports the idea of a different stretching of the PS chains in the polymeric matrix, resulting in a variation of the pore dimension, in agreement with the phenomenological model.

From a technological point of view, these results demonstrate that the choice of the random copolymer is crucial for the implementation of a disposable polymeric mask with well controlled dimension. Both the random copolymers under consideration present a window of thicknesses below L_0 that could be very useful for the fabrication of ultrathin soft mask in advanced lithographic processes. In particular the R62 random copolymer has the advantage of a large window of thicknesses in which perpendicular orientation of the PMMA cylinders occurs. This fact allows tuning the optimum thickness of the mask, depending on the requirements of the specific lithographic process to be implemented. On the other

hand, the average pore diameter in the polymeric films deposited on the R58 random copolymer is intrinsically smaller than in the films deposited on the R62 random copolymer. Moreover the thickness of the R58 random copolymer is below 5 nm; the opening of the pores requires no more than 60 seconds of plasma treatment and, consequently, the final dimension of the opened pores in the PS matrix is below 18 nm. On the contrary the thickness of the R62 random copolymer is around 8 nm and complete opening of the pores requires at least 120 s of O_2 plasma exposure. As previously demonstrated, long plasma treatments induce a progressive enlargement of the pores in the PS matrix. Although this enlargement does not substantially modify the functionality of the disposable polymeric mask, careful evaluation of the random copolymer choice is required in order to match the specific lithographic constraints. Various aspects have to be considered to achieve the desired results. In particular, according to the present data, in order to simultaneously maximize the window of thicknesses with perpendicular orientation of the PMMA cylinder and minimize the pore diameter of the final PS mask, a random copolymer with the same PS fraction of the R62 copolymer and a lower molecular weight (i.e. a lower chain length) would represent the best compromise; the lower the molecular weight, the lower the thickness of the random copolymer film. The overall result would be a reduction of O_2 plasma exposure and, consequently, a minimization of the pore enlargement due to the isotropic etching.

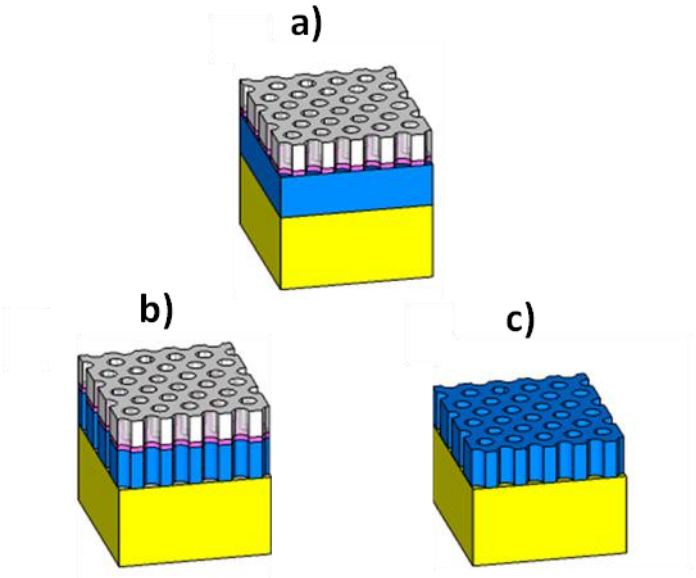

Figure 4.11 Fundamental steps to fabricate nanoporous SiO_2 oxide: PS matrix after complete opening of the pores by means of oxygen plasma (a), RIE through PS matrix on SiO_2 substrate (b) and nanoporous SiO_2 after the removal of PS matrix (c).

4.3 Hard mask fabrication

Etching process is one of the approaches used in the thesis work to create nano-objects. In this case the soft PS mask acts as a sacrificial layer to pattern the underlying substrate and to create a hard nanoporous SiO_2 masks. Figure 4.11 depicts the steps to generate a nanoporous SiO_2 matrix starting from the BC mask. For this experiment the R58 random copolymer was used and reactive ion etching (RIE) was performed, through the BC mask, on the SiO_2 substrate in order to faithfully transfer the pattern and fabricate the nanoporous oxide structure. The polymeric mask was finally removed by wet etching, i.e. by piranha solution. The dry etching process was performed in a Plasmalab 80 Plus at a pressure of 40 mTorr. The power of RF Generator was set at 120 W and the Bias Voltage at 340 V. The gas was a mixture of CHF_3 (60 sccm) and Ar (25 sccm). The etching was carefully calibrated and a linear dependence of the etched thickness as a function of time was observed, as shown in figure 4.12.

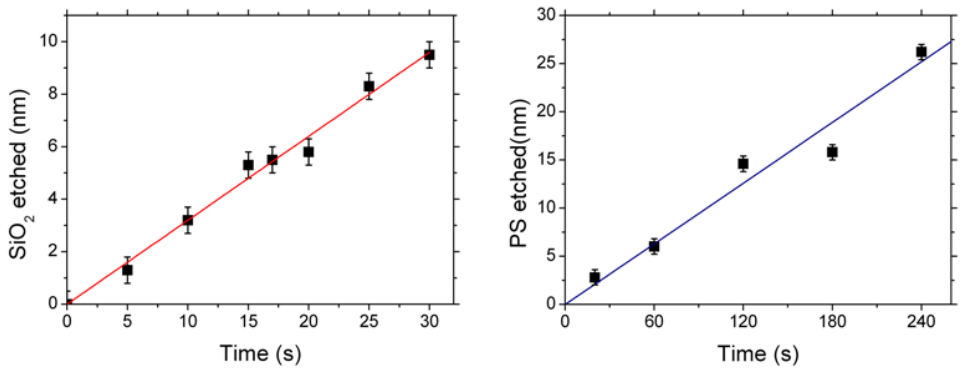

Figure 4.12 Thickness of the portion of SiO_2 (left) and PS (right) removed during the RIE treatment as a function of time.

Once again the complete opening of the pores is a fundamental pre-requisite in order to ensure the reproducibility and uniformity of the dry etching process through the polymeric mask on the underlying SiO_2 layer. Figure 4.13 shows SEM plan view images of the nanostructured SiO_2 film when the RIE processing is performed through a polymeric film with partially (a) or well opened (b) pores. The images were acquired after removal of the nanoporous PS matrix by degradation in piranha solution. In the case of partial opening of the pores, i.e. without O_2 plasma treatment, the pattern of the nanoporous PS template was not faithfully transferred to the underlying SiO_2 film. On the contrary in the case of complete opening of the

pore, the SiO_2 matrix presents well defined haxagonally packed pores with dimension, density and lateral distribution that closely resemble the original nanoporous PS soft mask.

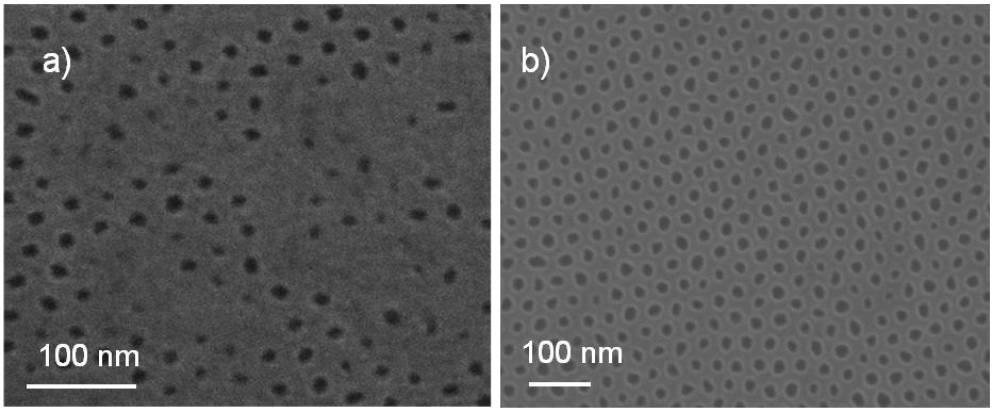

Figure 4.13 SEM images of SiO_2 film after 1 minute RIE (a) and after 1 minute oxygen plasma and subsequent 1 minute RIE (b).

The thickness of the original polymeric film for this experiment was 26 ± 1 nm as a result of the superimposition of the block copolymer and random copolymer layers. The O_2 plasma treatment determines a reduction of the thickness of the nanoporous PS template, reducing the overall thickness of the polymeric film. Assuming that the PS erosion rate during O_2 plasma exposure is roughly equivalent to the etching rate of the PS-*r*-PMMA copolymer a final thickness of the polymeric mask of 21 ± 1 nm was expected. This estimate is corroborated by ellipsometric analysis of the resulting polymeric film. Accurate calibration of RIE processing with CHF_3/Ar indicates that, in the optimized experimental conditions, the etching rate of SiO_2 and PS are 0.32 ± 0.04 nm/s and 0.10 ± 0.02 nm/s respectively, with an etch selectivity of 3. Consequently, considering the progressive erosion of the PS mask, the maximum achievable depth of the pores in the patterned SiO_2 is expected to be around 60 nm corresponding to an etching time of 200 s.

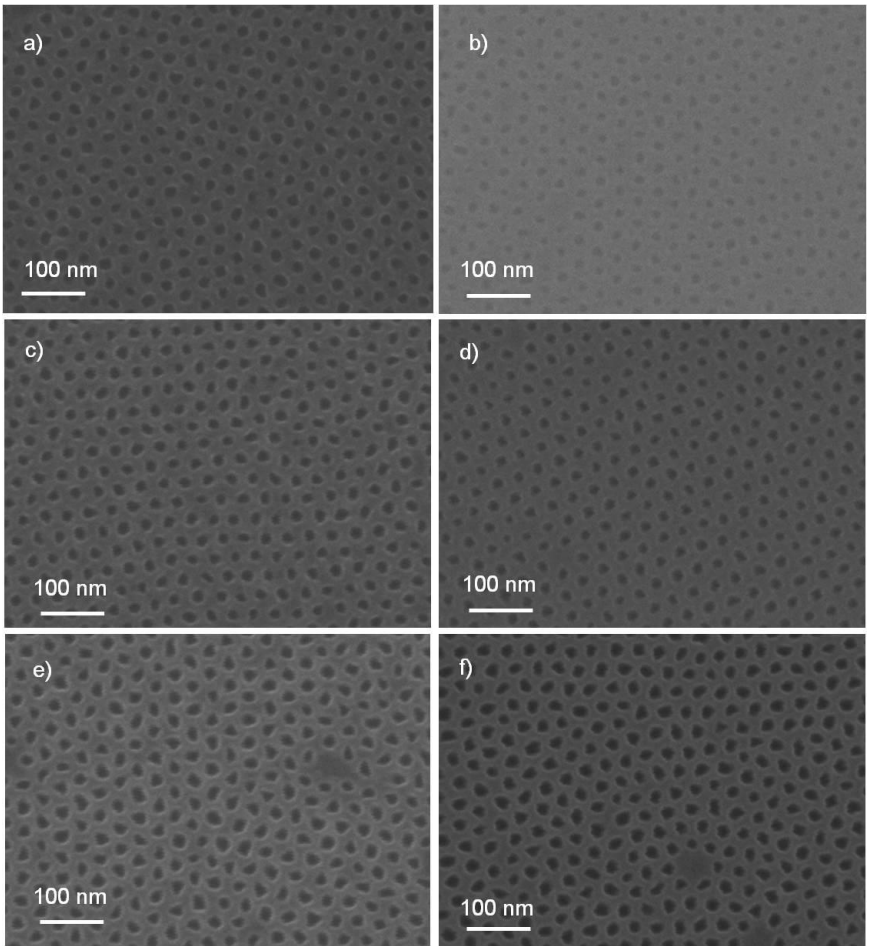

Figure 4.14 SEM images of PS matrix after 20 s RIE (a), 60 s RIE (c) and 100 s RIE (e). SEM images of SiO_2 substrate after the removal of PS matrix for 20 s RIE (b), 60 s RIE (d) and 100 s RIE (f).

The optimization of the RIE processing parameters through the nanoporous PS mask was performed using a 50 nm thick SiO_2 film grown on a Si (100) substrate. The etching time was varied from 20 s to 250 s. In figure 4.14 the representative SEM plan view images of the PS matrix after 20 s (a), 60 s (c), and 100 s (e) long exposure to CHF_3/Ar mixture are reported. A progressive enlargement of the pore diameter is observed with a slight modification of the shape of the pores. Similarly the SEM images of the same samples after removal of the PS template are reported as a function of the etching time in figure 4.14 (b), (d), and (f) respectively. The evolution of the shape and diameter of the nanopores in the SiO_2 clearly reproduce the modification of the polymeric template. By software analysis (SPIP^{TM}) of these images the mean pore diameter of the PS matrix, before and after RIE processing as well as the mean pore diameter of the pores in the SiO_2 matrix after removal of the polymeric mask by piranha degradation, was measured. The results of this analysis are reported in figure 4.15.

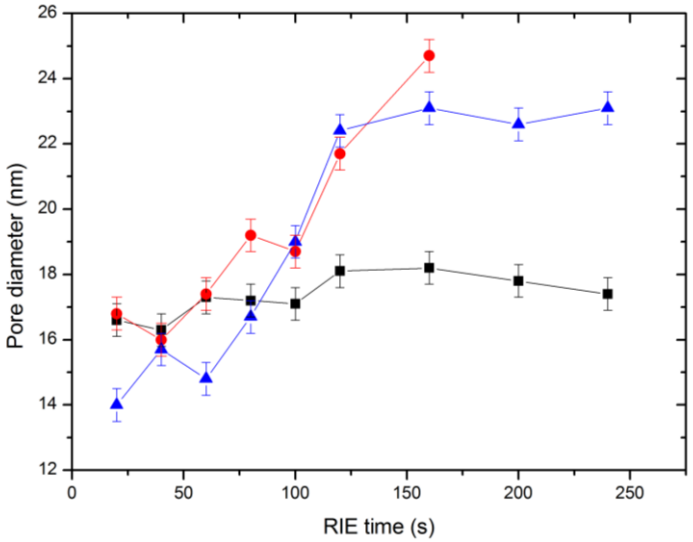

Figure 4.15 Mean pore diameter as a function of RIE time of PS initial mask (black data), of PS matrix after RIE process (red data) and of SiO_2 substrate after PS removal (blue data).

The diameter of the pores in the polymeric matrix after complete removal of the PMMA cylinders is fairly constant and oscillates around the average value 17.3 ± 0.4 nm. During RIE processing, a progressive enlargement of the pore diameter that corresponds to a gradual degradation of the polymeric template was observed. The measurement of the pore diameter in the SiO_2 matrix after the removal of the residual PS mask indicates that, during the initial stages of the RIE process the pores of the SiO_2 substrate are narrower than the corresponding pores in the PS mask. The diameter of the pores increases gradually with the RIE etching time (t) since for t ≥120 a steady state condition is reached with an average diameter of the pores equal to 23.0 ± 0.1 nm. The initial evolution of the nanopores in the SiO_2 matrix is consistent with the hypothesis of a conical shape of the pores in agreement with experimental data reported in literature [21]. Moreover cross sectional TEM analysis on the nanoporous SiO_2 with nominal thickness of 16 nm indicated a truncated conical shape, as shown in figure 4.6. It is worth to note that for t >160 s the PS mask is expected to be completely removed, yet no further evolution of the pore diameter is observed, supporting the idea of a good anisotropy of the etching process.

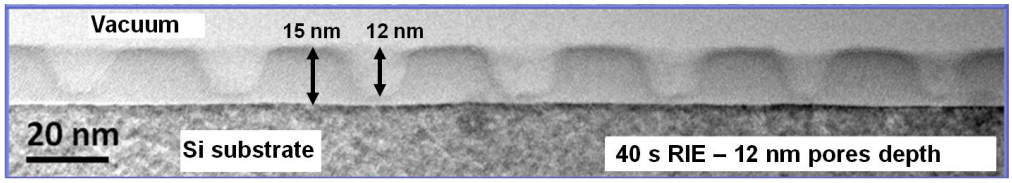

Figure 4.16 Cross sectional TEM image on nanoporous SiO_2 with a thickness of 15 nm, after 40 s of RIE.

Considering the etching rate of SiO_2, calculated by calibration reported above, 12 nm pore depth was expected after the RIE process and TEM analysis confirm the experimental calibration data. Such results demonstrate nanometric control of the dimensions of the nanoporous SiO_2.

4.4 Nanostructured surfaces

Nanoporous surfaces with controllable characteristic dimensions have received great attention due to their possible applications in various fields [22, 23, 24, 25]. The SiO_2 patterning described in section 4.3 offers a valid method to fabricate structures below 30 nm. A possible disadvantage of this type of structures is that the lowest achievable pore dimension of the nanoporous SiO_2 hard mask is determined by the physical size of the nanodomains in the block copolymer film, introducing a severe limitation to the versatility of this lithographic approach. In particular polymeric features with dimension below 10 nm are difficult to control, since a minimum number of monomers is necessary to overcome the critical value of the energy of interaction between the two homopolymers and, consequently, to induce the order-disorder transition [26, 27]. Recently the possibility to combine this technology with atomic layer deposition (ALD) has been proposed as a valuable solution to address these challenges [28, 29]. The approach is based on the possibility to selectively control the interaction of ALD precursors with the polymer units forming the block copolymer film. Once again, despite the wide range of selective chemistries that can be envisioned, basing on the enormous library of block copolymers and atomic layer deposition processes, this represents an important limitation to the flexibility of the proposed methodology, since a specific combination of block copolymers and ALD precursors is necessary to achieve the desired nanostructured material. Moreover the use of a polymeric template dramatically reduces the range of temperatures accessible during ALD growth and

consequently limits the choice to the precursors which can be operated at low growth temperatures. Thus the unique capabilities of ALD can be used to fabricate nanostructured oxide surfaces starting from a nanoporous SiO_2 scaffold which is obtained by a combination of block copolymer lithography and reactive ion etching (RIE). The use of an inorganic nanoporous film as a backbone for the ALD deposition removes all the limitations related to the growth temperature and chemical selectivity of the precursors. As a demonstration of this strategy, nanoporous Al_2O_3 films were grown onto the nanoporous SiO_2 film. However this approach is not limited to the use of Al_2O_3 since a large variety of metal oxides or nitrides can be easily grown by choosing appropriate reactants. Therefore, relying on the same lithographic process, it is possible to deliver a broad variety of size controlled nanoporous surfaces with properties accurately designed for specific applications.

For the fabrication of tunable Al_2O_3/SiO_2 templates, nanoporous SiO_2 backbones were prepared starting from a 50 nm thick SiO_2 film. According to previous calibration an etching time of 160 s was selected to maximize the aspect ratio of the nanopores and, at the same time, to avoid over-etching of Si substrate. After the removal of the BC mask by piranha solution, nanoporous SiO_2 was obtained with a mean pore diameter of 23.0 ± 0.1 nm and expected depth of ~ 48 nm. The Al_2O_3 films were grown varying the number of the ALD cycles and thus tuning the thickness of the deposited Al_2O_3 film. Flat SiO_2 substrates were introduced in the ALD reactor during each Al_2O_3 deposition in order to monitor the growth. The thickness of the Al_2O_3 thin film deposited on these surfaces is reported as a function of the number of ALD cycles in figure 4.17. The linear fitting (green line) of the experimental data confirms an average growth rate of 0.09 ± 0.01 nm/cycle. In figure 4.18 the SEM plan view image of the nanoporous SiO_2 template (a) is compared with the images of the nanostrucutred SiO_2 substrate after deposition of 4.6 ± 0.1 nm (b) and 7.9 ± 0.1 nm (c) thick Al_2O_3 thin film. A clear reduction of the pore diameter is observed when increasing the thickness of the Al_2O_3 film. Software analysis (SPIP^{TM}) of the SEM images acquired on the full set of samples allows studying the evolution of the pore diameter as a function of the number of ALD cycles. The results are reported in figure 4.17. The capability of ALD to finely tune the pore size is clearly highlighted by the linear dependence of the nanopore dimension on the number of ALD cycles. The linear decrease in the diameter of the

pores well correlates with the thickness of the deposited Al_2O_3 film, assuming a conformal growth on the walls of the nanopores. Moreover, according to the analysis of SEM data, a complete filling of the nanopores in the SiO_2 template is expected to occur after 122 ALD cycles corresponding to a 10.7 nm thick Al_2O_3 film.

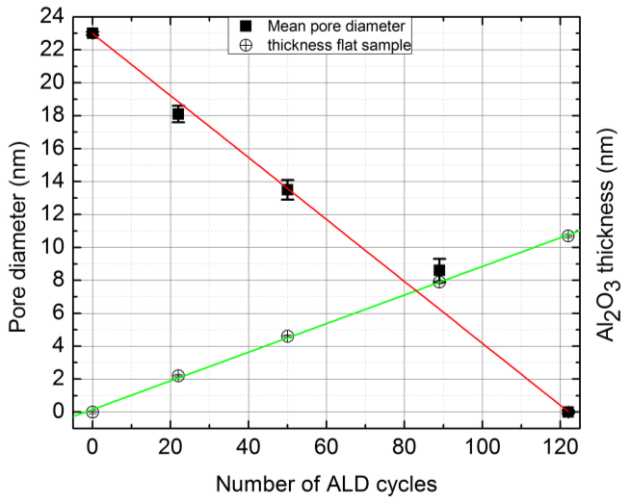

Figure 4.17 Mean pore diameter of Al_2O_3 film on SiO_2 as a function of ALD cycles (red line) and Al_2O_3 thickness of flat sample as a function of ALD cycles (green line).

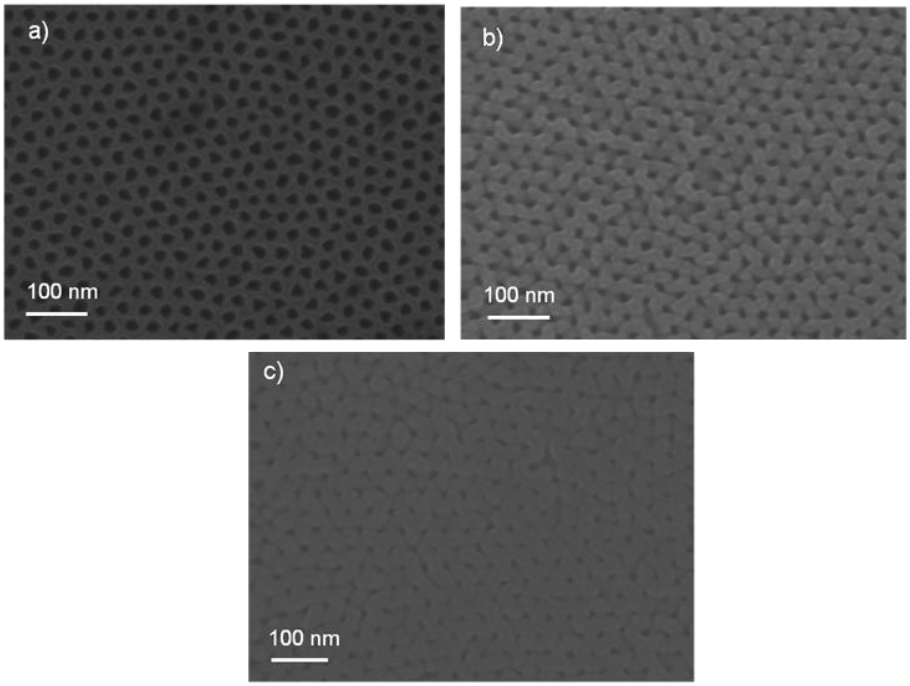

Figure 4.18 SEM plan view images of the nanoporous SiO_2 matrix before ALD deposition (a), after 50 ALD cycles (b) and after 89 ALD cycles (c).

Conformality of the Al_2O_3 films and complete filling of the pores were verified by cross sectional TEM analysis. Figure 4.19 (a) shows the TEM image of the

nanoporous SiO_2 template after 22 ALD cycles, corresponding to the deposition of a 2.2 ± 0.1 nm thick Al_2O_3 film. In the TEM cross section the Al_2O_3 thin film can be distinguished from the SiO_2 matrix due to the different contrast of the two materials. The good conformality of the ALD growth process is confirmed by this image. The thickness of the Al_2O_3 thin film along the walls of the pores was found to be 3.4 ± 0.4 nm, which is slightly higher than the thickness of the Al_2O_3 film deposited on flat SiO_2 substrate. This discrepancy could be related to a different growth rate of Al_2O_3 in the pores or to an experimental artifact related to the cutting of the sample for TEM analysis preparation. As reported in figure 4.17, SEM analysis demonstrates a reduction of the average pore diameter after the ALD growth from 23 ± 0.1 nm to 18.1 ± 0.5 nm after 22 ALD cycles. This variation corresponds to the growth of a 2.2 ± 0.1 nm thick Al_2O_3 film on the walls of the pores, in agreement with the ellipsometric measurement of the Al_2O_3 film deposited on flat surface. The combination of these experimental results suggests that the Al_2O_3 thickness determined by analysis of TEM images could be slightly overestimated because of sample preparation induced artifacts. Finally this TEM image provides a direct confirmation of the conical shape of the pores in the SiO_2 matrix. Figure 4.19 (b) shows the TEM image of the pores after 122 ALD cycles, corresponding to the deposition of a 10.7 ± 0.1 nm thick Al_2O_3 film. TEM cross sectional analysis confirms the complete filling of the pores without any bottleneck-like closure, as often reported in the literature in this kind of structures [30].

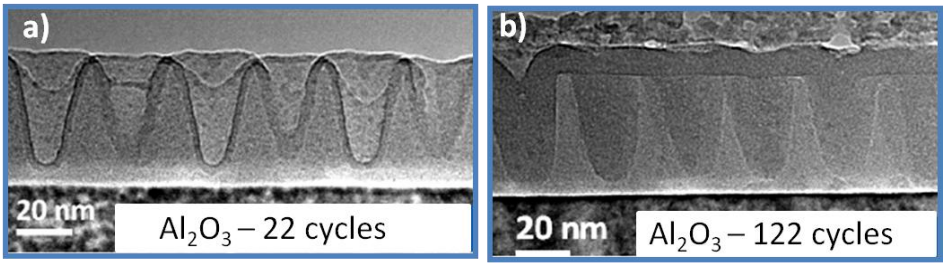

Figure 4.19 TEM images of Al_2O_3 deposited in SiO_2 pores by ALD after 22 cycles (a) and after 122 cycles (a). The darker region in the pores refers to the Al_2O_2 film.

According to previous results, the ALD growth of Al_2O_3 thin film on the nanostructured SiO_2 backbone allows the fabrication of a nanoporous Al_2O_3 surface with tunable pore size. The characteristic dimensions (pore diameter and depth) of the nanoporous Al_2O_3 can be easily varied at nanometer level with extremely high control. This capability of ALD to tune the feature sizes of the nanostructured

oxide, independently by the original dimensions imposed by BC templates, dramatically simplifies the fabrication protocol, because it eliminates the need to prepare different BC templates in order to get different feature size, with remarkable time saving. Moreover it offers the possibility to decouple the control on the pore diameter and on the pore-to-pore distance. In the initial soft PS-*b*-PMMA film the dimension of the pores and their centre-to-centre distance cannot be varied independently since they are related to the length of the PMMA and PS polymeric chains respectively; in order to modify the distance between the pores it is necessary to increase the length of the PS chain. This results in a modified ratio among the two polymeric chains and could influence the phase separation process occurring in the polymeric film. To restore the original ratio it is therefore necessary to increase the length of the PMMA chain, increasing the diameter of the PMMA cylinders and consequently of the pores in the resulting PS matrix. Finally, it should be considered that the tendency of the block copolymer to phase separate is determined by the strength of the repulsive interaction between the two blocks of the polymeric chains. The energy of interaction between PS and PMMA blocks of the copolymer should exceed the critical value for the order-disorder transition [26, 27]. Consequently a minimum number of monomers is required to promote phase separation introducing a limit to the scaling of the length of the polymeric chains. This clearly implies a limit in the scaling of nanopore diameter. The protocol here developed allows overcoming this limitation offering the possibility to tune the nanopores from the original size down to the complete filling of the pores.

The thickness of the nanoporous PS film restricts the possibility to obtain high aspect ratio structure in the SiO_2 template and consequently in the final Al_2O_3 film. It is worth to note that using different random copolymers for substrate neutralization it is possible to modify the width of the window of thicknesses with perpendicular orientation of the nanodomains with respect to the underlying substrate. According to data reported in the literature for this specific PS-*b*-PMMA block copolymer, perpendicular orientation of hexagonally packed PMMA cylinders in a PS matrix can be achieved in a wide range of thicknesses ranging from 20 nm to 40 nm depending on the choice of the random copolymer. Consequently the aspect-ratio of the nanopores in the SiO_2 matrix can be widely increased by proper selection of the PS-*r*-PMMA copolymer.

From a general point of view, the proposed protocol provides a versatile approach to the synthesis of nanostructured substrates. The protocol is fully compatible with conventional silicon technology and the scalability of block copolymer lithography over large areas has already been demonstrated [31]. In principle any material that can be grown following a pure ALD scheme can be integrated into this process. Due to the intrinsic high conformality of the ALD growth, the SiO_2 template can be used as a backbone for the deposition of a large variety of nanoporous surfaces with specific chemical composition. The combination of block copolymer lithography and ALD growth represents a low cost and simple approach to fabricate nanostructured surfaces over wide areas with high reproducibility. In principle it is possible to fabricate the nanostructured oxide surfaces by directly processing the oxide of choice by RIE etching using the nanoporous PS thin film as a mask. Yet this would imply the development of a specific chemistry for the anisotropic etching of each oxide and would not allow overcoming the intrinsic scale limitations of BC lithography. The combination of ALD with nanoporous SiO_2 scaffolds allows to eliminate these technological constrains and to simplify the processing of the materials with remarkable time saving.

4.5 Si nanocrystals fabrication

Fabrication of two dimensional arrays of Si nanocrystals embedded or deposited on top of a SiO_2 matrix has been achieved in different ways as reported in the literature works [32, 33, 34, 35, 36, 37, 38, 39, 40]. In this thesis we aim to use block copolymer as template for the fabrication of ordered arrays of Si nanocrystals with controlled size and shape. Using the nanostructured polymeric mask we want to control the in plane positioning of the nanoparticles in order to achieve a complete control on their placement within the SiO_2 matrix. Two different approaches were pursued leading to different configurations where nanodots are embedded/deposited in/on the dielectric matrix. The first approach is based on **ion beam synthesis** and consists in the implantation of Si ions into the nanostructured polymeric film to locally introduce the desired ion supersaturation, such as silicon for example, in a limited nanosized area. After removal of the polymeric film, a thermal annealing leads to the formation of nanocrystals at a depth depending on the ion energy. No

results are available in the literature about ion implantation throughout block-copolymers nanostructured templates. The second approach is the **lift-off process** that includes material deposition by e-beam evaporation onto the nano-structured polymeric film and on the exposed substrate regions followed by the subsequent removal of the polymeric template and material excess by wet or dry etching. Even if few reports are available in the literature, the feasibility of this lift-off process has already been demonstrated for the deposition of metallic and silicon oxide nanocrystals [41]. The results of these two experimental approaches are described in details in the following sections.

4.5.1 Ion Beam Synthesis

The ion implantation process was performed in Toulouse at CEMES laboratory into a 16 nm thick thermally grown SiO_2 film covered with a 20 nm thick nanoporous PS mask. Si^+ ions were implanted at 1 keV with different doses. A schematic drawing of the process is shown in figure 4.20. Three different implantation doses were investigated: $5x10^{15}cm^{-2}$, $7.5x10^{15}cm^{-2}$ and $1x10^{16}cm^{-2}$. In figure 4.21 EFTEM plan view images of the samples implanted at 1 keV with $5x10^{15}cm^{-2}$ (a) and the $1x10^{16}cm^{-2}$ (b) doses are reported as references. Isolated silicon nanoparticles were observed in the sample implanted with a dose of $5x10^{15}cm^{-2}$ while rather connected nanoparticles were observed in the sample implanted with a dose of $1x10^{16}cm^{-2}$.

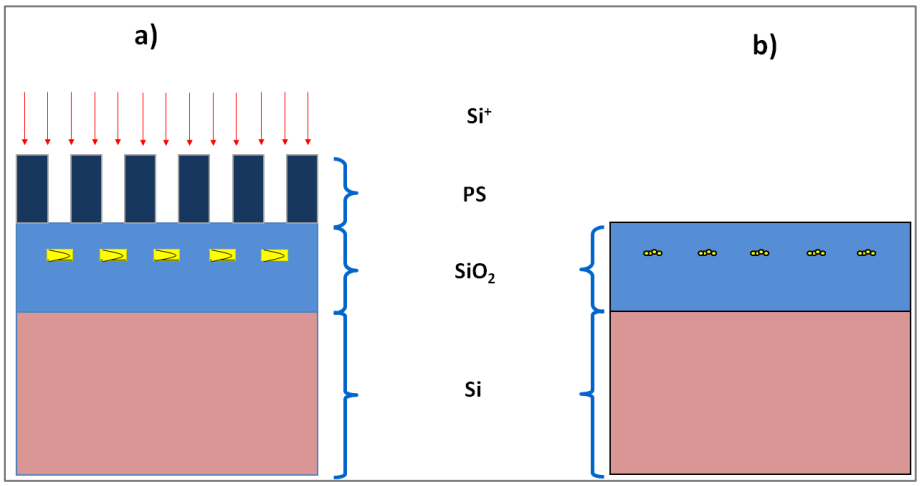

Figure 4.20 Schematic illustration of the ULE-IBS. Si^+ ions are implanted through the PS mask (a). Si nanocrystals formation should happen after the removal of the mask and the subsequent thermal treatment (b).

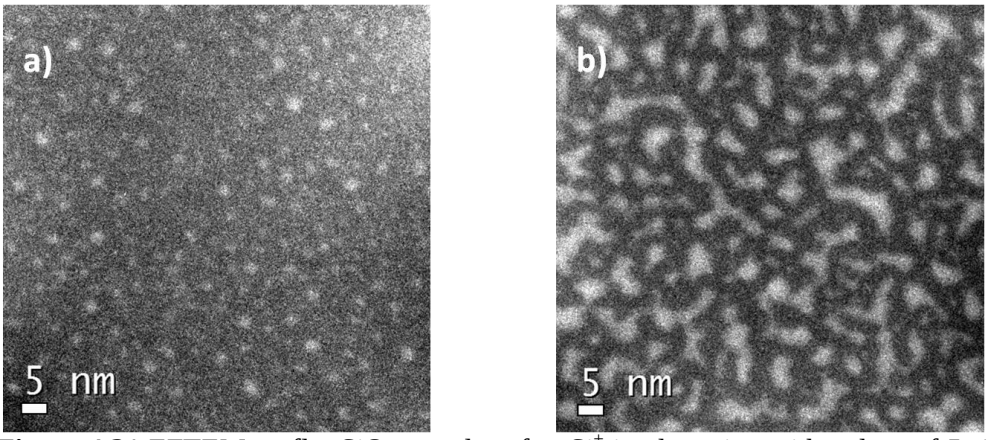

Figure 4.21 EFTEM on flat SiO_2 samples after Si^+ implantation with a dose of $5x10^{15}cm^{-2}$ (a) and with a dose of $1x10^{16}cm^{-2}$ (b).

In order to study the implantation process through the nanoporous polymeric mask we performed a systematic ToF-SIMS analysis of the implanted and annealed samples. The ToF SIMS profiles of the samples implanted at 1 keV with a fluence of $5x10^{15}cm^{-2}$ are reported in figure 4.22. The figure 4.22(a) shows the profile on Si^+ ion implanted through the PS mask: the yellow signal refers to the C and indicates the PS matrix. The red signal refers mainly to the SiO_2 host matrix. The blue signal indicates the Si which is present into the matrix. The saturation of this signal indicated the Si substrate. In the first layers Si signal presents two well defined bumps which corresponds to the Si^+ ions implanted in the PS matrix and in the underlying SiO_2 respectively. In figure 4.22(b) the ToF-SIMS profile of the same sample after removal of the PS matrix is reported. Due to the successful removal of the PS mask a clear reduction of the yellow signal is observed. Moreover 3-4 nm below the surface of the SiO_2 film there is a clear bump of the blue Si signal, which corresponds to a decrease in the red signal indicating the SiO_2. This evolution of the ToF-SIMS signals is determined by the presence of a local excess of silicon in the first layers of the SiO_2 matrix due to the Si^+ ions implanted through the polymeric mask. Figure 4.22(c) refers to the implantation of Si^+ ions into a flat SiO_2 surface without the nanoporous polymeric mask: a similar trend for the silicon related signals is observed with a bump of the Si^- secondary ions located 3-4 nm below the SiO_2 surface. The intensity of the signal is much higher compared to the one observed in figure 4.22(b) due to the different effective dose in the two cases.

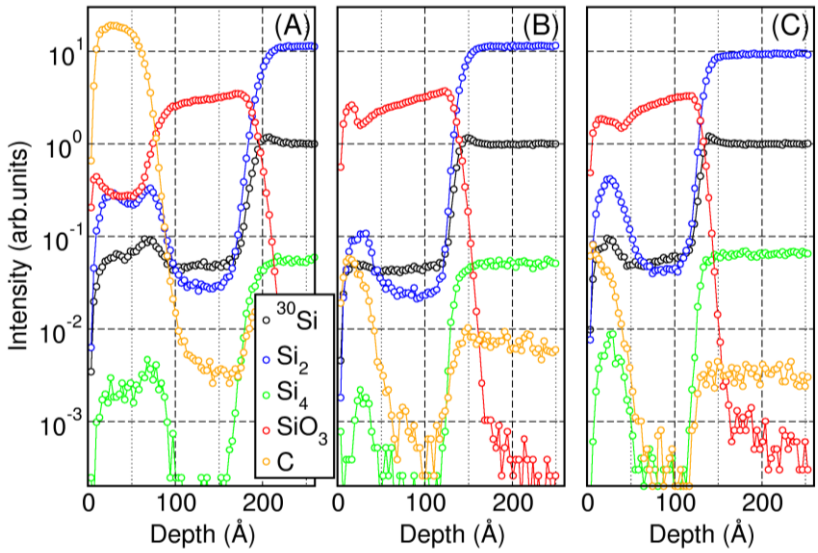

Figure 4.22 ToF SIMS profiles of the implanted Si ion in a SiO_2 matrix with a dose of $5x10^{15}cm^{-2}$. The implantation was performed through the PS mask (a), then the mask was removed (b). The implantation of a flat sample was also performed (c).

The same analysis was performed after the thermal treatment. The samples were annealed in a tubular furnace at 1050 ° C, in N_2 atmosphere. The left part of the figure 4.23 shows the ToF SIMS profile of the SiO_2 host matrix after the implantation of Si^+ ions by ULE-IBS as already reported in the figure 4.22(b). The right part of the figure 4.23 shows the same matrix after the annealing process: the main difference between the two profiles is the increased blue Si signal located 3-4 nm below the surface. This increase indicates a modification of the chemical state of silicon in the implanted matrix and it is usually related to a possible formation of Si nanoclusters in the SiO_2 matrix. Nevertheless the TEM analysis performed on this sample, shown in figure 4.24, indicates no formation of isolated Si nanoparticles like the ones observed in the sample implanted without the polymeric mask (figure 4.21(a)). This result can be related to different effects. One possible reason is a dose loss due to the charging of the PS mask during the implantation, which causes a screening of the ions. Another possibility is related to different nucleation and growth mechanisms of the Si nanoclusters when the silicon excess is generated in very small nanovolumes.

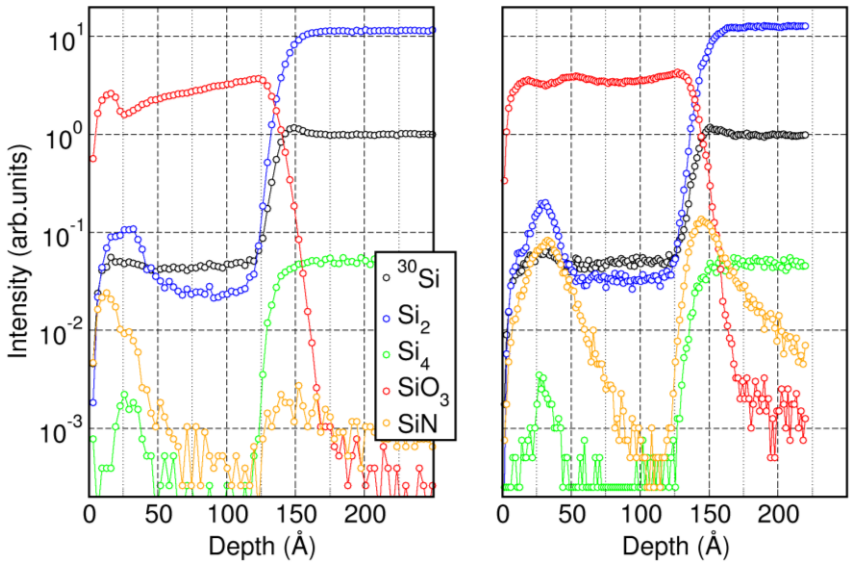

Figure 4.23 ToF SIMS profiles of the implanted Si ion in a SiO_2 matrix with a dose of $5x10^{15}cm^{-2}$ after the removal of the polymeric mask (left) and after the annealing process (right).

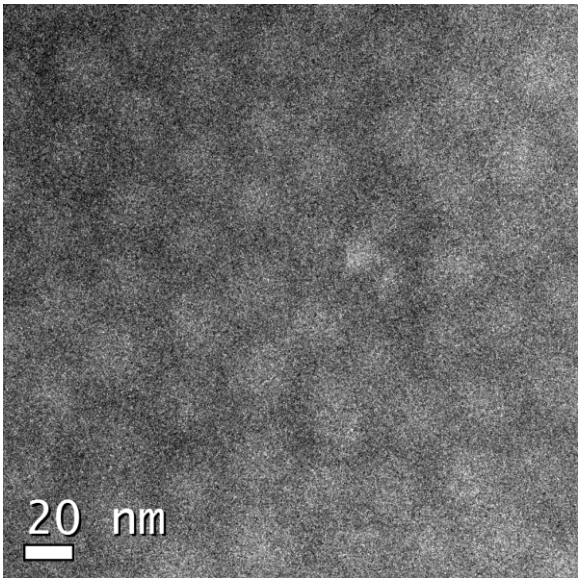

Figure 4.24 EFTEM on SiO_2 host matrix after Si^+ implantation with a dose of $5x10^{15}cm^{-2}$ through the PS mask.

Figure 4.25 reports the ToF SIMS profiles of the samples implanted with a fluence of $1x10^{16}$ cm^{-2} at 1 keV. As in the previous case, the yellow signal in the figure 4.25(a), which refers to the C, indicates the polymeric mask. The blue signal related to Si presents the two bumps that indicate the presence of implanted materials in the PS mask and in the SiO_2 matrix as well. After the removal of the polymeric mask,

the bump of Si signal can be observed in correspondence of the lowering of the red signal related to SiO_2, as depicted in figure 4.25(b). Also in this case the blue Si signal presents a peak 3-4 nm below the SiO_2 surface. Figure 4.25(c) refers to the implantation in a flat sample and thus the intensity of the Si signal and exhibits higher Silicon related signals compared to the sample implanted through the nanoporous polymeric mask. Figure 4.26 reports the ToF SIMS profile of the sample implanted with $1x10^{16}cm^{-2}$ before and after the annealing at 1050 ° C in nitrogen atmosphere. The left part of the figure 4.26 shows the ToF SIMS profile of the SiO_2 host matrix after the implantation of Si^+ ions by ULE-IBS as already reported in the figure 4.25(b). The right part of the figure 4.26 shows the same matrix after the annealing process. The increase of the silicon related signals indicates a modification of the chemical state of silicon in the implanted matrix. In this case the TEM analysis, shown in figure 4.27, indicates a formation of small isolated Si nanoparticles which resemble the PS template: this result is similar to the implantation performed on the flat sample with a dose of $5x10^{15}cm^{-2}$ thus confirming the screening effect of the PS mask and the necessity to increase the implantation dose in order to obtain nanoclusters formation.

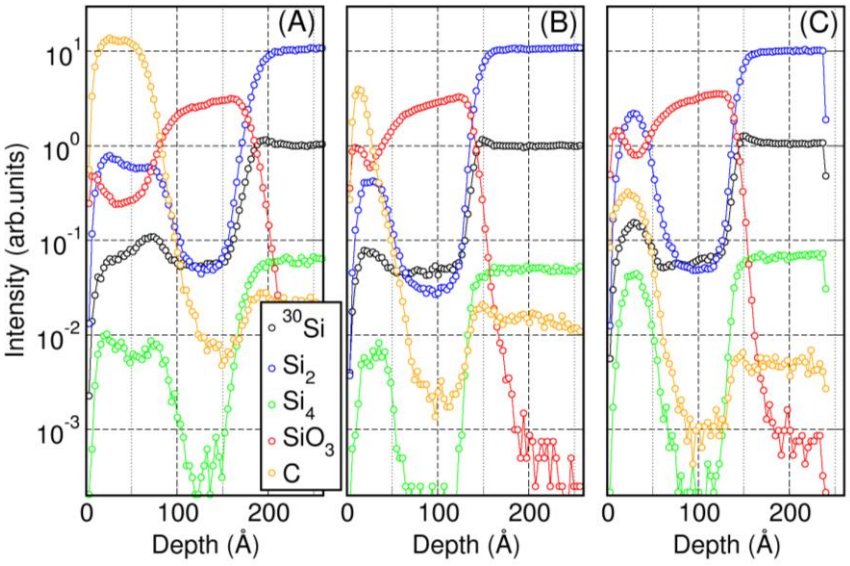

Figure 4.25 ToF SIMS profiles of the implanted Si ion in a SiO_2 matrix with a dose of $1x10^{16}cm^{-2}$. The implantation was performed through the PS mask (a), then the mask was removed (b). The implantation of a flat sample was also performed (c).

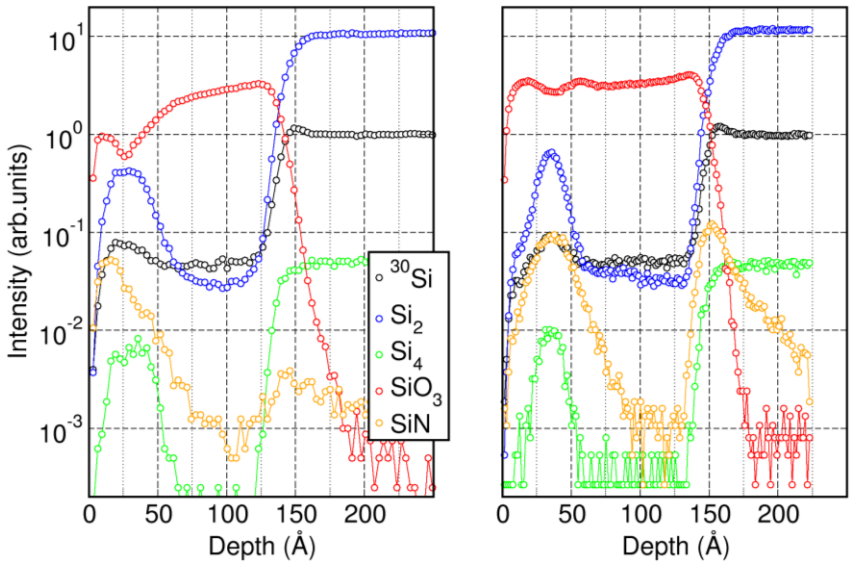

Figure 4.26 ToF SIMS profiles of the implanted Si ion in a SiO_2 matrix with a dose of $1x10^{16}cm^{-2}$ after the removal of the polymeric mask (left) and after the annealing process (right).

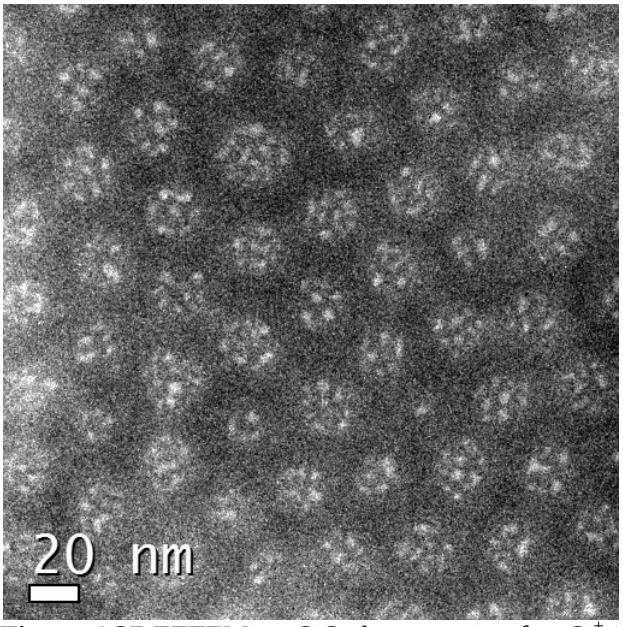

Figure 4.27 EFTEM on SiO_2 host matrix after Si^+ implantation with a dose of $1x10^{16}cm^{-2}$ through the PS mask.

4.5.2 Lift off

The other approach used to fabricate Si nanocrystals is the lift off process. Figure 4.28 shows the fundamental steps of lift-off process. Amorphous silicon is deposited by e-beam evaporation through the nanoporous PS mask. The protocol for the fabrication of the soft polymeric mask has already been described in details

in section 4.2. The excess of material and the polymeric films are finally removed by degradation in Piranha solution. In order to get a successful lift off process, the thickness of evaporated material cannot exceed the thickness of the PS mask which in these specific samples is 21 nm.

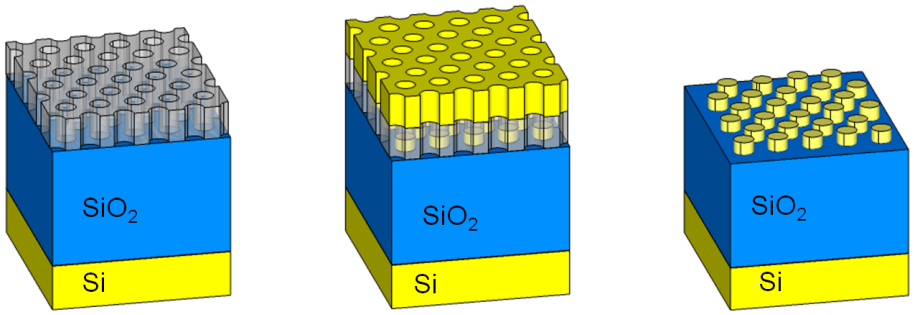

Figure 4.28 Lift off process: PS soft mask (left), deposition by e-beam evaporation (middle) and removal of the PS mask (right).

The resulting silicon dots can be viewed in the SEM image reported in figure 4.29. By means of statistical analysis of this image, a mean pore diameter of 18.1 ± 0.7 nm is measured for the Si dots. In order to measure the real thickness of the dots, AFM analysis of two samples with different nominal thickness of the deposited Si layer was performed in Barcelona with a Multimode Nanoscope V Controller. A silicon nitride cantilever with a low spring constant and a silicon tip, which can reach a radius of about 2 nm, have been used for AFM analysis. According to AFM measurements, the thickness of the Si dots was determined to be 7.4 ± 0.6 nm and 10.3 ± 0.7 nm for samples with nominal thickness of 7 nm and 10 nm respectively. In principle the AFM allows also measuring the dot diameter, but the measure is affected by the tip size and thus it overestimates the dimension. The SEM analysis resulted more accurate in this case. Also the SiO was deposited by e-beam evaporation: the dots resulted in a lower mean diameter (17.1 ± 0.4 nm) while the height was 6.1 ± 0.4 nm when the nominal thickness was 6 nm. These data demonstrated the precise control at nanometric scale which allows obtaining two dimensional ordered arrays of dots.

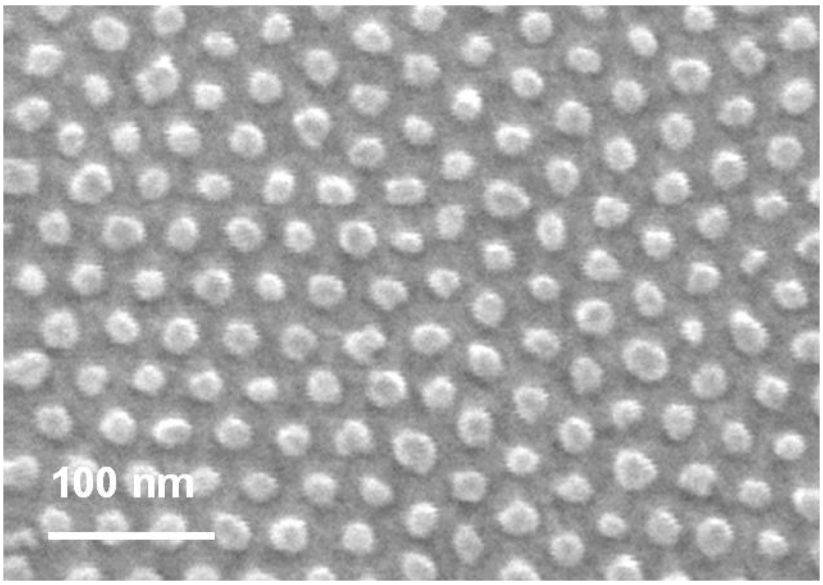

Figure 4.29 SEM image of Si dots obtained by e-beam evaporation and lift off.

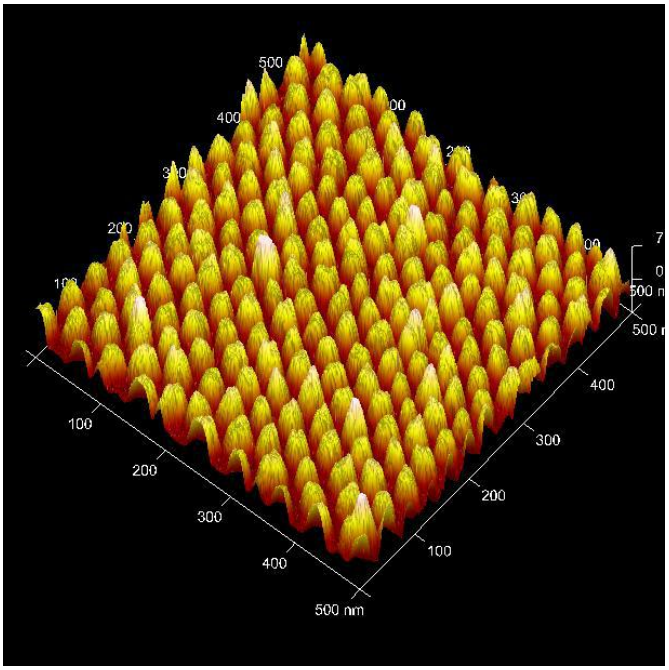

Figure 4.30 AFM image of Si dots obtained by lift off.

The amorphous Si dots were then covered with a 10 nm thick SiO_2 e-beam evaporated film and subsequently annealed at high temperature in order to synthesize the Si nanocrystals. The annealing was performed in a tubular furnace at 1050 °C in nitrogen atmosphere for 30 min. The ToF SIMS data reported in figure 4.31 refer to the sample before the annealing (left image) and after the annealing (right image). The thickness of the Si deposited in this case was 5 nm as can be

deduced by the blue Si signal in the range depth from 10 nm to 20 nm the peak. This signal remains even after the annealing and it indicates the presence of a silicon rich layer. TEM analysis was performed on these samples which gave interesting information. Figure 4.32 shows HRTEM images of the sample with e-beam evaporated Si and 10 nm thick SiO_2 covering. The analysis demonstrated the particles are crystalline with a diameter of 3.4 ± 0.2 nm. EFTEM analysis at 17 eV, reported in figure 4.33, shows agglomeration of Si nanoparticles (white objects). The calculated density of nanocrystals is (7.6 ± 1.5) $x10^{11}$ cm^{-2}. Cross sectional analysis, shown in figure 4.34, indicated that the SiO_2 surface has a periodic morphology. In fact the lateral dimensions of the Si nanocrystals agglomerates after annealing is 11.1 ± 0.4 nm and the height is 4.3 ± 0.2 nm. According to these data the volume of the Si nanocrystals agglomerates is only 15% of the volume of the original amorphous Si dots. From the comparison of SEM/AFM data of the as deposited sample and TEM analysis of the annealed one, a shrinking of the nanoparticles was observed to occur during the thermal treatment thus suggesting a possible silicon oxidation that limits the size of the nanocrystals. The oxidation of the nanoparticles can be due to different factors, such as air absorption, oxygen contaminants during evaporation or annealing or either it can be due to piranha solution used to remove the PS mask after evaporation. Presence of oxygen contaminants in Si grains and gettering of residual oxygen species in the vacuum chamber can cause nanoparticles oxidation during the e-beam evaporation. Furthermore the native oxide formation should be considered even if the thickness of the native oxide does not exceed 2 nm. Since the annealing was performed in ultrapure N_2 atmosphere, no oxygen contaminations derive from this process. Further analyses are currently in progress to investigate this point.

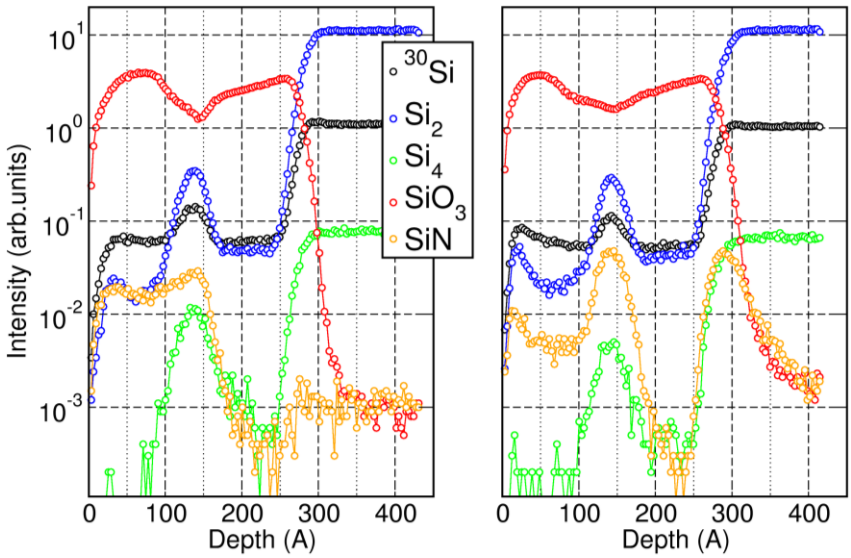

Figure 4.31 ToF SIMS profiles of e-beam evaporated Si covered with 10 nm thick SiO_2 matrix as deposited (left) and annealed (right).

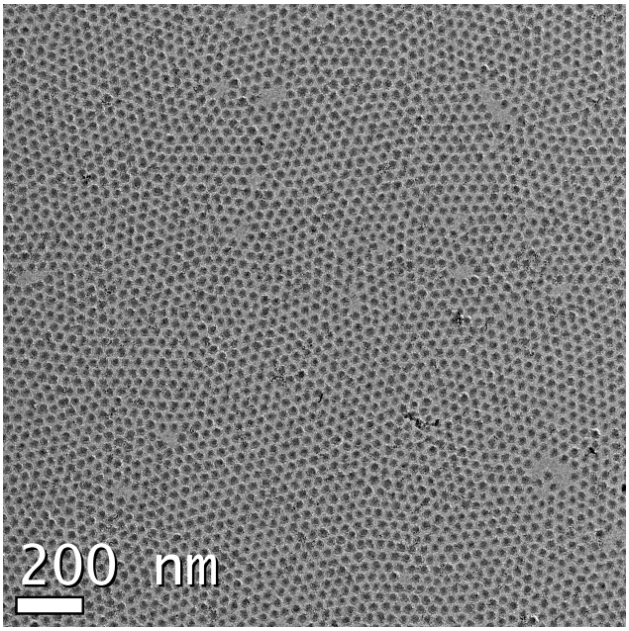

Figure 4.32 HRTEM on SiO_2/Si/SiO_2 multilayer.

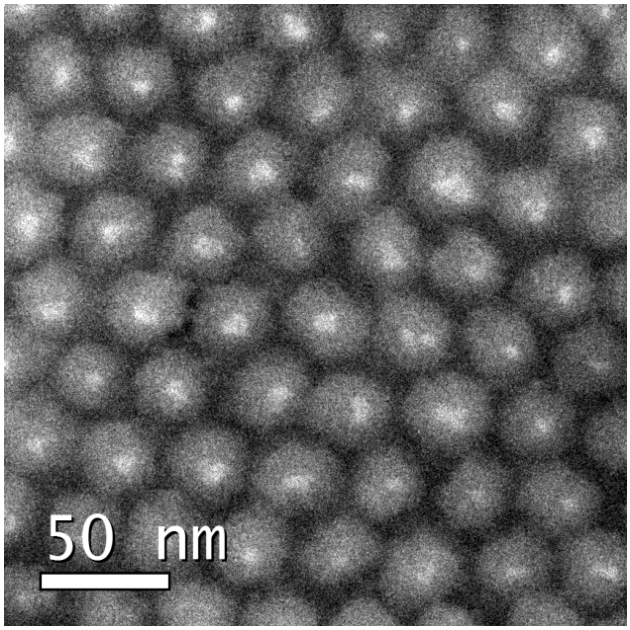

Figure 4.33 EFTEM on $SiO_2/Si/SiO_2$ multilayer.

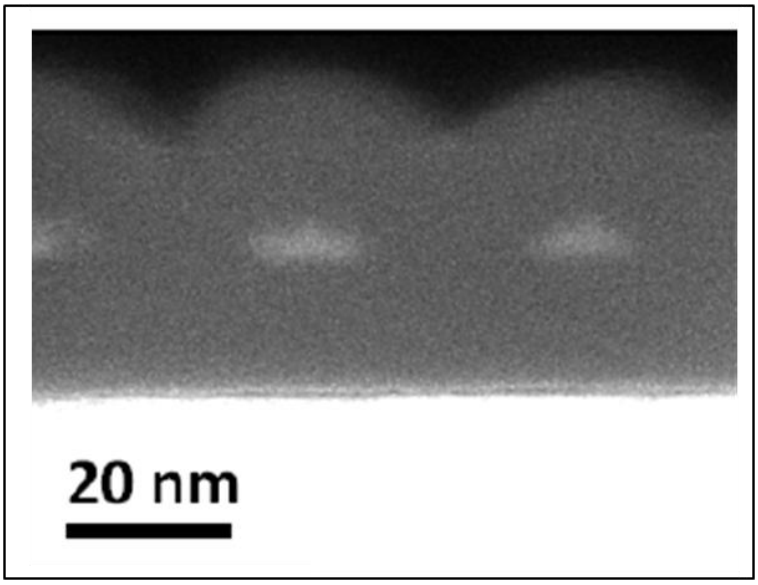

Figure 4.34 Cross section TEM on the $SiO_2/Si/SiO_2$ multilayer.

4.6 Graphoepitaxy

In this last section of the chapter we explore the possibility to control the in plane positioning of the nanoporous template by depositing the BC thin film on pre-patterned surfaces reducing defects in the periodic arrangement and improving the long range ordering. This approach is usually referred as graphoepitaxy. Among the range of strategies to achieve long-range lateral ordering, graphoepitaxy offers a rich opportunity for studies of self-assembly behavior in confined environments and represents a valid source of innovation in nanofabrication methods [42, 43, 44, 45, 46, 47]. Graphoepitaxy is based on the combination of the bottom up approach of block copolymers with the top down approach of conventional lithography. In this way it is possible to register the periodic domains of the self assembled block-copolymer film with the underlying topographic structure to improve the long range order of the nanostructures.

The pre-patterned SiO_2 templates were fabricated by e-beam lithography. The 996K PMMA diluted in anisole solution is spin coated on the SiO_2 substrate, exposed to e-beam at different doses and finally developed in Methyl isobutyl ketone:isopropyl alcohol (MIBK:IPA) solution for 30 seconds. The defined trenches in the PMMA thin film were finally transferred into the SiO_2 substrate by means of RIE. Trenches with width ranging from 20 nm to 260 nm were fabricated in the SiO_2 matrix. By properly adjusting the RIE etching time the depth of the trenches in SiO_2 was varied from 30 nm to 120 nm.

Cylinder forming PS-*b*-PMMA block copolymers thin films were deposited on the pre-patterned substrates by spin coating after proper neutralization of the substrate by means of R62 PS-*r*-PMMA according to the recipe we optimized for flat substrates. The parameters of the spin coating were varied in order to obtain the desired thickness of the BC thin films. A systematic study of BC thin films arrangement inside the SiO_2 trenches was performed: for each SiO_2 trench depth (30 nm, 60 nm, 90 nm and 120 nm), several BC thicknesses were deposited (20 nm, 25 nm, 30 nm and 35 nm). The samples were then annealed in vacuum for 120 minutes in order to promote self organization.

In the samples with film thickness of 30 nm and 35 nm, no confinement was observed regardless of the trench depth and trench width. Thus we focused on the

samples with thickness of 20 and 25 nm: the width of the trench has a fundamental role in determining the confinement of the film since below a width of 120 nm the film cannot arrange inside the trench, but it remains suspended-like. Figure 4.35 shows different confinements of a 20 nm PS-*b*-PMMA film in a 120 nm trench depth as a function of the trench width. In figure 4.35 (a) the rearrangement of the BC film can be appreciated: the film lost his organization next to the trench in order to organize inside the trench. Reducing the trench width to 120 nm allowed the film to organize inside trench, but the region in which the film did not organize is little compared to the previous one, as depicted in figure 4.35 (b). When the trench width was 80 nm the film didn't reorganize and preferred maintaining its initial arrangement, as depicted in figure 4.35 (c).

In order to induce reorganization of the BC film inside the trenches and to avoid such suspension-like behavior of the film, the distance between the trenches was varied. The distance between two adjacent trenches, from the corresponding edges, was selected to be 2w, 3w, 5w and 8w, where w indicates the trench width. Figure 4.36 shows a SEM image with a film thickness of 25 nm in a trench with depth of 90 nm and width of 260 nm. In this case the distance between the trenches is 2w and thus the surface between the edges of the trenches is 260 nm. A reduction of BC defectiveness is clearly visible: the low distance between trenches forces the BC to break the periodicity and to fall inside the trenches. This phenomenon occurs for all the trench widths down to 80 nm and for distances of 2w, 3w and 5w. Figure 4.37 shows a SEM image with a film thickness of 25 nm in a trench depth of 90 nm and width of 80 nm. The distance between trenches is 3w: also in this case the periodicity of the film is broken and thus it could rearrange inside the trench, differently from the situation depicted in figure 4.35 (c).

When the distance between trenches is 8w, the trenches are isolated and no proximity effect occurs: for low trench width, i.e. 80 nm and below, the surface tension prevents the BC to fall inside trenches and a continuous BC film cover the surface without filling the trenches. An example of this peculiar behavior is provided by figure 4.38 in which the BC thickness is 25 nm, the trench depth 120 nm and the trench width 80 nm. According to these results a proper filling of the trenches by the polymeric film can be achieved only by properly combining the thickness of the PS thin film, the width of the trenches fabricated in the SiO_2 as well as the distance among the different trenches.

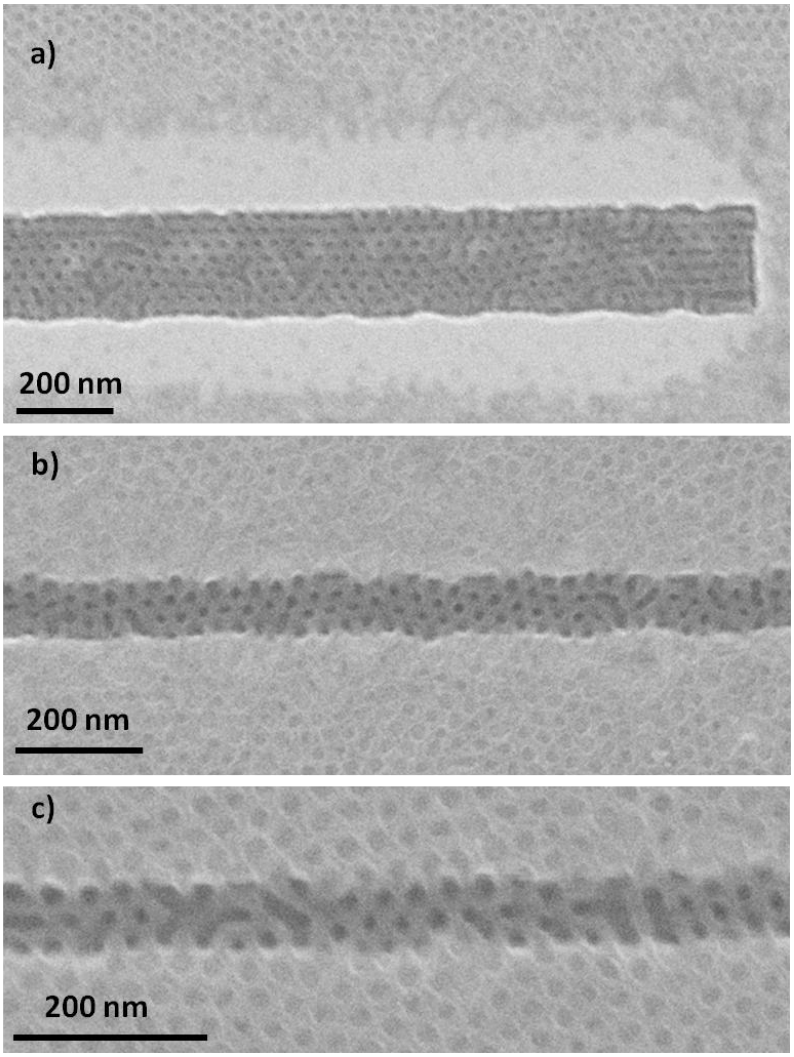

Figure 4.35 SEM images of 20 nm PS-*b*-PMMA film deposited inside 120 nm SiO_2 trench with a trench width of 240 nm (a), 120 nm (b) and 80 nm (c).

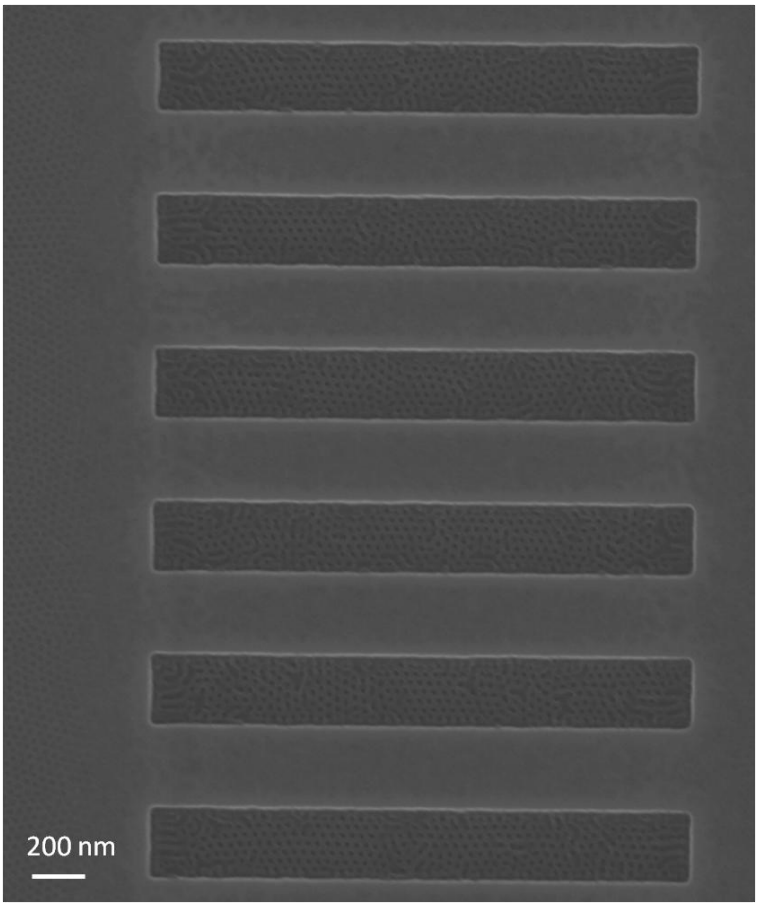

Figure 4.36 SEM image of PS-*b*-PMMA deposited inside SiO_2 trench with a distance of 260 nm.

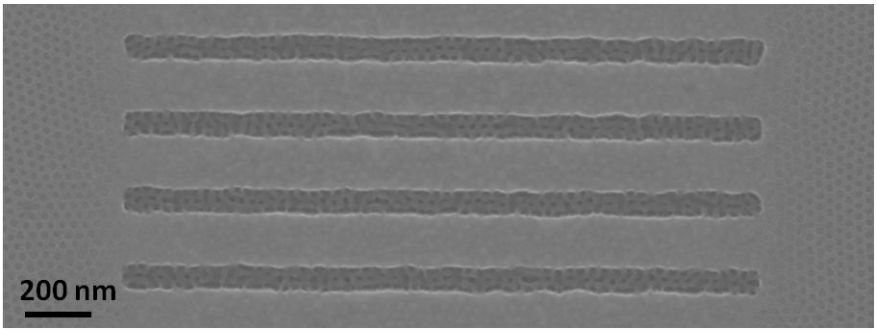

Figure 4.37 SEM image of PS-b-PMMA deposited inside SiO_2 trench with a distance of 160 nm.

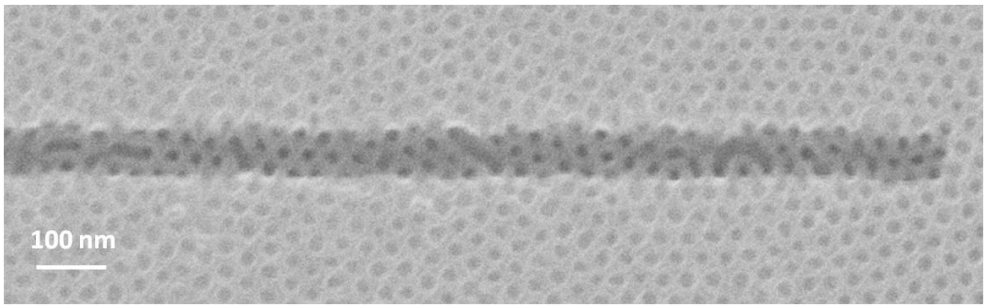

Figure 4.38 SEM image of PS-*b*-PMMA deposited inside SiO_2 trench whose width is 80 nm.

Nevertheless the presence of defects, even with the improvement in the fabrication of the trenches, is clearly visible within the trenches while a perfect organization of the BC thin film is achieved outside the topographic structures. The origin of these defects could be the roughness of the SiO_2 at the bottom of the trenches. According to AFM analysis, the roughness of the SiO_2 surface after RIE exposure seems not to critically affect the BC deposition. Moreover it is interesting to note that various works in literature report time of annealing much longer than the ones we performed in this thesis work [48, 49]. Longer annealing time could promote self-organization and minimize the defectiveness in the topographic structures. Thus an annealing of 24 hours instead of 2 hours was performed and the improved organization of the BC films inside the trenches is clearly visible in figure 4.39.

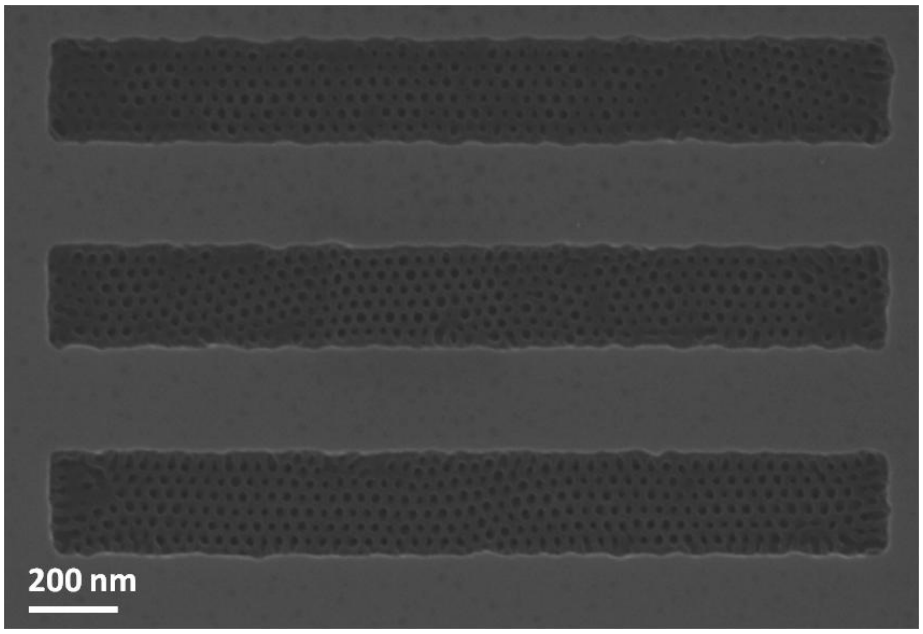

Figure 4.38 SEM image of 25 nm PS-*b*-PMMA deposited inside 90 nm SiO_2 trench with a distance of 240 nm. The film was annealed for 24 hours.

Finally, an interesting result is shown in figure 4.39: ordered arrays of dots were fabricated in a selected area of the sample by means of TSA. Precisely these dots were obtained by *soft graphoepitaxy*, which is an emerging technique in the field of graphoepitaxy [50, 51, 52]. The difference is that the deposition of block copolymers is performed directly through the trenches of the resist. This allows avoiding the RIE step and the nanostructures are fabricated on the SiO_2 surface.

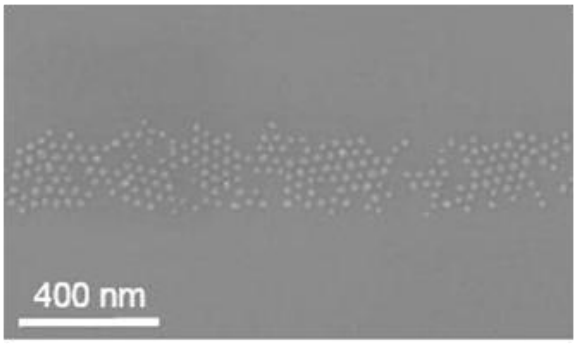

Figure 4.39 SEM image of Si dots fabricated by soft graphoepitaxy.

References

1 T. Thurn-Albrecht, J. DeRouchey, T. P. Russell and H. M. Jaeger, *Macromolecules* **33,** 3250 (2000)

2 T. Thurn-Albrecht, J. DeRouchey, T. P. Russell and R. Kolb, *Macromolecules* **35**, 8106 (2002)

3 S. H. Kim, M. J. Misner, T. Xu, M. Kimura and T. P. Russell, *Adv. Mater.* **16,** 226 (2004)

4 Y. Xuan, J. Peng, L. Cui, H. Wang, B. Li and Y. Han, *Macromolecules* **37**, 7301(2004)

5 P. Mansky, Y. Liu, E. Huang, T. P. Russell and C. J. Hawker, *Science* **275**, 1458 (1997)

6 D. Y. Ryu, S. Ham, E. Kim, U. Jeong, C. J. Hawker and T. P. Russell, *Macromolecules* **42**, 4902 (2009)

7 E. Huang, S. Pruzinsky, T. P. Russell, J. Mays, C. J. Hawker, *Macromolecules* **32**, 5299 (1999)

8 P. Mansky, T. P. Russell, C. J. Hawker, J. Mays, D. C. Cook, S. K. Satija, *Phys. Rev. Lett.* **79**, 237 (1997)

9 P. Mansky, T. P. Russell, C. J. Hawker, M. Pitsikalis, J. Mays, *Macromolecules* **30**, 6810 (1997)

10 K. W. Guarini, C. T. Black, S. H. I. Yeung, *Adv. Mater.* **14**, 1290 (2002)

11 I. A. Zucchi, E. Poliani and M. Perego, *Nanotechnology* **21**, 185304 (2010)

12 Polymer Source Inc.

13 S. Ham, C. Shin, E. Kim, D. Y. Ryu, U. Jeong, T. P. Russell and C. J. Hawker, *Macromolecules* **41**, 6431 (2008)

14 U. Cvelbar, N. Krstulovic, S. Milosevic and M. Mozetic, *Vacuum* **82**, 224 (2008)

15 K. W. Guarini, C. T. Black, K. R. Milkove and R. L. Sandstrom, *J. Vac. Sci. Technol. B* **19**, 2784 (2001)

16 J.-W. Lee, S.-W. Ryu, D. O. Shin, B. H. Kim, S. O. Kim and Y.-K. Choi, *Solid-State Electronics* **53**, 640 (2009)

17 D. H. Lee, D. O. Shin, W. J. Lee and S. O. Kim, *Adv. Mater.* **20**, 2480 (2008)

18 U. Jeong, D. Y. Ryu, K. J. Kim, D. H. Kim, T. P. Russell and C. J. Hawker, *Adv. Mater.* **15**, 1247 (2003)

19 E. Han, K. O. Stuen, Y. La, P. F. Nealey and P. Gopalan, *Macromolecules* **41**, 9090 (2008)

20 E. W. Edwards, M. F. Montague, H. H. Solak, C. J. Hawker and P. F. Nealey, *Adv. Mater.* **16**, 1315 (2004)

21 C. T. Black, K. W. Guarini, Y. Zhang, H. Kim, J. Benedict, E. Sikorski, I. V. Babich and K. R. Milkove, *IEEE Electron Device Letters* **25**, 622 (2004)

22 S. Y. Yang, J. Park, J. Yoon, M. Ree, S. K. Jang and J. K. Kim, *Adv. Mater.* **18**, 1371 (2008)

23 G. Liu and J. Ding, *Adv. Mater.* **10**, 69 (1998)

24 R. Elghanian, J. J. Storhoff, R. C. Mucic, R. L. Letsinger and C. A. Mirkin, *Science* **277**, 1078 (1997)

25 G. Gay, T. Baron, C. Agraffeil, B. Salhi, T. Chevolleau, G. Cunge, H. Grampeix, J.-H. Tortai, F. Martin, E. Jalaguier and B. De Salvo, *Nanotechnology* **21**, 435301 (2010)

26 F. S. Bates and G. H. Fredrickson, *Phys. Today* **52**, 32 (1999)

27 H.-C. Kim, S.-M. Park and W. D. Hinsberg, *Chem. Rev.* **110**, 146 (2010)

28 Q. Peng, Y.-C. Tseng, S. B. Darling and J. W. Elam, *Adv. Mater.* **22** 5129 (2010)

29 S. M. George, *Chem. Rev.* **110** 111 (2010)

30 A. Asatekin and K. K. Gleason, *Nano Letters* **11** 677 (2010)

31 W.-K. Li and S. Yang S, *J.Vac. Sci. Technol. B* **25**, 1982 (2007)

32 E. Kapetanakis, P. Normand, D. Tsoukalas, and K. Beltsios, *Appl. Phys.Lett.* **80**, 2794 (2002)

33 T. Shimizu-Iwayama, S. Nakao and K. Saitoh, *Appl. Phys. Lett.* **65**, 1814 (1994)

34 M. Perego , S. Ferrari, S. Spiga, E. Bonera, V. Soncini and M. Fanciulli, *Appl. Phys. Lett.* **82**, 121 (2003)

35 M. Perego , S. Ferrari, G. BenAssayag, C.Bonafos, M. Carrada, A. Claverie and M. Fanciulli, *Appl. Phys. Lett.* **95**, 257 (2004)

36 L. Bychto, M. Balaguer, E. Pastor, V. Chirvony and E. Matveeva, *J. Nanopart. Res.* **10**, 1241 (2008)

37 S.Decossas, F. Mazen, T. Baron, G. Brémond and A. Souifi, *Nanotechnology* **14**, 1272 (2003)

38 A. A. Guzelian, J. E. B. Katari, A. V. Kadavanich, U.Banin, K. Hamad, E. Juban, A. P. Alivisatos, R. H. Wolters, C. C. Arnold, and J. R. Heath, *J. Phys. Chem.* **100**, 7212 (1996)

39 O. I. Micic and A. J. Nozik, *J. Luminesc*. **70**, 95 (1996)

40 W. Seifert, N. Carlsson, M. Miller, M.-E. Pistol, L. Samuelson and R. Wallenberg, *Progr. Crystal Growth Charact.* **33**, 423 (1996)

41 K. W. Guarini, C. T. Black, K. R. Milkove and R. L. Sandstrom, *J. Vac. Sci. Technol.* B **19** 2784 (2001)

42 J. Y. Cheng, C. A. Ross, H. I. Smith and E. L. Thomas, *Adv. Mater.* **18**, 2505 (2006)

43 E. Han, H. Kang, C.-C. Liu, P. F. Nealey and P. Gopalan, *Adv. Mater.* **22**, 4325 (2010)

44 S.–M. Park, M. P. Stoykovich, R. Ruiz, Y. Zhang, C. T. Black and P. F. Nealey, *Adv. Mater*. **19**, 607 (2007)

45 R. A. Segalman, H. Yokoyama, E. J. Kramer, *Adv. Mater.* **13**, 1152 (2001)

46 R. A. Segalman, A. Hexemer, E. J. Kramer, *Macromolecules* **36**, 6831 (2003)

47 D. Sundrani, S. B. Darling, S. J. Sibener, *Nano Lett.* **4**, 273 (2004)

48 S. Xiao, X. Yang, E. W. Edwards, Y.-H. La and P. F. Nealey, *Nanotechnology* **16**, S324 (2005)

49 G. B. Kang, S.-I. Kim, Y. T. Kim, J. H. Park, *Current Applied Physics* **9**, S82 (2009)

50 S.-J. Jeong, H.-S. Moon, J. Shin, B. H. Kim, D. O. Shin, J. Y. Kim, Y.-H. Lee, J. U. Kim and S. O. Kim, *Nano Letters* **10**, 3500 (2010)

51 S.-J. Jeong, J. E. Kim, H.-S. Moon, B. H. Kim, S. M. Kim, J. B. Kim and S. O. Kim, *Nano Letters* **9**, 2300 (2009)

52 S.-J. Jeong and S. O. Kim, *J. Mater. Chem.* **21**, 5856 (2011)

Chapter 5

Conclusions and perspectives

The main objective of research activity carried out at MDM Laboratory during my PhD was the growth and manipulation of nano-objects to be used as building blocks for the fabrication of new generation of nano-transistors, nano-memories and nano-emitters. Block copolymers are considered an extremely promising and low cost tool in order to overcome the limitations of conventional photolithography techniques.

One of the main challenging issues in this field is related to the implementation of reliable protocols for the combination of these new nano-lithographic tools with standard semiconductor processing techniques, conventionally used for the fabrication of electronic and optoelectronic devices. As a consequence the first part of the research activity was related to the development of reproducible and controlled protocols for the fabrication of polymeric soft masks for advanced lithographic applications using block copolymers. To this purpose hexagonally packed nanoporous polymeric thin films were fabricated using PS-b-PMMA block copolymers and accurately characterized. The main output of this part of the research activity was related to the understanding and control of all the parameters that allows a fine tuning of the characteristic dimensions (thickness, diameter and pore-to-pore distance) of the final polymeric template. Special care was used to the functionalization of the sample surface prior to block copolymer thin film deposition. The effect of the self assembled monolayer of random copolymers conventionally used for surface neutralization was deeply investigated. In particular we observed that different random copolymer thin films influence the window of thicknesses in which perpendicular orientation of the PMMA domains with respect to the underlying substrate occurs, as well as the characteristic dimensions of the final nanoporous polymeric mask.

Nevertheless, in the fabrication of microelectronic and optoelectronic devices, a simple periodic structure is not sufficient and the organization of nanostructures

into precise locations, which are not periodic, is required. The spatial control of functional nanostructures using block copolymers can be achieved by topographically patterned substrates that deliver an external guidance for the ordering of block copolymer domains with alignment to surface patterns. The possibility of combining "bottom up" self assembly of block copolymers with "top down" patterned templates was explored to register the periodic domains of the self assembled block copolymer film with the underlying topographic structure. Moreover this approach is expected to improve the long range order of the nanostructures, at the same time reducing defects formation and increasing size uniformity. E-beam lithography was used to fabricate trenches in the SiO_2 substrate before the deposition of the block copolymer thin films. Surprisingly the registration of the nanostructured block copolymer film within the topographically defined structures required much longer annealing time than on flat surfaces. Further experiments are currently running in order to investigate the time evolution of the block copolymer phase separation when the polymeric film is physically confined in one or more dimensions.

The nanoporous polymeric mask fabricated during the first part of the research activity was then used as soft mask for patterning the underlying substrate in order to create nanoporous SiO_2 hard masks as well as for the fabrication of ordered arrays of Silicon nanodots.

The hexagonally packed nanopores of the polymeric mask were transferred to the underlying SiO_2 by reactive ion etching (RIE). The effects of the etching parameters on the final characteristics of the nanoporous oxide were deeply investigated. Increasing the etching time a progressive enlargement of the pores was observed and correlated with the degradation of the polymeric mask during the etching process. The nanoporous SiO_2 template was then used as a backbone for the fabrication of tunable nanoporous Al_2O_3 substrates by atomic layer deposition (ALD) growth of thin films of Al_2O_3 on the SiO_2 template. Progressive reduction of the pore size down to complete pore filling was obtained by properly adjusting the thickness of the Al_2O_3 film. This activity demonstrated the feasibility of fabricating periodic nanostructures surfaces with tunable dimensions well below the 20 nm limit. Moreover, since a large variety of oxide materials can be grown by ALD, the proposed methodology provided a general approach for the synthesis of nanoporous oxide with accurate control of pore dimension, size distribution and pore frequency.

Ordered arrays of Si nanocrystals were fabricated using the nanoporous polymeric film as a lithographic mask to control the formation of the nanodots. Two different approaches were pursued leading to different configurations where nanodots are embedded/deposited in/on the dielectric matrix. The first approach was based on ion beam synthesis and consisted in the implantation of Si ions into the nanostructured polymeric film to locally introduce the desired ion supersaturation in a limited nanosized area. After removal of the polymeric film, a thermal annealing led to the formation of nanocrystals at a depth depending on the ion energy. The second approach was the lift-off process that included material deposition by e-beam evaporation onto the nano-structured polymeric film and on the exposed substrate regions followed by the subsequent removal of the polymeric template and material excess by wet or dry etching. These arrays of semiconducting nanodots are suitable for the fabrication of Si nanocrystals non volatile memories or Si nanocrystals nanoemitters. During the next year the research activity will focus on the integration of these nanostructures in real memory devices and in the exploitation of their functionalities. In particular the possibility to address limited or even single Si nanodots will be explored in order to investigate the effect of discrete charges on the device standard operations.

Acknowledgements

I wish to thank all the people who have contributed to the realization of the present thesis, in particular my tutor Prof. Marco Fanciulli for supervising my research activity during these three years.

I am deeply indebted with Dr. Michele Perego, who gave me the possibility to work on the present thesis and assisted me with great professionalism.

A special thank to Dr. Gabriele Seguini for his support and for many fruitful discussions.

Thanks to all the people who worked at MDM during these years, in particular to Dr. Antonio Vellei and Mario Alia for their collaboration and companionship.

I would like to thank the people involved in the NANOBLOCK project, Dr. Gerard BenAssayag, Dr. Sylvie Schamm-Chardon, Dr. Celia Castro and Prof. Paolo Pellegrino, for their help.